SPATIAL HETERODYNE RAMAN SPECTROSCOPY FOR PLANETARY SURFACE EXPLORATION

A THESIS SUBMITTED TO THE OFFICE OF GRADUATE EDUCATION OF THE UNIVERSITY OF HAWAIʻI AT MĀNOA IN PARTIAL FULFILMENT OF THE REQUIREMENTS FOR THE DEGREE OF

MASTER OF SCIENCE
IN
CHEMISTRY

MAY 2017

By
Miles Jacob Egan

Thesis Committee:

John Head, Chairperson

Thomas Apple

Shiv K. Sharma

Keywords: spatial heterodyne spectrometer, Raman spectroscopy, Fourier transform Raman, interferometry, mineralogy

ACKNOWLEDGMENTS

I would like to thank my family for financial support and encouragement in my academic pursuits. I would like to thank Dr. Shiv Sharma for providing me the opportunity to work in his laboratory and for sharing his valuable experience that has guided me through my degree. In addition, I would like to thank Professor John Head for his levelheaded council and also for teaching me computer programming. I would like to thank Professor Thomas Apple for his interest in this project and for his help in educating me about Fourier transforms. Furthermore, I would like to thank Dr. S. Michael Angel, Dr. Nirmal Lamsal, and Dr. Tayro E. Acosta for their valuable help in the early stages of this work. I would like to thank Dr. Anupam Misra for the generosity of spirit he has shown me during my time at the University of Hawai'i at Mānoa. Finally, I would like to thank to Nancy Hulbirt and May Izumi for their help with figures and editing, respectively. This work was supported in part by NASA under grant NNX14AI34G.

ABSTRACT

Raman scattering is a phenomenon characterized by the inelastic scattering of light by a molecule that has a normal mode of vibration capable of producing an instantaneous induced dipole moment when radiation is incident upon said molecule. The activity of vibrational modes in the Raman spectrum can be predicted via group theory by first identifying all the symmetry elements of a molecule or mineral, classifying said molecule into a point or space group, followed by removal of superfluous degrees of freedom and finally disambiguation of the vibrational degrees of freedom into irreducible representations. A vibrational mode is active in the Raman (IR) spectrum if the vibrational mode, as represented by an irreducible representation, contains a change in polarizability (change in dipole moment).

In recent years, advancements in the speed, sensitivity and size of excitation sources, spectrographs and detectors has allowed the application of Raman spectroscopy to transition from delicate laboratory instruments to rugged in-situ spectrometers. The advancement in Raman instrumentation has simultaneously expanded the potential applications of Raman spectroscopy, which now ranges from pharmaceutical drug quality control to explosives detection to geological analysis on planetary surfaces. One of the most promising innovations in the field of Raman spectroscopy is the development of the spatial heterodyne Raman spectrometer (SHRS). SHRS is a variant of a Michelson interferometer in which the mirrors of a Michelson are replaced with two stationary diffraction gratings. When light enters SHRS, it is reflected off the diffraction gratings at frequency dependent angles that in turn produce crossed wavefronts in space that can be imaged by a plane array detector. The crossed wavefronts, which represent a superposition of interference fringes, are converted to a Raman spectrum upon Fourier transformation.

This thesis is divided into four parts. In Chapter 1, the historical evolution of the theory and instrumentation of Raman spectroscopy is covered in detail. In Chapters 2 and 3, SHRS is used to measure the Raman spectra of materials of importance to planetary science exploration at standoff distances. Finally, in Chapter 4, the author takes account of the lessons learned from the preceding chapters and recommends some future work.

TABLE OF CONTENTS

List of Tables

List of Figures

ns, the practical width of a laser pulse, in order to reject ambient light. The intensifier gain of the ICCD was set to 150. The images were accumulated for 30 seconds.

2.4. The Raman spectra of anhydrite ($CaSO_4$) and gypsum ($CaSO_4 \cdot 2H_2O$) in the 100-1260 cm^{-1} region. The settings used for these spectra were identical to those described in **Fig. 2.3**.

2.5. The Raman spectra of forsteritic olivine (Fo_{91}) and feldspars, specifically microcline and plagioclase in the 100-1200 cm^{-1} region. The settings used for these spectra were identical to those described in **Fig. 2.3** except for the accumulation time, which in this case was 50 seconds for olivine and 60 seconds for microcline and plagioclase.

3.1. An illustration of the SHRS system used to measure Raman spectra at a distance of 5 meters. B.E. stands for beam expander.

3.2. An illustration of how data is reduced from "phase corrected FT" (top image) to the white noise Raman spectrum (labeled C) by dividing the raw one-dimensional Fourier Transform (labeled A) by the lineshape of the shot noise (labeled B).

3.3. A depiction of the data reduction process in which raw shot noise is converted to white noise via modeling with a pseudovoigt curve. The noise is white noise if the Fourier transform is an impulse at x = 0 and the autocorrelation is a triangle.

3.4. The Raman spectra of carbonate minerals measured at a distance of 0.1 m with a laser power of 8.6 mJ per pulse and a camera gain of 150. The Littrow angle was set to retro-reflect 550 nm light. The accumulation time was 1 seconds.

3.5. The Raman spectra of sulfate minerals measured at a distance of 0.1 m with a laser power of 8.6 mJ per pulse and a camera gain of 150. The Littrow angle was set to retro-reflect 550 nm light. The accumulation time was 1 seconds.

3.6. The Raman spectra of orthosilicate minerals measured at a distance of 0.1 m with a laser power of 8.6 mJ per pulse and a camera gain of 150. The Littrow angle was set to retro-reflect 550 nm light. The accumulation time was 10 seconds.

3.7. The Raman spectra of tectosilicate minerals measured at a distance of 0.1 m with a laser power of 8.6 mJ per pulse and a camera gain of 150. The Littrow angle was set to retro-reflect 550 nm light. The accumulation time was 10 seconds.

3.8. The Raman spectra of α-spodumene and fluorapatite minerals measured at a distance of 0.1 m with a laser power of 8.6 mJ per pulse and a camera gain of 150. The Littrow angle was set to retro-reflect 550 nm light. The accumulation time was 10 seconds.

3.9. The Raman spectra of carbonate minerals measured at a distance of 5 m with a laser power of 8.6 mJ per pulse and a camera gain of 150. The Littrow angle was set to retro-reflect 554 nm light. The accumulation time was 10 seconds.

3.10. The Raman spectra of sulfate minerals measured at a distance of 5 m with a laser power of 8.6 mJ per pulse and a camera gain of 150. The Littrow angle was set to retro-reflect 554 nm light. The accumulation time was 10 seconds.

3.11. The Raman spectra of silicate minerals measured at a distance of 5 m with a laser power of 8.6 mJ per pulse and a camera gain of 150 (250 for forsterite). The Littrow angle was set to retro-reflect 554 nm light. The accumulation time was 30 seconds.

3.12. The Raman spectra of silicate minerals measured at a distance of 5 m with a laser power of 8.6 mJ per pulse and a camera gain of 250 (150 for α-quartz). The Littrow angle was set to retro-reflect 554 nm light. The accumulation time was 60 seconds (30 seconds for α-quartz).

3.13. The Raman spectra of salts measured at a distance of 5 m with a laser power of 8.6 mJ per pulse and a camera gain of 150. The Littrow angle was set to retro-reflect 554 nm light. The accumulation time was 10 seconds.

3.14. The Raman spectra of salts measured at a distance of 5 m with a laser power of 8.6 mJ per pulse and a camera gain of 150. The Littrow angle was set to retro-reflect 554 nm light. The accumulation time was 10 seconds.

3.15. The Raman spectra of organic compounds measured at a distance of 5 m with a laser power of 8.6 mJ per pulse and a camera gain of 250 (150 for naphthalene). The accumulation time was 10 seconds. The Littrow angle for acetonitrile,

naphthalene, anthracene and cyclohexane was set to retro-reflect 586, 599, 589 and 592 nm light, respectively.

3.16. The signal-to-noise Raman spectrum of cyclohexane, measured at 5 meters with a laser power of 8.6 mJ per pulse, 250 camera gain and 60 second accumulation time. The Littrow angle was set to retro-reflect 592 nm light.

List of Abbreviations

CCD – charge coupled device

CW – continuous wave

DCG – dichromate gelatin

DPSS – diode pumped solid state

EM – electromagnetic

FT – Fourier Transform

FWHM – full width half maximum

IC – internal conversion

ICCD – intensified charge-coupled device

IR – infrared

ISC – intersystem crossing

PMT – photomultiplier tubes

SHRS – spatial heterodyne Raman spectrometer

SHS – spatial heterodyne spectrometer

SPAD – single photon avalanche diode

UV – ultraviolet

VPHG – volume phase holographic gratings

Chapter 1: Raman Spectroscopy – Theory and Laboratory Spectra of Geologic Materials

(The majority of this chapter was submitted to Cambridge University Press as part of a book that covers remote sensing techniques for planetary surface exploration. Publication date TBD.)

Raman scattering is a type of inelastic scattering of light by molecules that changes the energy of a photon by an amount of energy equal to a vibrational transition of said molecule. Raman scattering can be modeled mathematically from the point-of-view of classical electrodynamics and quantum mechanics. Both descriptions of the phenomenon of Raman scattering will be outlined in the course of this chapter. The Raman activity of vibrational modes depends upon the symmetry of the molecule, as described by group theory, as well as the symmetry properties of the normal mode of vibration. This chapter will introduce the concepts necessary to identify the symmetry properties of molecules and minerals and their associated vibrational modes. Following the exposition of the theory of Raman scattering, the author will describe the principle components of Raman spectrometers, specifically excitation sources, spectrographs and detectors. In recent years, technological advancements have expanded the potential applications of Raman spectroscopy. Some of these technological advances include, but are not limited to, the development of reliable continuous wave and pulsed lasers at a variety of wavelengths, the advancement of multichannel detectors such as two-dimensional charge-coupled devices and photodiode arrays, and the coupling of optical accessories such as microscopes and telescopes. The applications of these advanced Raman systems in the fields of Earth and planetary science are highlighted herein.

1.1 Introduction to Raman Scattering

In 1928, C.V. Raman[1-2] discovered inelastic scattering of light during the course of extended research on the molecular scattering of light. For this discovery, Raman was awarded the Physics Nobel Prize in 1930 and the effect is named after the discoverer (i.e. the Raman Effect). Raman observed that when monochromatic light of frequency ν_0 is

incident on a transparent sample, the spectrum of the scattered light shows two distinct features. One feature is elastically scattered light of identical frequency, called the Rayleigh line, and the other is a pattern of spectral lines of altered frequency ($\Delta\nu_i$), called the Raman spectrum. The pattern on the low frequency side of the exciting light ($-\Delta\nu_i$), which is at longer wavelength than the exciting light, resembles the Stokes shift found in luminescence spectra. For this reason these spectral features are referred to as Stokes-Raman lines. An analogous pattern occurs on the high frequency side ($+\Delta\nu_i$) at shorter wavelengths, referred to as anti-Stokes Raman lines. The relationship of intensities between the Stokes and anti-Stokes Raman lines depends upon the temperature and energy gap between vibrational energy states of the sample, which will be described in **Section 1.2.3**. Raman spectroscopy provides complementary information to infrared spectroscopy because the selection rules are different. These selection rules are characterized in **Section 1.2.5**.

Raman spectral analysis has a number of advantages over passive IR and optical spectroscopy, chief among them being the sharpness and selectivity of spectral features. This allows unambiguous detection of specific minerals, in particular, mineral mixtures, rocks and isochemical glasses. A number of authors[3-8] have reviewed the applications of Raman techniques to geological materials. In this chapter, the basic theory of normal (spontaneous) and resonance Raman scattering are discussed along with advanced Raman techniques applicable to geological materials.

1.2 Theory of Normal Raman Scattering

1.2.1 Classical Theory of Normal Raman Scattering

The phenomena of Rayleigh and Raman scattering can be explained in part by classic electrodynamics[9]. In the classical electrodynamics framework, light scattering is thought to be an interaction between an electromagnetic (EM) wave and matter in which the EM wave perturbs the electron clouds of the sample atom or molecule. The perturbation of the electron cloud results in the periodic separation of the center of positive and negative charges within the atom or molecule, which produces an induced dipole (P). The oscillating induced dipole moment is a source of EM radiation, which may produce scattered light. In the simplest case, a hypothetical atom with a spherical symmetric electron cloud has no permanent dipole moment. Its induced dipole may be modeled as Eq. (1.1)

$$P = \alpha E \tag{1.1}$$

where α is a constant of proportionality (also known as polarizability), and E is the magnitude of the electric field as described by $E = E_0 \cos 2\pi\nu_0 t$. When an atom is placed in an oscillating field of EM light of frequency ν_0, it will induce a dipole moment P given by Eq. (1.2)

$$P = \alpha E_0 \cos(2\pi\nu_0 t) \tag{1.2}$$

where ν_0 is the frequency in Hz (c/λ_0, where c is the velocity of light, and λ_0 is the wavelength of light) of incident light, and t is time.

In the case of molecules, polarizability is not constant as certain vibrations and rotations of a molecule can cause α to vary. For example, during the vibration of a diatomic molecule, the molecular shape is alternately compressed and extended. If the electron cloud is not identical at the extremes of the vibration, a change in polarizability will result. For small displacements the polarizability of a diatomic molecule can be given as Eq. (1.3)

$$\alpha = \alpha_0 + \left(\frac{\partial\alpha}{\partial Q}\right) dQ \tag{1.3}$$

where dQ is the difference between the inter-nuclear distance and the equilibrium inter-nuclear distance at a given time, and $\partial\alpha/\partial Q$ is the change of α with respect to dQ. If the vibration is considered harmonic, dQ can be modeled by Eq. (1.4)

$$dQ = Q_0 \cos(2\pi\nu_{vib} t) \tag{1.4}$$

where Q_0 is the maximum displacement about the equilibrium position, and ν_{vib} is the vibrational frequency. Substituting the values of α and dQ from Eq. (1.3) and (1.4) in Eq. (1.2) yields Eq. (1.5).

$$P = \alpha_0 E_0 \cos(2\pi\nu_0 t) + \left(\frac{\partial\alpha}{\partial Q}\right) E_0 Q_0 \cos(2\pi\nu_0 t)\cos(2\pi\nu_{vib} t) \tag{1.5}$$

Using the product to sum trigonometric identity, the above equation can be rewritten as:

$$P = \alpha_0 E_0 \cos(2\pi\nu_0 t) + \left(\frac{E_0 Q_0}{2}\right)\left(\frac{\partial\alpha}{\partial Q}\right)[\cos(2\pi(\nu_0 + \nu_{vib})t) + \cos(2\pi(\nu_0 - \nu_{vib})t)] \tag{1.6}$$

It is clear from Eq. (1.6) that the spectrum of the scattered light will contain the line corresponding to incident light (Rayleigh scattering), and two modified lines corresponding to frequencies ($\nu_0 \pm \nu_{vib}$) (Raman scattering). According to this theory, the intensity of the Rayleigh line depends on the square of the amplitude (i.e. $(E_0\alpha_0)^2$) and the intensities of the Raman lines depend on $(E_0Q_0/2)^2 * (\partial\alpha/\partial Q)^2$, where $\partial\alpha/\partial Q$ is the rate of

change of α during a given normal mode of vibration. An obvious corollary from this description of Raman scattering is that $\partial\alpha/\partial Q$ must be non-zero in order for Raman scattering to take place. The above description outlines the classical explanation of Stokes and anti-Stokes Raman lines. The major limitation of the classical theory is that it does not accurately predict intensities. According to the classical theory, the intensities of Stokes-Raman and anti-Stokes Raman lines should be equal. This prediction is not borne out by experiment and will be explained via quantum mechanics in **Section 1.2.3**.

1.2.2 Polarization and Intensities of Raman Lines

Polarization of incident radiation and the orientation of single crystal samples affect the intensities of Raman scattered radiation. Studies of the intensities of Raman lines in varying polarization and crystal orientations provides a valuable guide in assigning observed frequencies to specific modes of vibrations.

As discussed previously, a normal mode of vibration is allowed in the Raman spectrum if the polarizability of the molecule changes during the mode. By resolving P, α, and E in the x, y, and z directions, the following relationships are anticipated.

$$P_x = \alpha_x E_x;\ P_y = \alpha_y E_y;\ P_z = \alpha_z E_z \tag{1.7}$$

Equation (1.7) is only applicable to a completely spherical molecule. Most molecules, however, have structures that are not totally spherical. Therefore the equation does not hold in such cases because the direction of polarization does not coincide with the direction of the applied field. In place of Eq. (1.7), the following relationships, as described by Eq. (1.8), must be used instead.

$$\begin{bmatrix} P_x \\ P_y \\ P_z \end{bmatrix} = \begin{bmatrix} \alpha_{xx} & \alpha_{xy} & \alpha_{xz} \\ \alpha_{yx} & \alpha_{yy} & \alpha_{yz} \\ \alpha_{zx} & \alpha_{zy} & \alpha_{zz} \end{bmatrix} \begin{bmatrix} E_x \\ E_y \\ E_z \end{bmatrix} \tag{1.8}$$

The 3x3 matrix on the right hand side of Eq. (1.8) is called the second rank polarizability tensor. It is a symmetric tensor, meaning that $\alpha_{xy} = \alpha_{yx}$; $\alpha_{yz} = \alpha_{zy}$; and $\alpha_{xz} = \alpha_{zx}$. Equations (1.7) and (1.8) describe Rayleigh scattering. For Raman scattering, the polarizability components α_{xx}, α_{xy}, $\alpha_{xz,}$ etc… should be replaced with terms corresponding to the change in polarizability with respect to coordinate $\partial\alpha_{xx}/\partial Q$, and so on. One can visualize the polarizability tensor by means of a polarizability ellipsoid.

In order to define the term depolarization ratio in the Raman spectra of fluids, which measures the degree of depolarization of Raman lines, let us assume that the *x* axis is the direction of propagation of incident monochromatic light unto the sample and the direction of observation is perpendicular to the *x* axis in the *yz* plane. If the plane polarized incident laser light is the excitation source, then the depolarization ratio ρ_p is defined as the ratio of intensity of the scattered light polarized perpendicular to the *yz* plane, $I_{\perp}$, to that polarized parallel to the *yz* plane, $I_{||}$, as described by Eq. (1.9).

$$\rho_p = \frac{I_{\perp}}{I_{||}}. \tag{1.9}$$

In the case of fluid samples, including glasses, where all orientations of scattering molecules are possible, the degree of depolarization[9] of a totally symmetric Raman line will be close to zero and the maximum degree of depolarization of an anti-symmetric Raman line will be 3/4. A measurement of the depolarization ratio in gases, solutions, and glasses provides a means of distinguishing totally symmetric vibrations from the rest of the vibrational modes.

The effect of polarization of radiation and orientation of crystals on the Raman spectra was investigated using a 90-degree scattering geometry in the early days of Raman spectroscopic research[10-11] on single crystals of sodium nitrate and calcite and found that the polarization of Raman lines varies with orientation of the crystals. The polarized Raman spectral analysis of an oriented single crystal yields a detailed description of the symmetry of crystal vibrations. In the 1960's, Porto's group at the Bell Laboratories[12] proposed a useful notation to specify the relative orientation of the polarization vector. In the case of an oriented crystal excited by polarized laser light under a 90-degree scattering configuration, these authors proposed the notation *x*(*zx*)*y* where *x* is the direction of propagation of incident light and *y* is the direction of propagation of scattered light. The terms within the parenthesis refer to the polarization of the incident and scattered light, respectively. These terms represent the α'_{zx} component of the change in the polarizability. By changing the polarization of the incident light, scattered light, and crystal orientation, all the components of the polarizability tensor can be observed and the symmetry species of various modes can be identified.

1.2.3 Jablonski Energy Diagram: Phenomena of Radiative and non-Radiative Energy Transitions

A Jablonski diagram[13] is a type of energy diagram that depicts how a molecule may absorb, emit, scatter or otherwise dissipate electromagnetic radiation. The principle components of the diagrams are the discrete electronic and vibrational energy states, illustrated in **Fig 1.1** as bold and muted horizontal lines, as well as straight and curved vertical lines that show how a molecule may transform from one energy state to another. The bulk of the phenomena shown in **Fig 1.1** begin when a molecule absorbs a photon and is excited from a low electronic energy level to a higher electronic energy level. It is important to note that only photons that possess an amount of energy equal to the difference in energy between two energy states may be absorbed. After absorption, the molecule will seek to return to the ground electronic energy state and may do so by means of radiative or non-radiative transitions. The non-radiative transitions will be addressed first as they occur more quickly than the radiative transitions.

A non-radiative transition is any mechanism by which a molecule dissipates energy without emitting a photon. These mechanisms include vibrational relaxation, internal conversion (IC) and intersystem crossing (ISC). When a molecule absorbs an ultraviolet-visible photon, the molecule typically arrives at an excited electronic and an excited vibrational energy state. The molecule will then relax to the ground vibrational energy state in the excited electronic energy state by a process called vibrational relaxation in a time span of 10^{-14} to 10^{-11} seconds. Vibrational relaxation is the loss of vibrational excitation through transfer of energy to the environment by collisions with other molecules. Internal conversion is another method of non-radiative dissipation of energy where a molecule transitions from an excited electronic energy state to a vibrational excited energy state within the ground electronic energy state. This process may occur within 10^{-14} to 10^{-11} seconds as well. Finally, intersystem crossing is a non-radiative dissipation of energy where a molecule transitions between two excited electronic energy states of different spin multiplicities. Intersystem crossings typically take between 10^{-8} and 10^{-3} seconds.

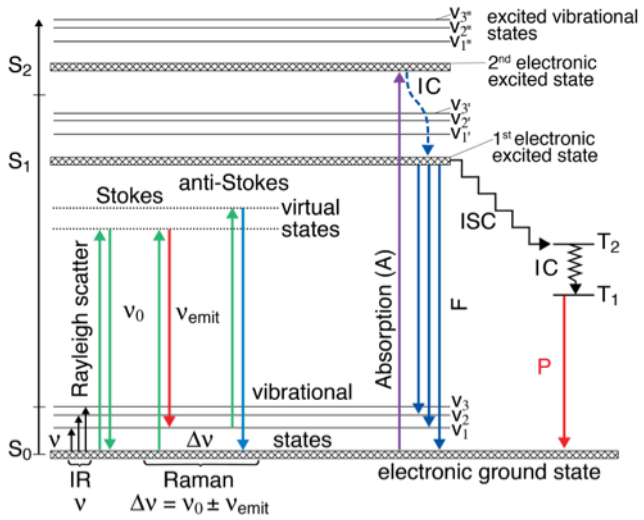

Figure 1.1 – Jablonski energy level diagram showing the virtual states involved in elastic (Rayleigh) and inelastic (Raman) scattering and the real electronic excited states involved in fluorescence and phosphorescence (see text for explanation). Figure modified from Panczer[14].

The radiative transitions are those processes that include emission of a photon in order to dissipate excess energy from excited electronic states. There are two varieties of radiative transitions – fluorescence (F) and phosphorescence (P) – that proceed by separate mechanisms. Fluorescence is a mechanism where a photon is emitted from a singlet first excited electronic energy state to a singlet ground electronic energy state, a process that takes 10^{-9} to 10^{-7} seconds to occur. Phosphorescence is a mechanism where a photon is emitted from a triplet excited electronic energy state to a singlet ground electronic energy state. Triplet excited states typically cannot be populated from absorption of a photon alone and must first go via intersystem crossing from an excited singlet electronic energy state to the triplet excited electronic energy state. Intersystem crossing is one of the slowest transitions, taking between 10^{-8} to 10^{-3} seconds, because a transition from a singlet to a triplet electronic state is strictly speaking forbidden based on electronic selection rules. Therefore, phosphorescence is also a slow process, taking between 10^{-4} to 10^{-1} seconds. Phosphorescence may occur in minerals and typically originate from transition metal ion or rare-earth ion impurities[14-16].

The most important feature of **Fig 1.1** for the purposes of this chapter is the elastic and inelastic scattering of light by molecules. Atoms or molecules, which are smaller in extent

than that of the incident light, may elastically scatter light by first absorbing the light, thereby exciting the atom or molecule to a virtual state, followed by relaxation of the atom or molecule and simultaneous re-emission of a photon of identical frequency to that of the incident light. This phenomenon is known as Rayleigh scattering. Raman scattering is a type of inelastic scattering of light by molecules that changes the energy of a photon by an amount of energy equal to a vibrational transition of said molecule. As discussed in **Section 1.2**, the scattered light may be of greater (i.e. anti-Stokes shifted) or lesser in energy (i.e. Stokes shifted) than the incident light. The intensity ratio of the Stokes to anti-Stokes Raman lines of a sample will depend upon the population of molecules in the ground and excited vibrational states, according to following Eq. (1.10)

$$\frac{I_{Stokes}}{I_{anti-Stokes}} = \frac{(\nu_0-\Delta\nu)^4}{(\nu_0+\Delta\nu)^4} e^{(-hc\Delta\nu/kT)} \tag{1.10}$$

where h is Planck's constant, k is Boltzmann's constant, T is the temperature in Kelvin, ν_0 is the wavenumber of the excitation laser and $\Delta\nu$ is the Raman shift due to a normal mode of vibration of the molecule (ν_{vib}) in cm^{-1}. The intensity ratio predicted in Eq. (1.10), which is based on quantized nature of vibrational modes, is consistent with the observed ratio of Stokes-Raman to anti-Stokes Raman lines. Based on Eq. (1.10), the Stokes to anti-Stokes ratio of Raman lines can be used to determine the temperature of the sample.

For a molecular bond, the individual atoms are confined to specific set of quantized vibrational modes[17]. For example, the vibrational energy of a particular vibrational mode in a diatomic molecule can be given by the solution of the Schrödinger equation as detailed in Eq. (1.11)

$$\frac{d^2\Psi}{dq^2} + \frac{8\pi^2\mu}{h^2}\left(E - \frac{1}{2}Kq^2\right)\Psi = 0 \tag{1.11}$$

where Ψ is the wave function of the quantum system, q is the atomic displacement from the equilibrium position, μ is the reduced mass of the system and K is the force constant. Solving for the condition that the wave function must be single valued, continuous and quadratically integrable, the eigenvalues are given by Eq. (1.12)

$$E_v = (v + 0.5)h\nu_{vib} \tag{1.12}$$

where v is the vibrational quantum number, 0.5 is the zero point energy, ν_{vib} is the vibrational frequency, and the frequency of vibration is given by Eq. (1.13).

$$\nu_{vib} = \frac{1}{2\pi}\sqrt{\frac{K}{\mu}}. \quad (1.13)$$

The vibrational frequencies depend on the reduced mass of atoms involved in a particular vibration. Isotopic substitutions have been used to assign the origin of the vibrational modes in silicate minerals and glasses[5].

1.2.4 Resonance Raman Scattering

Resonance Raman scattering is a variant of the "normal" Raman scattering phenomenon. Normal Raman spectroscopy is typically performed using laser sources whose energy is above the vibrational or rotational energies of the molecule, but far below the first electronic excited state. Resonance Raman scattering takes place when the laser's energy nears that of an electronic excited state (e.g., 1st or 2nd electronic excited state in **Fig 1.1**). In such a case, the Raman bands originating in the excited electronic transition may show very strong enhancements with intensities 10^3 to 10^5 higher than predicted by the ν_0^4 rule for normal Raman. When the excitation energy is in the vicinity of the electronic absorption, the term "pre-resonance Raman scattering" is commonly used. In minerals, Raman enhancement has been observed[18-19] for the iron containing oxides such as hematite (α-Fe_2O_3), maghemite (γ-Fe_2O_3), and magnetite (Fe_3O_4). For this group of minerals, pre-resonance Raman[20] occurs with 636 nm excitation due to a spectral absorption band located near 640 nm. Resonance Raman is also observed in biominerals[21] containing chromophore biomolecules such as carotene in pink corals.

1.2.5 Normal Modes of Vibrations and Selection Rules

Group theory and its application to molecular vibrations have been described in several textbooks[5,9,22-25]. An overview of the concepts will be provided in this section.

For every atom of a given molecule, there exist three independent motions along a Cartesian axis that the atom may move (i.e. x, y or z). Every independent motion is known as a degree of freedom. In total, a molecule with N atoms will have 3N degrees of freedom. When all atoms of a given molecule move along the same Cartesian axis in unison, the molecule moves through space in what is called a translation. Since there are three Cartesian axes, there are three translational degrees of freedom. In addition to translational

degrees of freedom, a molecule may exhibit a spin or angular momentum about an axis. For non-linear molecules, the number of rotational degrees of freedom is three; for linear molecules, the number of rotational degrees of freedom is two since rotation about the third axis in a linear molecule is identical to doing nothing. The remaining degrees of freedom, 3N – 6 for non-linear molecules and 3N – 5 for linear molecules, represent a superposition of the normal modes of vibration. The superposition of vibrational modes may be reduced to individual vibrational modes called normal modes of vibration by applying group theory. A brief overview of the concepts and procedure is given below.

The first step in identifying the number, symmetry and activity of vibrational modes of a given molecule is to identify all symmetry elements of said molecule. A symmetry element is a point, line or plane from which a symmetry operation can transform a molecule into a new orientation that leaves said molecule indistinguishable from its starting position. Once all symmetry elements have been identified, a molecule may be classified into a point group by utilizing tree diagrams such as those published by Cotton[22] or Harris[26]. For every point group, there exists a character table that defines all symmetry elements (e.g. E, C_n, i, σ_v, S_n, etc…), irreducible representations (e.g. A_1, B_1, E_1, etc…) as well as which irreducible representations contain a change in dipole moment (e.g. x, y or z), rotational degree of freedom (e.g. R_x, R_y or R_z) and/or change in polarizability (e.g. xy, yz, xz, x^2, y^2, etc…). Once the superposition of vibrational modes are reduced to normal modes of vibration, the character tables can be used to predict which vibrational modes will be Raman or IR active by applying the following selection rule. *For molecular vibrations, a vibration is Raman (IR) active if the normal mode of vibration, whose symmetry properties are described by an irreducible representation, contains a change in polarizability (change in dipole moment).*

Every irreducible representation has associated with it a Mulliken symbol that characterizes the symmetry properties of the representation. The best summary of the symmetry properties of Mulliken symbols was written by Colthup[9] and is provided below.

A	Symmetric with respect to principal axis of symmetry
B	Anti-symmetric with respect to principal axis of symmetry

E	Doubly degenerate vibrations, the irreducible representation is two dimensional
F	Triply degenerate vibrations
g and *u* (subscripts)	Symmetric or anti-symmetric with respect to a center of symmetry
1 and 2 (subscripts)	Symmetric or anti-symmetric with respect to rotational axis (C_p) or rotation-reflection axis (S_p) other than the principal axis or in those point groups with only one symmetry axis with respect to plane of symmetry
‘ or ‘’ (superscripts)	Symmetric or anti-symmetric with respect to plane of symmetry.

For linear molecules belonging to the point group $C_{\infty v}$ and $D_{\infty h}$, capital Greek letters designations are used as follows:

Σ^+	Symmetric with respect to plane of symmetry through the molecular axis
Σ^-	Anti-symmetric with respect to plane of symmetry through the molecular axis
Π, Δ, Φ	Degenerate vibrations with degree of degeneration increasing in this order.

The generation of irreducible representations corresponding to normal modes of vibration can be achieved by the following method. First, apply each symmetry operation of the appropriate point group on a molecule in succession and count the number of atoms that remain unmoved. Label this representation $\Gamma_{unmoved}$. Second, add up the irreducible representations that contain a change in dipole moment. Label this representation Γ_{xyz}. Third, multiply $\Gamma_{unmoved}$ by Γ_{xyz}. Label this representation Γ_{total}. Fourth, subtract the translational and rotational degrees of freedom from Γ_{total}. Label this representation Γ_{vib}. Γ_{vib} represents the superposition of all vibrational modes and can be reduced to irreducible representations by application of Eq. (1.14).

$$a_i = \frac{1}{h}\sum_R \chi^R \chi_i^R C^R \tag{1.14}$$

where a_i is the number of times an irreducible representation appears in Γ_{vib}, h is the order of the point group found by summing the number of symmetry elements, χ^R is the character of the operation R in the reducible representation Γ_{vib}, χ_i^R is the character of the operation R in the i^{th} irreducible representation, and C^R is the number of members in the class to which R belongs[26]. In the following section, this procedure will be applied to an example molecule – the water molecule – so that the reader can concretize this procedure.

1.2.5.1 Vibrational Modes of H_2O Molecule

Let us first identify the symmetry elements of H_2O. Water has a 180° axis of rotation and two mirror planes parallel to this axis of rotation, as shown in **Fig 1.2**. Therefore, water belongs to the point group labeled C_{2v}.

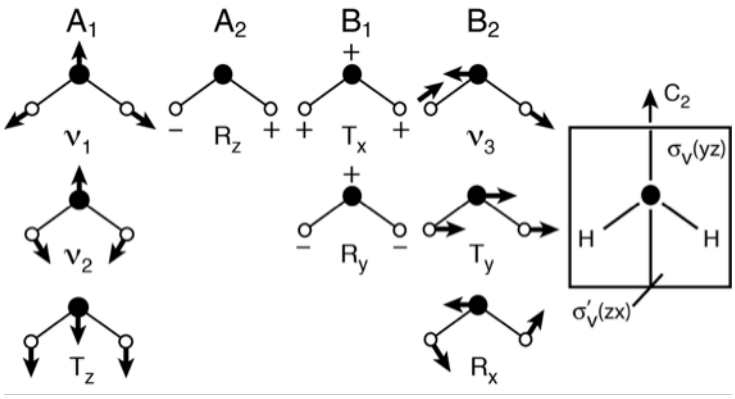

Figure 1.2 – This figure illustrates the degrees of freedom of water and their associated symmetry properties. The motions labeled with T, R or ν correspond to translational, rotational and vibrational degrees of freedom, respectively. The + and – sign represent motions into and out of the plane of the paper.

Now, apply each symmetry operation of the point group C_{2v} to a water molecule, as depicted in **Fig 1.2**, and write down the numbers of atoms that remain unmoved.

$$\Gamma_{unmoved} = \begin{matrix} E & C_2(z) & \sigma_v(xz) & \sigma_v(yz) \\ 3 & 1 & 1 & 3 \end{matrix}$$

Next let us add up the irreducible representations that contain a change in dipole moment. For the C_{2v} point group, A_1, B_1 and B_2 contain a change in dipole moment. Let $\Gamma_{xyz} = A_1 + B_1 + B_2$.

$$\Gamma_{xyz} = 3 \quad -1 \quad 1 \quad 1$$

Now let us multiply $\Gamma_{unmoved}$ by Γ_{xyz} and label the product Γ_{total}.

$$\Gamma_{total} = 9 \quad -1 \quad 1 \quad 3$$

Next, let's subtract the translational and rotational degrees of freedom from Γ_{total} and label this new representation Γ_{vib}. The translational degrees of freedom are equal to Γ_{xyz} and the rotational degrees of freedom for C_{2v} are equal to $\Gamma_{rot} = A_2 + B_1 + B_2$.

$$\Gamma_{vib} = 3 \quad 1 \quad 1 \quad 3$$

Finally, let us use Eq. (1.14) to determine the number and variety of irreducible representations present in Γ_{vib}.

$$A_1 = \frac{1}{4}\{(3*1*1) + (1*1*1) + (1*1*1) + (3*1*1)\} = 2$$

$$A_2 = \frac{1}{4}\{(3*1*1) + (1*1*1) + (1*-1*1) + (3*-1*1)\} = 0$$

$$B_1 = \frac{1}{4}\{(3*1*1) + (1*-1*1) + (1*1*1) + (3*-1*1)\} = 0$$

$$B_2 = \frac{1}{4}\{(3*1*1) + (1*-1*1) + (1*-1*1) + (3*1*1)\} = 1$$

Hence the three vibrational modes of water have the symmetry of A_1, A_1 and B_2. Upon inspection of the C_{2v} character table in **Table 1.1**, it is evident that the irreducible representations A_1 and B_2 contain both a change in dipole moment and a change in polarizability. Therefore, all three modes will be both IR and Raman active. The ν_1, ν_2, and ν_3 modes of water vapor have been observed in the Raman and IR spectra at 3651, 1595 and 3755.8 cm^{-1}, respectively, according to Herzberg[27].

Table 1.1 Character Table for point group C_{2v}

C_{2v}	E	C_2 (z)	σ_v(xz)	σ_v'(yz)		
A_1	1	1	1	1	T_z	α_{xx}, α_{yy}, α_{zz}
A_2	1	1	-1	-1	R_z	α_{xx}
B_1	1	-1	1	-1	T_x; R_y	α_{zx}
B_2	1	-1	-1	1	T_y; R_z	α_{yz}

Now, let's take a look at the degrees of freedom of water depicted in **Fig 1.2**. Note that in total there are nine degrees of freedom represented, including three translations, three rotations and three vibrations, as would be expected by the 3N rule. Also note that the vectors of the various movements transform according to the irreducible representation to which they are associated. For example, the vectors associated with the ν_1 vibration remain pointed in the same direction with the same magnitude upon applying each symmetry operation. Therefore, the characters of A_1 are all equal to one. As a second example, the vectors associated with ν_3 point in opposite directions upon applying the $C_2(z)$ and $\sigma_v(xz)$ symmetry operations and so the characters for those symmetry operations are negative one. Thus, the shape of molecular vibrations may be imagined by adhering to the symmetry properties of an irreducible representation. Another method of identifying the shape of molecular vibrations is symmetry coordinate analysis, explanations may be found in Cotton[22].

1.2.5.2 Vibrational Modes of CO_2 Molecule

Carbon dioxide, CO_2, is a linear molecule with an infinite axis of rotation, two 180° axes of rotation, two mirror planes parallel to the infinite axis of rotation, a mirror plane perpendicular to the infinite axis of rotation, a center of inversion and an infinite improper rotation axis. Therefore, CO_2 belongs to the $D_{\infty h}$ point group[28]. Since CO_2 is a linear molecule with three atoms, it should have a total of four vibrations, as shown in **Fig 1.3**. For the sake of brevity, the above procedure for reducing the vibrational degrees of freedom into irreducible representations has been omitted. The vibrations are a symmetric stretch (Σ_g^+), an anti-symmetric stretch (Σ_u^+) and a doubly degenerate symmetric bending mode (Π_u). Molecules that contain a center of inversion will have active IR and Raman vibrational modes that are mutually exclusive. And so for the case of CO_2, the Σ_g^+ is Raman active and the Σ_u^+ and Π_u modes are IR active.

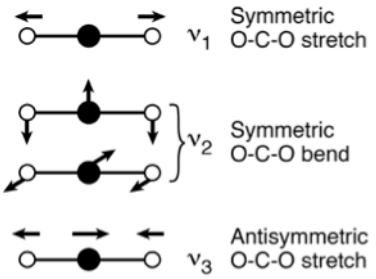

Fig 1.3 – The normal modes of vibration of CO_2 molecule.

The IR spectrum of CO_2 matches theory exactly, producing two absorption bands at 667.3 and 2349.3 cm^{-1} that are assigned to Π_u and Σ_u^+ respectively. The Raman spectrum of CO_2 diverges from theoretical predictions in that two Raman lines are seen, one at 1388.3 and another at 1285.5 cm^{-1}, instead of the one Raman line predicted by group theory. The average of the two Raman lines is nearly twice the value of Π_u and so the doublet is rationalized[27] by attributing the presence of the second Raman line to Fermi resonance between the Σ_g^+ and the first overtone of Π_u.

1.2.5.3 Vibrational Modes of MX_3 Molecule

There are two spatial orientations – trigonal planar and trigonal pyramidal – for molecules with the generic formula MX_3 where X represents those atoms bound to the central atom M. The highest symmetry these two molecular geometries may attain is D_{3h} and C_{3v} for trigonal planar and pyramidal, respectively, when all X are the same atom. Examples of trigonal planar molecular geometry include carbonate anions (CO_3^{2-}) and boron trifluoride (BF_3). Examples of trigonal pyramidal molecular geometries include ammonia (NH_3), phosphorous trichloride (PCl_3) and sulfite anion (SO_3^{2-}). What distinguishes trigonal planar molecules from trigonal pyramidal molecules is that trigonal pyramidal molecules have a lone pair of electrons bound to the central atom that repel the X atoms away from the plane that in turn reduces the symmetry of trigonal pyramidal molecules as compared to trigonal planar molecules.

Let us now use CO_3^{2-} as an example for how to apply group theory[23] to trigonal planar type molecules. CO_3^{2-} has a 120° rotations axis, three 180° rotation axes, a mirror plane perpendicular to the 120° rotations axis, three mirror planes parallel to the 120° rotations

axis, and an improper 120° rotation axis. Therefore CO_3^{2-} belongs to the D_{3h} point group. CO_3^{2-} should have six vibrations according to the 3N – 6 rule for non-linear molecules. Upon reducing the vibrational degrees of freedom to irreducible representations, it is found that CO_3^{2-} has vibrations with characters of A_1', E', E', and A_2'', which is in accord with theory. The single and double dashes associated with an irreducible representation connote symmetry or anti-symmetry with respect to the perpendicular mirror plane (σ_h), respectively. The modes which are IR active include the E' and A_2'' modes while the A_1' and E' modes are Raman active. The Raman active, totally symmetric stretching mode A_1', vibrational mode appears at 1088 cm^{-1} in the Raman spectrum. The two doubly degenerate anti-symmetric stretching and bending modes (2E') appear at 1438 and 714 cm^{-1} in both the IR and Raman spectra. Lastly, the out-of-plane bending mode A_2'' appears at 880 cm^{-1} in the IR spectrum only.

Now let us use NH_3 as an example of trigonal pyramidal type molecules. NH_3 has a 120° rotations axis and three mirror planes parallel to the rotation axis. Therefore, NH_3 belongs to the C_{3v} point group. Upon reducing the vibrational degrees of freedom to irreducible representations, it is found that NH_3 has vibrations with characters A_1, A_1, E and E. All A_1 and E vibrational modes are IR and Raman active. The A_1 vibrational modes correspond to totally symmetric stretching and bending modes, which appear at 3336 and 950 cm^{-1} in the Raman spectrum, respectively. The E vibrational modes represent anti-symmetric stretching and bending modes, present at 3444 and 1626 cm^{-1} respectively[29].

1.2.5.4 Vibrational Modes of MX_4 Tetrahedral Molecule

A number of minerals including perchlorate, silicates, and sulfates have basic building blocks that have tetrahedral symmetry. The symmetry of these MX_4 molecules or ions is that of point group T_d. The total number of normal modes of vibration for MX_4 is nine. According to group theory, these modes of vibrations can be classified according to the irreducible representation of the T_d point group as $\Gamma_{Td} = A_1$ (R) + E (R) + 2F (R, IR).

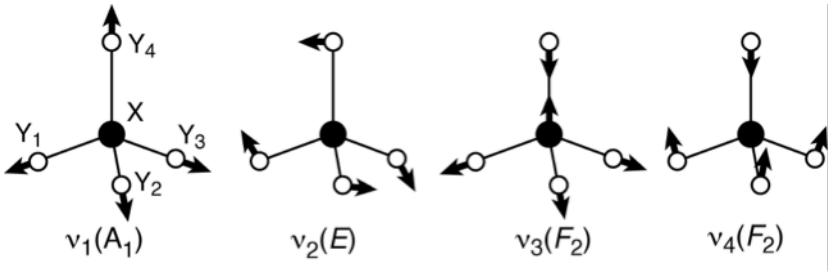

Figure 1.4 – Normal modes of vibrations of MX_4 molecule.

Figure 1.4 gives one example for each of the four fundamental modes of vibrations of MX_4 molecules, degenerate vibrations not included. For isolated silicate ions[4], the totally symmetric Raman active ν_1 (A_1) line appears at 819 cm^{-1}. The doubly degenerate Raman active symmetric bending mode ν_2 (E) appears at 340 cm^{-1}; and the triply degenerate anti-symmetric stretching ν_3 (F), and anti-symmetric bending modes, ν_4 (F), appear, respectively, at 956 and 527 cm^{-1}.

1.3 Classification of Crystal Vibrations

In crystalline solids, atoms are arranged in a periodic lattice and strong forces exist between neighboring atoms. If one atom is displaced from its mean equilibrium position, the neighboring atoms also undergo displacements. Therefore, the atomic motions in solids are collective rather than individual. These motions give rise to normal modes of vibrations, which travel as a wave through the crystal. Furthermore, the energy of these waves is quantized. The pseudo-particles associated with these waves are referred to as phonons, by analogy with the term photon for a quantized unit of light energy.

A crystal containing N atoms in the primitive cell has 3N degrees of freedom, of which three are associated with the translation of the unit cell as a whole and thus become acoustic modes. The acoustic modes are responsible for the propagation of sound waves through the crystal lattice. Thus, the number of lattice vibrations that may be observed by Raman and infrared spectroscopy is equal to 3N-3 and are referred to as “optical modes”. The transverse and longitude modes are referred to as TO and LO modes, respectively.

A classification of the crystal vibrational modes into internal (molecular) and external (lattice) vibrations is commonly accomplished by two approximations. The first commonly

used method is called factor group analysis. A factor group is defined as the group formed by the symmetry elements present in the smallest unit cell, which is called a Bravais cell. The Bravais cell is defined in such a way that the pure lattice translations of the unit cell can be used to obtain the entire space group. A factor group is always isomorphous with one of the 32 crystallographic point groups[30].

The analysis of the vibration at k = 0, the center of the Brillouin zone, for the entire crystal can be accomplished by two principal methods. The first is the factor group method of Bhagavantam & Venkatarayudu[31] that considers the atoms in the Bravais unit cell as a large molecule. The crystallographic unit cell may be identical with the Bravais cell or it may be larger by some simple multiple. For example, for all x-ray crystal structures designated by a symbol P (for primitive) or R (rhombohedral primitive), the crystallographic unit cell and Bravais unit cell are identical. Crystal structures designated by capital letters I, A, and C have unit cells that contain two Bravais cells. Crystal structures designated by capital letter F (Face-centered) have unit cells that contain four Bravais cells. For factor group analysis[32-33] the number of molecules per crystallographic unit cell should be divided by the cell multiplicity, e.g., by four for an F cell, by two for I, A, and C cells, and one for P and R cells. Adams & Newton[34-35] established tables for factor group analysis of vibrational modes for all space groups.

The second commonly used method is called the site group method of Halford[36], which involves deriving the number of allowed modes of specific molecular entities based on site symmetry of the molecule in the unit cell. It is an approximation that can be used for molecular crystals such as carbonates, sulfates, and phosphates, where the forces between molecules are considerably weaker than those between the atoms inside the molecules. Hornig[37] and Winston[38] discuss the relationship of the factor group method to the site group method. These authors showed that it is possible to get equivalent results using either of the methods. Maraduddin[39] and Warren[40] provide in depth discussion on factor group analysis for the full Brillouin zone. Based on factor group analysis, Ferraro[41] lists selection rules for some common minerals. Fateley[32] developed the correlation of the site group to the factor group. DeAngeles[42] and Fateley[32] summarized the procedure to perform calculations for the zone center (k = 0) phonons. To assist with the analysis of vibrational modes in crystals, a set of online databases is available that includes data from

international tables, space-groups, and point groups, symmetry relations between space groups, and a k-vector database with Brillouin zone figures and classification tables of the wave vectors for space groups[43-45].

The essentials of factor group analysis are illustrated below for calcite and aragonite polymorphs of calcium carbonate minerals. The rhombohedral primitive cell of calcite (space group #167, D_{3d}^6 ($R\bar{3}c$)) contains two $CaCO_3$ formula units for a total of ten atoms. Its 27 (3N-3) vibrational modes can be classified according to the irreducible representations of the D_{3d} point group as follows:

$$\Gamma_{D3d} = 1A_{1g}\,(R) + 4E_g\,(R) + 3A_{2g}\,(i.a.) + 2A_{1u}\,(i.a.) + 3A_{2u}\,(IR) + 5E_u\,(IR) \quad (1.15)$$

where R = Raman active, IR = IR active, and i.a. = inactive mode.

At room temperature, in the polarized Raman spectra of oriented single crystal of calcite, the following fundamental internal modes of the CO_3 ion are detected[46]: $\nu_1(A_{1g})$ = 1088 cm^{-1}, $\nu_3(E_g)$= 1434 cm^{-1}, and $\nu_4(E_g)$=711 cm^{-1}. In addition to the vibrational modes of the CO_3, two doubly degenerate E_g translational and rotation lattice modes of calcite are observed at the 156 and 283 cm^{-1}, respectively. Finally, the Raman line observed at 1750 cm^{-1} is a combination (ν_1+ν_4) mode.

The orthorhombic cell of aragonite (space group #62, D_{2h}^{16}-Pnma) contains four formula units for a total of 20 atoms. Fateley[32] classified aragonite's 57 vibrational modes as follows:

The irreducible representations of the D_{2d} point group is

$$\Gamma_{D2d} = 9A_g\,(R) + 6A_u\,(i.a.) + 6B_{1g}\,(R) + 8B_{1u}\,(IR) + 9B_{2g}\,(R) + 5B_{2u}\,(IR) + 6B_{3g}\,(R) + 8B_{3u}.\,(IR) \quad (1.16)$$

Of the 30 Raman active fundamental modes of aragonite, 28 have been identified in single crystal measurements[47] at 80 K. The following internal modes of vibrations of CO_3 were detected: four A_g (705, 854, 1087.2, and 1466.2 cm^{-1}), two B_{1g} (705.9 and 1464.1 cm^{-1}), three B_{2g} (716.9, 911.1 and 1579.0 cm^{-1}), and one B_{3g} (700.1 cm^{-1}). On the basis of theoretical calculations, De La Pierre[47] concluded that the two internal modes B_{2g} (1091.6 cm^{-1}) and B_{3g} (1415.0 cm^{-1}) have zero intensity. Due to the low intensities of these bands, they could not be detected[47] in the Raman spectra.

All the Raman active lattice modes anticipated based on the factor group analysis of aragonite structure were detected in the single crystal measurement. These include the following: five A_g (144.7, 166.1, 199.2, 219.9, and 291.5 cm^{-1}); four B_{1g} (117.9, 156.2, 211.7, and 227.0 cm^{-1}); five B_{2g} (184.6, 212.8, 252.5, 267.0, and 284.1 cm^{-1}); and four B_{3g} (101.3, 167.6, 177.8 and 271.2 cm^{-1}).

1.4 Experimental Methods

Raman spectroscopy was initially considered a physics curiosity until the invention of lasers because the intensities of Raman lines are extremely weak without a high intensity monochromatic light source. This was despite the fact that Raman studies of several minerals and pure compounds had been carried out at the macroscopic scale using 404.6, 435.8, and 253.65 nm light from mercury emission lamps as the excitation (λ_0) source. Lasers that became available during the 1960s were able to provide high irradiance of monochromatic light onto samples for recording the Raman spectra. The following sub-sections outline the advancements in: (i) continuous-wave (CW) and pulsed laser excitation sources; (ii) Raman dispersive spectrometers and interferometers; (iii) detectors used for Raman measurements with CW and pulsed lasers, respectively; and (iv) advances in micro-Raman and remote Raman instrumentation.

1.4.1 Excitation Laser Sources

Various lasers used for exciting Raman spectra of samples can be classified into two basic categories: (i) CW laser sources and (ii) pulsed laser sources.

1.4.1.1 CW Lasers

In modern Raman spectroscopy systems, three types of CW ionized-gas lasers are in use: Ar-ion, Kr-ion, and mixed Ar-Kr-ion lasers. The wavelengths of these lasers are stable and known within an accuracy of ~ 1 pm which corresponds to 0.04 cm^{-1} around 500 nm. When operated in constant output power modes, these lasers produce laser radiation with long-term power stability of better than 1%. These medium and high power (1 to 2 W at 514.5 nm) Ar-ion and Kr-ion lasers can deliver different excitation lines over a wide spectral range. The main laser lines usually used for Raman spectroscopy are: **514.5**,

488.0, and 457.9 nm for Ar-ion lasers; and 532.9, 566.2, **647.1**, and 676.4 nm for Kr-ion lasers. The laser lines in bold are the strongest lines from these lasers. UV excitation lines may be obtained with high power Ar-ion and Kr-ion lasers with intracavity frequency doubling. The mixed Ar-Kr-ion lasers deliver many lines, each corresponding to an end-member gas. Laser line filters or pre-monochromators may be used to eliminate plasma line emissions. Alternatively, plasma lines from the gas medium may be allowed to pass through and be used as a wavelength standards[48] for calibrating Raman spectrographs.

The CW He-Ne laser, which is known for its red line at 632.8 nm, are also used in Raman spectroscopy with single monochromators equipped with laser rejection filters. Another gas laser includes the He-Cd laser, which delivers radiation at 441.6 nm (output power <180 mW) and 325 nm (50 mW), and is mainly used for UV excitation.

The compact UV hollow cathode NeCu ion-lasers, which emit CW radiation at 248.6 nm with output power greater than 50 mW[49] have recently been selected as the excitation source for the SHERLOC instrument on NASA's Mars 2020 rover mission[50].

Diode Pumped Solid State (DPSS) CW Nd:YAG lasers that emit fundamental radiation at 1064 nm with output power of several watts are commonly used as an excitation source with Fourier Transform Raman spectrometers (FT-Raman). The line width is <1 cm^{-1} in standard lasers. In addition to the 1064 nm laser wavelength, radiation at 532, 355, and 266 nm can be obtained with frequency doubling, tripling, and quadrupling crystals.

Single mode, frequency stabilized near infrared 785 and 830 nm diode lasers with linewidth <1 cm^{-1} are increasingly finding applications[51-56] in Raman spectroscopy as excitation sources. When excited with near IR lasers, the Raman spectra of some minerals and related materials display strong laser-induced fluorescence lines from rare-earth elements, which may be mistakenly identified as Raman lines[57-58].

1.4.1.2 Pulsed Laser Sources

In the past, flash lamp pumped or DPSS Nd:YAG pulsed 532 nm laser excitation sources were not usually used for exciting Raman spectra of geological samples. This was because a focused ns-pulsed beam could damage the samples when used in 180° scattering geometry. Sharma[59] demonstrated that a 532 nm pulsed laser could be used by focusing the expanded excitation beam in a 135° scattering geometry and collecting the scattered beam

with a 20x objective. A spectrally narrowed (<0.1 nm), 532 nm, passively Q-switched micro-chip laser with 600 ps pulses (1.5 μJ, 40 kHz) has also been used to measure the micro-Raman spectra of minerals in 180^{o} scattering geometry[60].

1.4.2 Dispersive Spectrometers and Interferometers

Both grating-based dispersive and interferometer-based Raman spectrometers have been developed for measuring Raman spectra of minerals, inorganic and organic materials. The following gives a brief description of these two types of Raman spectrographs.

1.4.2.1 Dispersive Raman Spectrographs

In modern spectrographs, an important component is the dispersing element. Two types of gratings are available: transmission gratings and reflection gratings. Dubessy[8] reviewed the properties of various gratings. Holographic gratings are used to efficiently reject stray light and eliminate ghost lines in the spectrographs. Both plane and concave holographic gratings are used in commercial Raman spectrometers[61-63]. Most dispersive Raman spectrographs employ the Czerny-Turner configuration. The aperture of Czerny-Turner optics is limited to F/4 or slower in order to minimize comma and spherical aberrations.

In the past two decades, the technology of Volume Phase Holographic gratings (VPHG) has been widely exploited in the field of Raman spectroscopy for instrumentation[64-65] that works both in the visible and in the near infrared. VPHG have very large diffraction efficiency even at very high dispersion and are easy to customize because each VPHG is a master grating. In VPHGs the diffraction of light occurs due to a periodic modulation of the refractive index in the volume of an active material such as dichromate gelatin (DCG)[64]. These holographic gratings have found applications in Raman instrumentation[64,66]. These gratings have been instrumental in developing compact and high throughput Raman spectrographs for planetary applications[67-69].

Due to the low (~10^{-7}) efficiency of Raman scattering and potential high efficiency of Rayleigh (10^{-3}) scattering combined with reflection of the laser excitation radiation (λ_0), rejection of λ_0 radiation before it reaches the detector must be achieved to avoid detection of unwanted light. In the past, double and triple Czerny-Turner spectrographs were

developed[54] to measure low-wavenumber Raman spectra. Efficient rejection of the excitation λ_0 laser radiation has been made possible with advanced holographic notch filters and dielectric edge filters, which allows the use of only a single stage Czerny spectrograph for Raman scattering measurements down to 50 cm^{-1}. In the past six years ultra-narrow holographic notch filters have been developed[70] that allow the measurements of Raman lines down to ~ 10 cm^{-1}.

1.4.2.2 Fourier-Transform Raman Spectrometers

The development of laboratory based FT-Raman spectrometers based on Michelson interferometers was motivated with the possibility of (i) achieving higher-resolution than is possible with the dispersive grating based instruments[71]; and (ii) measuring near-IR excited Raman spectra of materials that are highly fluorescent when excited with visible radiation[72-73]. In FT-spectrometers, the limiting resolution does not depend on the size of the entrance slit so high spectral resolution can be achieved without sacrificing the optical throughput. Multichannel FT-Raman systems that combine a common-path interferometer with near IR laser excitation[74-75], and spatial heterodyne interferometers with 532 and UV pulsed laser excitations have been developed[76-78]. The multichannel FT-Raman systems with pulsed laser and gated ICCD detectors do not have any moving parts, thus offering an advantage for standoff measurements under high ambient light environments.

1.4.3 Detectors for Raman Measurements with CW Lasers and Pulsed Lasers

Various detectors used in CW and time-resolved modes with pulsed lasers are briefly discussed in the following subsections.

1.4.3.1 Detectors for Raman Measurements with CW Lasers

Single channel photomultiplier tubes (PMT) were used during 1960-1980 for Raman spectroscopy. These PMT detectors were used in the first Raman microprobes at ambient pressures[61,79] as well as in high-pressure Raman with the diamond anvil cell[80-81]. In the mid-1980s, the first popular multichannel detectors[82] were linear intensified photodiode arrays of 1024 pixels with dimensions of 3 mm x 24 μm. These diode array detectors significantly reduced the measurement time as 1024 spectral wavelength could be

measured simultaneously in 1 sec, however, the spectral resolution was degraded because of the size and number of pixels. Charge-coupled device (CCD) cameras appeared in mid-1990 and replaced all the other detectors because of their high quality. The CCDs are made up of two-dimensional arrays of individual pixels. The common dimensions of CCD used in laboratory Raman spectrographs are 1024 x 256 pixels. The pixel size is typically 26 μm x 26 μm. The dynamic range of most laboratory CCDs is 16 bit (e.g., maximum counts 65536 = 2^{16}).

1.4.3.2 Detectors for Raman Measurements with Pulsed Lasers

Minerals and rocks containing transition metal and rare-earth ions can produce luminescence spectra that in some cases overlap with their Raman spectra. The lifetime of mineral photoluminescence is much longer (μs to ms) as compared with the lifetime of the Raman signal that is ~10^{-13} s. The difference in the lifetime of Raman scattering and fluorescence has been exploited to minimize interference by luminescence with the Raman spectra by using pulsed laser excitation and a gated detection[83-86]. Raman spectrometers equipped with intensified CCD (ICCD) detectors or single-photon avalanche diode (SPAD) array detectors and pulsed laser excitation allow measurements of Raman spectra of minerals with minimum interference from photoluminescence as well as from ambient light[60,85,87]. The ICCD detectors normally allow gating down to 2 ns and the SPAD arrays offer gating down to 0.5 ns thus effectively minimizing interference from mineral photoluminescence and short-lived fluorescence (>0.5 ns) from organic and biological molecules, respectively.

1.4.4 Advances in Micro-Raman and Remote Raman Instruments

In past two decades, significant advances have been made both in the micro-Raman and remote Raman instrumentation. These advances in Raman instrumentation are briefly outlined below.

1.4.4.1 Advances in Micro-Raman Spectroscopy

Figure 1.5 shows a schematic of a micro-Raman system with continuous wave (CW) Ar-ion laser, 488 and 514.5 nm radiation used in 180-degree excitation, and a pulsed

frequency-doubled 532-nm Nd:YAG laser used in an oblique (typically 135-degree) angle excitation.

One of the principal advantages of micro-Raman spectroscopy is the ability to make measurements on a region of a sample the same size as the focused laser spot. The laser can be focused to a diffraction limited spot such that the system will accept light from other areas such as above and below the nominal focus area in an on-axis configuration (e.g., backscattering geometry). Insertion of a pinhole in the optical path in the image plane as shown in **Figure 1.5** will make the Raman system confocal, allowing rejection of out of focus signal as well as spurious light from other sources. Use of 135-degree-excitation geometry also avoids the generation of scattered light within the collection optics that may interfere with the weak light scattered from a sample.

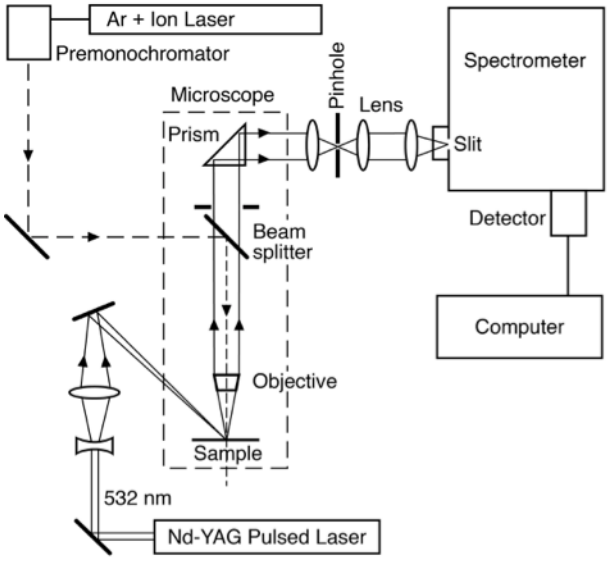

Figure 1.5 – Schematics of a confocal micro-Raman system with 180° and 135° scattering geometry with a CW Ar-ion laser and a pulse 532 nm laser, respectively.

Fully automated commercial confocal Raman instruments are available from many companies including Renishaw *inVia* Raman microscope (Renishaw, Gloucestershire UK), WITec *alpha300* confocal Raman system (WITec GmbH, Ulm, Germany), and F/1.8 Raman *RXN microprobe* (described by Battey[66]; Kaiser Optical Systems, Inc., Arbor, MI, USA). The *inVia* Raman microscope has the option of focusing the laser beam on a spot or line on the sample. The spectral image of the sample can be obtained by rasterizing the sample under the laser focus and moving from point to point on the sample until the desired area is

mapped. By focusing the laser on a line rather than a spot, the resulting image can be focused on the slit and subsequently imaged on the CCD detector. The x-axis on the CCD will be the Raman shift and y-axis will show variation in the spectra of the sample. The line focus allows the use of higher laser power on the sample as compared to the point focus, and allows a faster spectral image of the sample as multiple points along the line are measured simultaneously.

Advances in notch and sharp edge filters have significantly reduced the size and increased the efficiency of dispersive Raman systems. SuperNotch filters allows the rejection of the Rayleigh scattered light by a factor of $\sim 10^8$ thereby eliminating the need for a filter-stage in modern Raman spectrometers. These advances have been used to develop research-grade miniature Raman spectrometers for space applications[69,88] as well as commercial miniature Raman spectrometers (for a review see Dubessy[8]).

1.4.4.2 Advances in Remote Raman Instrumentation

Telescopic Raman systems equipped with an intensified CCD camera using 532-nm pulsed laser with 10 ns pulses have been developed for measuring time-resolved remote Raman spectra of minerals during day and night[68,84,89-91].

In recent years, remote Raman systems based on spatial heterodyne Raman spectrometers[76,78] (SHRS) using both 532 nm and UV pulsed lasers have been developed for measuring time-resolved Raman spectra of inorganic and organic compounds. SHRS is a variant of a Michelson interferometer in which the mirrors of a Michelson are replaced with two stationary diffraction gratings. When light enters SHRS, the light is split 50/50 by a beam splitter and directed unto two diffraction gratings. The light is reflected off the diffraction gratings in the first order at frequency dependent angles that in turn produce crossed wavefronts in space that can be imaged by a plane array detector. The greater the angle of reflection is relative to the optical axis, the greater the frequency of the spatial fringe. The crossed wavefronts, which represent a superposition of spatial interference fringes, are converted to Raman spectra upon Fourier transformation. The principle advantages of SHRS over dispersive-based Raman spectrometers include SHRS' lack of an entrance slit, thus allowing many more photons to be recorded than dispersive-based instruments, and SHRS' ability to measure large laser spot sizes without sacrificing signal-

to-noise ratio or resolution. Quantitative explanations of the angles of reflection, formation of spatial fringes, and conversion of an image corresponding to a superposition of spatial fringes to a Raman spectrum will be provided in **Chapter 2**, **Sections 3** and **Chapter 3, Section 3**.

Using SHRS and 532 nm pulsed laser excitation, Egan[92] measured Raman spectra of weak Raman scatterers such as feldspars and olivine minerals (**Fig 1.6**). These spectra show well resolved Raman fingerprint modes[93-94] of four-membered TO_4 rings in microcline at 475, 484, and 513 cm^{-1}, and in plagioclase at 481 and 509 cm^{-1}. The Raman fingerprints of olivine, which includes a doublet consisting of well-resolved lines at 824 and 855 cm^{-1}, have been observed with high resolution with SHRS (**Fig 1.6**).

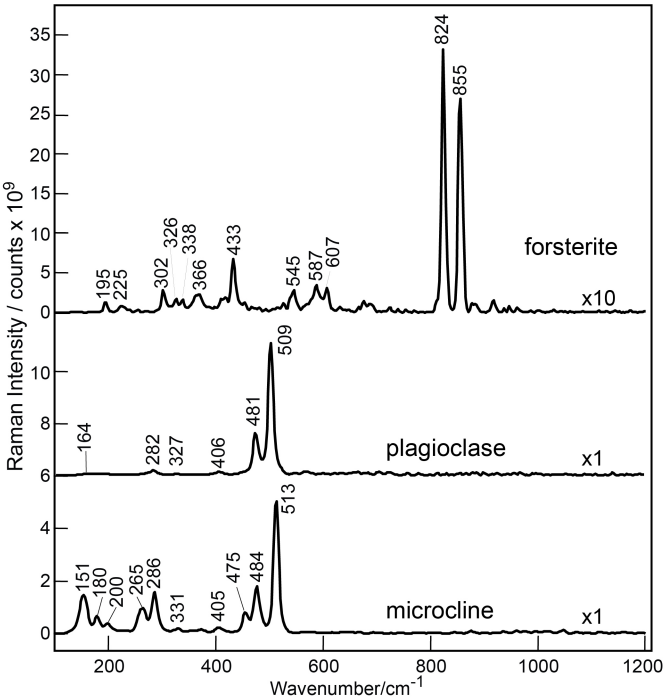

Figure 1.6 – The Raman spectra of feldspars, specifically microcline, plagioclase and forsteritic olivine in the 100-1200 cm^{-1} region at a distance of 0.5 meters. The laser used in this experiment was a 532 nm, 100 Hz, 8.6 mJ per pulse. The accumulation time was 50 seconds for olivine and 60 seconds for plagioclase and microcline.

1.5 Raman Spectra of Planetary Ices and Geological Materials

1.5.1 Raman Spectra of Planetary Ices

Raman spectroscopy can detect homopolar molecules such as H_2, N_2, O_2 etc…, which do not absorb in IR as well as heteropolar molecules. Raman spectroscopy has been successfully adopted by a number of scientists for *in situ* investigation of irradiated frozen ices[95-97] containing organic molecules, crystalline and amorphous water ice films on metal surfaces. Micro-Raman techniques have been used in the laboratories to study the effects of ion-induced lattice damage in carbonaceous solids and organic compounds in frozen planetary ice analogs[96,98-100]. Bennett[101] developed a novel high sensitivity Raman spectrometer to study pristine and irradiated interstellar ice analogs. These scientists measured *in situ* Raman spectra of thin films of CO_2 ices of 10 to 396 nm thickness at 4.5 K under ultrahigh vacuum. The Fermi resonance doublet of CO_2 ice was detected at 1385 and 1278 cm^{-1}, which is in good agreement with previous studies. To evaluate the effect of irradiation on CO_2 ice, a CO_2-ice film (450 nm thick) was deposited at 4.5 K and subjected to 1 hour of irradiation from 5 keV electron beam over an area of 1.6 cm^2. The Raman spectrum of the irradiated CO_2 film detected the presence of two new species, namely CO at 2145 $cm^{-1}$and O_2 at 1545 cm^{-1}, in the film[101].

1.5.2 Raman Spectra of Geological Materials

Advances in the Raman instrumentation have enhanced the applications of Raman spectroscopy in nearly all geological and planetary disciplines. Fluid inclusions in various geological and extra-terrestrial materials have been studied with Raman spectroscopy[79,102-104]. The major strength of Raman spectroscopy in studying fluid inclusions is that the technique is capable of nondestructively analyzing single small (>5 μm) inclusions[105]. Raman spectra of minerals, glasses and melts of mineral compositions have also been investigated as these provide information about short range and intermediate range structural orders[55,81,106-119].

Raman spectroscopy can provide structural information about minerals, glasses and melts. For example, a comparative study[109,120-122] of the Raman spectra of silicate minerals and corresponding glasses led to reassignment of the two weak, sharp, and polarized peaks at 490 and 606 cm^{-1} in the Raman spectrum of SiO_2 glass (see **Fig 1.7**). The 490 and 606

cm^{-1} bands have been assigned, respectively, to symmetric stretching of oxygen atoms of four and three-membered rings of SiO_4 tetrahedra in the disordered three-dimensional network.

These ring modes are vibrationally decoupled from rest of the network, remaining highly localized within the rings, which explains their narrow width compared to the rest of the glass spectrum. A micro-Raman study[7,123-124] of a silica polymorph moganite, which contains four-membered rings of SiO_4, found a strong Raman band at 501 cm^{-1}. This observation further confirmed that the lines in the range 500-512 cm^{-1} are the Raman fingerprints of the four-membered rings of tetrahedra in tectosilicate minerals, glasses and melts of mineral compositions.

A number of scientists[7,122,125-127] have reviewed extensive work on Raman spectroscopic investigations of the structure of silicate glasses and melts of interest in earth science, which have had a profound effect on our understanding of magmatic processes.

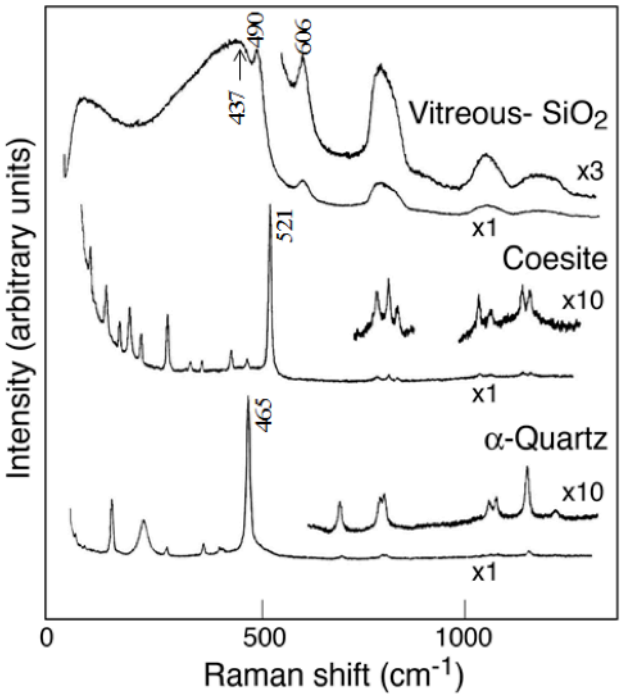

Figure 1.7 – Raman spectra of α-quartz, coesite, and vitrous-SiO2 (Modified from Sharma et al 1981).

Micro-Raman and confocal Raman instruments are being used for identification of mineral phases in rocks and meteorite samples[128-130]. For example, Acosta[131] used micro-Raman mapping of mineral phases in a thin section of a strongly shocked Taiban ordinary chondrite. The Raman spectra was excited with various laser excitation wavelengths (e.g., 244, 514.5, 785, and 830 nm), which allowed identification of mineral phases such as olivine, wadsleyite, ringwoodite, high-Ca clinopyroxene, majorite-pyrope, jadeite, maskelynite, and lingunite. Olivine was found to be Fe depleted (Fo_{88}) in contact with the ringwoodite as compared to olivine (Fo_{94}) separated from ringwoodite grains, which suggests chemical fractionation during a solid-state olivine-ringwoodite transformation. Raman imaging revealed a close correlation between the blue ringwoodite color and the peak observed at 877 cm^{-1}. This signal[131] showed a strong near-resonance Raman enhancement when measured with near-IR laser excitations (785 and 830 nm) close to the optical absorption bands of four-fold coordinated Fe^{2+} in the ringwoodite. The near IR optical absorption is assigned[132] to the transition $^5T_{2g} \rightarrow {}^5E_g$ of $^{VI}Fe^{2+}$ split by the trigonal distortion or Jahn-Teller effect.

Micro-Raman spectroscopy has also been successfully used to investigate mineralogy and phase transitions under high pressure and temperatures to gain insight into the Earth and planetary interiors[112,133-136].

1.6 Outline of Thesis

In this chapter, the author described the theory and instrumentation of Raman scattering. Raman scattering is a phenomenon characterized by the inelastic scattering of light by a molecule that has a normal mode of vibration capable of producing an instantaneous induced dipole moment when radiation is incident upon said molecule. The phenomenon of Raman scattering may be modeled mathematically by two methods – classical electrodynamics and quantum mechanics. The quantum mechanics model is superior to the classical electrodynamics model because the quantum mechanics model accurately predicts the relative intensities between Stokes and anti-Stokes Raman lines. The activity of vibrational modes in the Raman spectrum can be predicted via group theory by first identifying all the symmetry elements of a molecule or mineral, classifying said

molecule into a point or space group, followed by removal of superfluous degrees of freedom and finally disambiguation of the vibrational degrees of freedom into irreducible representations. A vibrational mode is active in the Raman (IR) spectrum if the vibrational mode, as represented by an irreducible representation, contains a change in polarizability (change in dipole moment).

This chapter also discussed the advancement of Raman instrumentation components such as excitation sources, spectrographs and detectors. The most commonly used lasers for Raman spectroscopy were discussed, including continuous wave noble gas lasers, and solid state pulsed lasers, highlighting the use of different wavelengths to solve unique problems. This chapter gave examples of the most effective Raman spectrometers – dispersive and interferometric – and discussed the advantages of each type. This chapter also talked about the use of two-dimensional multichannel detectors such as ICCD and SPAD and how these detectors allow for excellent spectral resolution, dynamic range and flexibility when measuring Raman spectra in ambient light conditions. Finally, this chapter presented the Raman spectra of various minerals of importance to the planetary science community as characteristic spectra that prove the usefulness of Raman spectroscopy.

The impetus of this thesis is to determine whether or not SHRS can be used for planetary surface exploration, whether it is currently superior to existing dispersive-based Raman spectrometers, and whether it could be superior to existing instruments in the future. In answering these questions, the phenomenon of Raman scattering and instrumentation of Raman spectroscopy as utilized for planetary surface exploration was defined in the present chapter. In Chapter 2, the author turns specifically to the application of SHRS to the measurement of Raman spectra of carbonate, sulfate, and silicate minerals at distances of 0.5 meters in order to test the feasibility of using SHRS for planetary surface exploration. In Chapter 3, the author presents a novel data reduction procedure that allows for the recording of Raman spectra of important mineral groups, inorganic salts and organics for the exploration of planetary surfaces with SHRS at distances of up to 5 meters. Finally, in Chapter 4, the author takes account of the lessons learned from the preceding chapters and recommends some future work.

Chapter 2: Standoff Spatial Heterodyne Raman Spectrometer for Mineralogical Analysis

(This chapter was published online by the *Journal of Raman Spectroscopy* on March 7, 2017. DOI 10.1002/jrs.5121)

Raman spectroscopy is ideally suited for planetary exploration because of its ability to unambiguously identify minerals, organic compounds, and biomarkers. Traditionally, Raman spectra were acquired with grating-based dispersive spectrometers that require tens of micrometer sized entrance slits and thus limited light throughput. Recently, the author evaluated a new type of Fourier transform (FT) Raman spectrometer, the spatial heterodyne Raman spectrometer (SHRS), that provides high spectral resolution in a compact system without limiting light throughput. This work presents time-resolved Raman spectra of carbonate, sulfate, and silicate minerals, including low Raman scattering efficiency olivine and feldspar minerals, in the 100-1260 cm^{-1} Raman fingerprint region with SHRS using 1.5 cm diameter pulsed 532 nm Nd:YAG laser beam.

2.1 Introduction

For planetary surface exploration, Raman spectra of minerals, organic compounds and biomarkers are typically measured with dispersive spectrometers that require narrow entrance slits to achieve high resolution, which concurrently restricts light throughput. In order to overcome this limitation, Fourier transform (FT) Raman instruments have been developed over the years in order to take advantage of the properties of FT instruments, such as Jacquinot's advantage, multiplex advantage, constant resolution, wide acceptance angle, and field of view. However, FT instruments frequently require moving optics and are relatively large in size, which make them unsuitable for planetary exploration. The spatial heterodyne spectrometer (SHS), which combines the ruggedness of a dispersive spectrometer with the high resolution and throughput of an FT instrument, is ideal for planetary exploration when characterization of large areas is sought.

SHS was first developed by Harlander's group[1-4] in order to bring the advantages of interferometry described above into the ultraviolet (UV) regime and has since been

extended to many other applications that generally fall into two categories. First, SHS has been used to measure various forms of scattering and emission spectra from extreme UV to the near infrared, including Raman spectra of organics, inorganic salts, pharmaceuticals and minerals[5-11], atomic emission spectra of brass alloys[12], and emissions by particles in various strata of the atmosphere[13-14]. The second class of SHS experiments involves measuring the Doppler shift of emission lines in order to estimate velocity distributions, notably wind velocity measurements from ground[15] or satellite based instruments.

The relationship between resolution and throughput of SHRS as compared to a single stage dispersive Raman spectrometer (Kaiser Holospec f/1.8 with 100 micron slit) has been discussed by Gomer et al.[5] The author Gomer[5] has compared the response of a dispersive spectrometer and SHRS as a function of 532-nm laser spot size (from 0.2 cm to 8 cm) on a sulfur sample under identical laser power (100 mW). It has been found that the SHS maintains identical peak intensity for the 463 cm^{-1} Raman band of sulfur regardless of the beam diameter. For the dispersive system, the intensity of the peak drops significantly as the laser beam size increases, especially once the spot overfills the slit. Even though lower S/N ratios are expected with the SHS for small (<5 mm) laser beam diameter, the high optical etendue gives it an advantage for wide area targets that does not sacrifice intensity, S/N, or resolution, allowing it to outperform the dispersive spectrometer for wide area measurements with large spot sizes[5]. So far in the SHRS literature, the Raman spectra of molecules with relatively high Raman scattering efficiencies have been obtained and reported.[5-11] The goal of the current project is to test the limits of sensitivity of SHRS in measuring minerals over a large area of 1.5 cm diameter laser spot size with relatively low Raman scattering efficiency[16] that may be useful in planetary science applications. This work evaluates SHRS's ability to measure time-resolved Raman spectra of carbonate, sulfate and silicate minerals while simultaneously characterizing spectral resolution, throughput, acceptance angle, and field-of-view.

2.2 Mineral Samples

The rock-forming minerals (calcite, dolomite, anhydrite, gypsum, microcline, plagioclase, and forsterite) were purchased from Ward's Natural Science Establishment, Inc. (Rochester, NY, USA). The carbonate minerals calcite and dolomite were, respectively,

from Chihuahua, Mexico, and Bamble, Norway. The sulfate minerals anhydrite and gypsum samples were, respectively, from Windsor Nova Scotia, Canada, and Washington County, Utah, USA. The feldspar samples microcline and plagioclase were from Essex County New York and Crystal Peak Colorado, respectively. Electron microprobe analysis showed that the composition of the major phase in the microcline sample was $Ab_{5.48}An_{0.03}Or_{94.3}$, where Ab = albite ($NaAlSi_3O_8$); An = anorthite ($CaAl_2Si_2O_8$); and Or = orthoclase ($KAlSi_3O_8$). The sample originally labeled as orthoclase was largely a plagioclase with composition of $Ab_{70.09}An_{21.18}Or_{2.78}$. The rock originally labeled forsterite contained fine-grained, light greenish minerals from Jackson County, North Carolina, USA. The sample was found to be a magnesium-rich olivine (Fo_{91}), (91% forsterite (Mg_2SiO_4) and 9% fayalite (Fe_2SiO_4). All samples were measured without cutting or polishing.

2.3 Experimental Method of SHRS at 0.5 meters

Figure 2.1 shows a schematic of the SHRS used in the present work. The basic spectrometer design has been previously described[6-8]. A diode-pumped frequency doubled 532 nm Nd:YAG, 100 Hz, 8.6 mJ per pulse laser is sent through a 2x beam expander, reflected off a mirror, and directed onto the sample. The spot size of the laser on the sample was 1.5 cm in diameter.

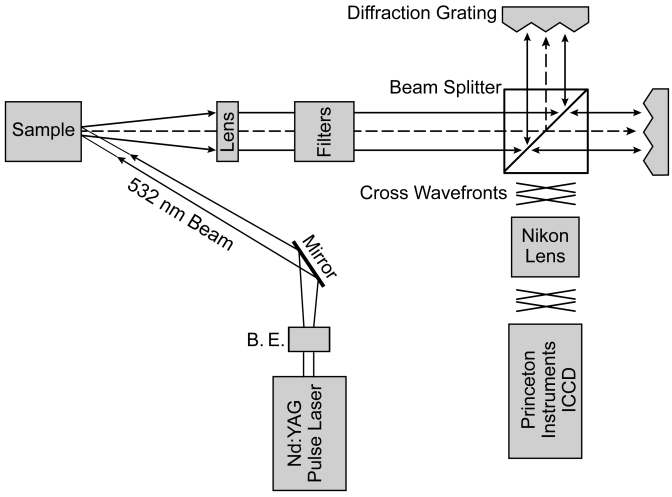

Fig 2.1 – Schematic diagram of SHRS utilized in the present work. B.E. stands for 2x beam expander.

All samples measured in this work were at a distance of 0.5 m from the collimating lens. The scattered light was collimated to infinity by a 25.4 mm lens (f = 0.5 m), and portions of the scattered light were attenuated via filters, specifically two 532 nm long-pass filters diminish Rayleigh scattered 532 nm Nd:YAG laser light, and a 525 to 575 bandpass filter minimizes longer wavelength radiation caused by fluorescence. The filtered light then enters the interferometer and its amplitude is split in two by a 50/50 silica glass cube beam-splitter, which directs the beams of light onto two tilted diffraction gratings. The diffraction gratings, which have 150 grooves per mm and are 25 mm square, are oriented to retro-reflect a desired wavenumber in the first order at the discretion of the experimentalist. The angle at which a given wavenumber is reflected is found by defining the angle of incidence, θ_i, and calculating the angle of reflectance, θ_r, in the grating equation[1], as shown in Eq. 2.1.

$$d(sin\theta_i + sin\theta_r) = m\sigma \tag{2.1}$$

where σ is a wavenumber, m is the order of light, and d is the distance between adjacent grooves on a grating in units of wavenumbers. A special case arises when the angle of incidence equals the angle of reflectance. This special case is known as the Littrow angle, θ_L, and is defined[1] by Eq. 2.2.

$$\theta_L = arcsin\left(\frac{m\sigma_0}{2d}\right) \tag{2.2}$$

The Littrow angle used in all spectra presented in this work was 2.2870°, which retro-reflects 532 nm light. The gratings retro-reflect σ_0 and produce planar parallel wavefronts from each grating that combine at the beam splitter, producing a fringe of constant intensity across the CCD. For wavelengths not equal to σ_0, wavefronts are diffracted at angles relative to the optical axis, which recombine at the beam-splitter as crossed wavefronts (**Fig. 2.1**). When these crossed wavefronts are imaged on the CCD, they produce a spatial fringe pattern, as described[1] by Eq. 2.3.

$$I(x) = \int_0^\infty B(\sigma)\{1 + cos[8\pi(\sigma - \sigma_L)xtan(\theta_L)]\}d\sigma \tag{2.3}$$

where B(σ) represents the input spectral intensity as a function of wavenumber, and x represents the position on the CCD array x-axis. Equation 2.4 describes the width of a spatial fringe[1].

$$f = 4(\sigma - \sigma_L)tan(\theta_L) \tag{2.4}$$

The interference pattern is focused at infinity by a Nikon f/1.8D lens and imaged by a Princeton Instruments intensified charge-coupled device (ICCD). The principle advantage of using an ICCD is its ability to produce a retarding voltage, which inhibits photons from being recorded by the CCD while the retarding voltage is activated. This permits Raman measurements to be made during daytime ambient light conditions, as the retarding voltage is deactivated exclusively during the interval when the laser pulse is incident on the detector.

2.4 Operating Procedure

Raman spectra were collected with SHRS in the following manner. First, an image is taken of the interference pattern, which henceforth will be called the "science image". Next, each of the two diffraction gratings is blocked, one at a time, with a piece of black paper. An image is then taken with settings identical to the science image. These two images represent the non-modulated contributions to the science image. The difference between the science and non-modulated images contains the modulated contribution to the science image. This image will henceforth be labeled the "modulated image". The Raman spectra may be acquired from either the science or modulated image by following the procedure detailed below. Spectra acquired from the modulated image have slightly better signal-to-noise ratio than those acquired with the science image and therefore will be the touchstone in the remainder of this work.

The modulated image is then integrated along the x-axis in order to create a one-dimensional interferogram. The direct current bias is removed by subtracting the mean of the interferogram, and the interferogram is apodized by a Gaussian window function so that the ends of the interferogram approach zero in order to reduce the magnitude of sidelobes in the instrumental line shape. The FT of this interferogram is taken, which results in a Raman spectrum, which is not phase or intensity corrected. Next, the phase of the Raman spectrum may be corrected by one of two equivalent methods. The first method involves summing the squares of the real and imaginary parts of the Raman spectrum, followed by taking the square root. The second method involves multiplying the real part of the Raman spectrum by the cosine of the phase and the imaginary part of the Raman spectrum by the sine of the phase, as described by Mertz[17] and Brault[18]. The phase

corrected Raman spectrum is inverse FT into a phase corrected interferogram and the power spectrum is calculated via Welch's method[19].

Finally, the intensity of the Raman spectrum is calibrated as a function of wavenumber. SHS is an amplitude-splitting interferometer with a sinc(σ) instrumental response. This effect was corrected by matching the relative intensities of an uncalibrated SHS spectrum of $CaCO_3$ to the relative intensities of the same $CaCO_3$ sample as measured using an intensity calibrated Renishaw Raman microscope. The intensity correction function, I(σ), and its implementation are shown in Eqns. 2.5 and 2.6.

$$I(\sigma) = \frac{1}{1+785.7e^{-0.0075\sigma}} \tag{2.5}$$

$$FT_{final} = FT_{phase\_correct} * I(\sigma) \tag{2.6}$$

Figure 2.2 illustrates the instrument response as a function of wavenumber and the intensity correction function calculated from the above method. The entirety of the data reduction procedure may be automated so that no manual human input is required except loading the science and background images as arrays.

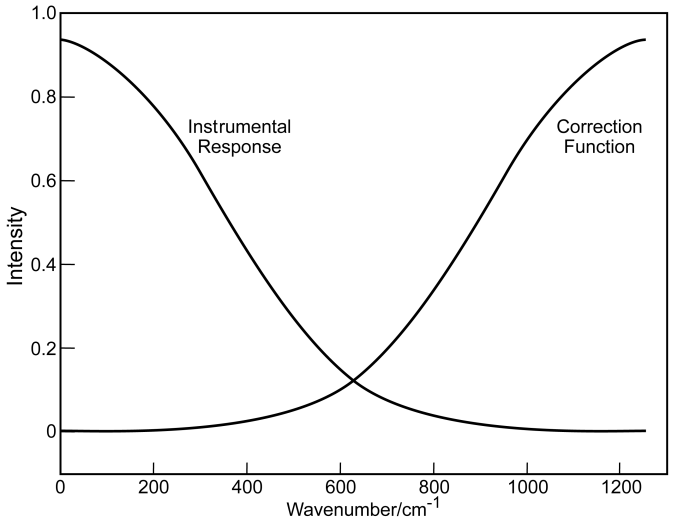

Fig 2.2 – The instrument response and intensity correction function as a function of wavenumber. The correction function was produced by matching the relative intensities of an uncalibrated SHS spectrum of calcite to that of the intensity calibrated spectrum of calcite taken with a Renishaw Raman microprobe.

2.5 Results and Discussion

The following sections describe the Raman spectra of minerals measured with SHRS, and the properties of SHRS in terms of its spectral resolution, bandpass and etendue. Minerals with high Raman cross-sections, such as calcite or dolomite, may be acquired in 1 second, and the Raman spectra of molecules with high Raman cross-sections such as sulfur may be acquired in as little as 10 milliseconds. Longer accumulation times were selected for presentation in this work in order to utilize the multiplex advantage of interferometers and to facilitate comparison between certain spectra.

2.5.1 Raman Spectra of Minerals at 0.5 meters

Figure 2.3 illustrates the Raman spectra of calcite ($CaCO_3$) and dolomite ($CaMg(CO_3)_2$). The carbonate ion symmetric stretching (ν_1) and asymmetric bending (ν_4) vibrational modes are clearly visible at 1085 and 710 cm^{-1} and 1092 and 720 cm^{-1} for calcite and dolomite, respectively. The lattice modes of these carbonate minerals, which represent hindered translations and rotations of the lattice[20-22], are evident at 155 and 282 cm^{-1}, and 169 and 294 cm^{-1} for calcite and dolomite, respectively. The change in chemical environment for each of these carbonate minerals causes a shift in the vibrational wavenumber of these modes, which is quantified by the Raman spectrum.

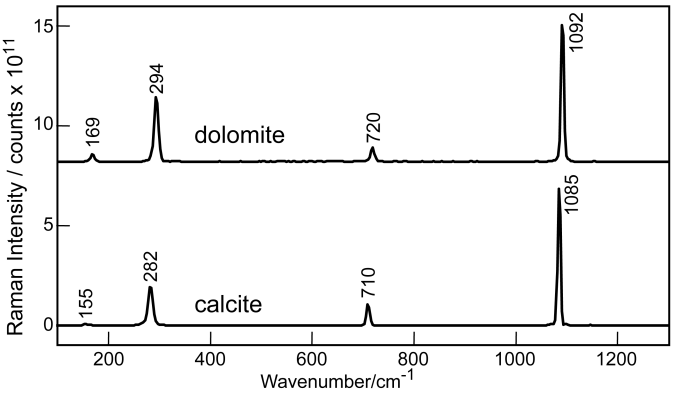

Fig 2.3 – The Raman spectra of calcite ($CaCO_3$) and dolomite ($CaMg(CO_3)_2$) in the 100-1260 cm^{-1} region. A diode-pumped frequency doubled 532 nm Nd:YAG, 100 Hz, 8.6 mJ per pulse laser was used as the excitation source. The Littrow angle was set to 2.2870° in order to retro-reflect 532 nm light. The ICCD gate width was 30 ns, the practical width of a laser pulse, in order to reject ambient light. The intensifier gain of the ICCD was set to 150. The images were accumulated for 30 seconds.

Figure 2.4 depicts the Raman spectra of gypsum ($CaSO_4 \cdot 2H_2O$) and anhydrite ($CaSO_4$). The most prominent feature of these spectra is the sulfate anion symmetric stretch (ν_1) at 1006 cm^{-1} for gypsum[23], which is shifted to a higher wavenumber, 1018 cm^{-1}, as the compound is dehydrated into anhydrite[24-25]. The symmetric bending modes (ν_2) of sulfate appear at 415 and 494 cm^{-1} in gypsum and 416 and 499 cm^{-1} in anhydrite. The other modes, between 600 and 700 cm^{-1}, are antisymmetric bending modes (ν_4) of the sulfate anions[23-25].

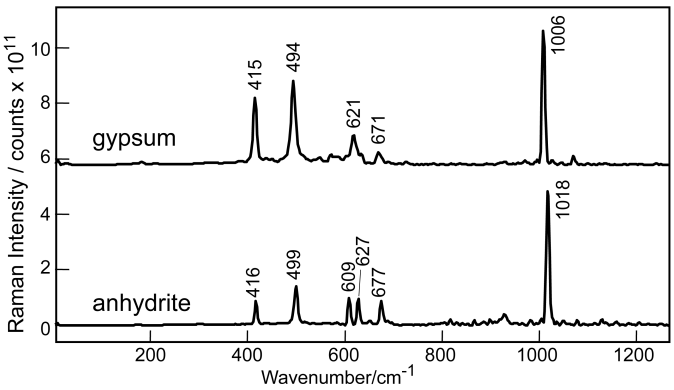

Fig 2.4 – The Raman spectra of anhydrite ($CaSO_4$) and gypsum ($CaSO_4 \cdot 2H_2O$) in the 100-1260 cm^{-1} region. The settings used for these spectra were identical to those described in **Fig. 2.3**.

Figure 2.5 shows the Raman spectra of two feldspars, namely, microcline and plagioclase and a forsterite-rich olivine (Fo_{91}). The most distinctive features of the feldspar mineral spectra are the 4-membered tetrahedral ring breathing modes located between 450 and 520 cm^{-1} in the Raman spectrum[26-27]. In the case of the ordered microcline polymorph of potassium feldspar, these modes appear at 475, 484, and 513 cm^{-1} as a triplet, and in the case of plagioclase containing Al, Si disorder[27] these breathing modes are evident as a doublet at 481 and 509 cm^{-1}. The most impressive feature of the forsterite spectrum is the completely resolved doublet at 824 and 855 cm^{-1}. This doublet originates from the $Si\text{-}O_{non\text{-}bridging}$ bond stretching in the $[SiO_4]^{4-}$ tetrahedra and has a mixed character of ν_1 and ν_3 modes[28-30]. The spectra of these three silicate minerals over a large (15 mm diameter) area demonstrate SHRS's excellent resolution and S/N ratio.

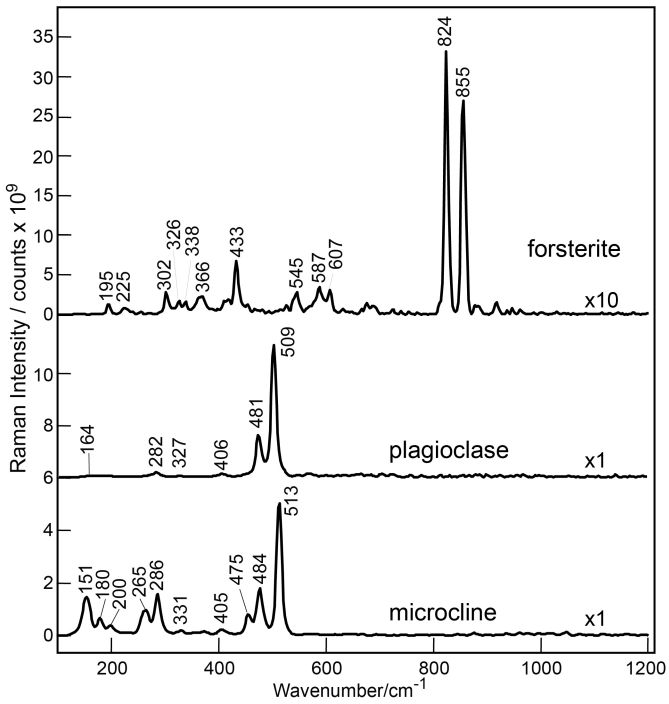

Fig 2.5 – The Raman spectra of forsteritic olivine (Fo_{91}) and feldspars, specifically microcline and plagioclase in the 100-1200 cm^{-1} region. The settings used for these spectra were identical to those described in **Fig. 2.3** except for the accumulation time, which in this case was 50 seconds for olivine and 60 seconds for microcline and plagioclase.

2.5.2 Properties of SHRS

The resolving power, R, of SHRS is proportional to the width of the two diffraction gratings, W (mm), and the groove density, d (lines per mm)[6], as indicated by Eq. 2.7.

$$R = 2Wd = 7620 \tag{2.7}$$

where W equals 25.4 mm for each grating and d equals 150 grooves per mm. Using this value for R, the minimum resolvable wavenumber difference[6], Δσ, can be calculated with use of Eq. 2.8.

$$R = \frac{\sigma}{\Delta\sigma} \tag{2.8}$$

where σ represents an absolute wavenumber of a spectral line. Therefore, SHRS should theoretically be able to resolve peaks separated by 2.47 cm^{-1} if σ is set equal to the absolute wavenumber of the laser (18794.2 cm^{-1}). The full-width half maximum (FWHM) of the narrowest line presented in this paper is the symmetric stretch (ν_1) of calcite, which occurs at an absolute wavenumber of 17709.2 cm^{-1} with a FWHM of 3.41 cm^{-1} and indicates an experimental resolving power of 5190.

Next, the bandpass[6] can be calculated with use of Eq. 2.9.

$$BP = \frac{N\sigma}{2R} \tag{2.9}$$

where N is the number of pixels of the CCD illuminated on the x-axis, R is the resolving power, and σ is the wavelength of the laser in absolute wavenumbers. Setting R equal to 7620, N equal to 1024, and σ equal to 18794.2 cm^{-1}, the bandpass was calculated to be 1262.8 cm^{-1}. This value is very close to the experimentally determined bandpass of 1260 cm^{-1}, determined by calibrating the x-axis of a SHRS calcite spectrum to a reference calcite spectrum with a quadratic curve and taking the difference of the endpoints.

Lastly, the etendue[6] was calculated with help from Eq. 2.10.

$$\Omega = \frac{2\pi}{R} \tag{2.10}$$

which yields a collection solid angle of 8.25 x 10^{-4} sr and a field-of-view of 3.24 x 10^{-2} radians. Evidently with 25 mm diameter lens and 1.5 cm diameter laser beam it is possible to measure the Raman spectra of the mineral samples at a distance of 0.5 m with compact SHRS.

2.6 Conclusion

In this work, the data reduction procedure was described, including phase and intensity corrections, and the properties of SHRS were calculated, including resolving power, bandpass, and etendue. This work demonstrated for the first time that it is possible to measure with SHRS the Raman spectra of olivine and feldspar minerals, which have a relatively low Raman scattering efficiency. This work also demonstrated SHRS' ability to measure Raman spectra of carbonate, sulfate and silicate minerals at a distance of 0.5 meters with a 532 nm pulsed Nd:YAG laser and SHRS' potential for planetary science applications.

Chapter 3: Data Reduction Optimization for Spatial Heterodyne Raman Spectroscopy with Application to Minerals, Salts and Organic Compounds

Spatial heterodyne Raman spectroscopy (SHRS) is a variant of a Michelson interferometer in which the mirrors of a Michelson are replaced with two stationary diffraction gratings. When light enters SHRS, it is reflected off the diffraction gratings at frequency dependent angles that in turn produce crossed wavefronts in space that can be imaged by a plane array detector. The crossed wavefronts, which represent a superposition of interference fringes, are converted to Raman spectra upon Fourier transformation. In this work, a new approach to intensity calibration is discussed that originates from modeling the shot noise produced by SHRS and converting the real noise to the idealized white noise predicted by theory. This procedure has two effects. First, the technique produces Raman spectra with white noise. Second, when the mean of the noise is normalized to one, the technique produces Raman spectra where the intensity axis is equal to signal-to-noise ratio.

Next, the data reduction technique described in brief above is applied to the measurement of carbonate, sulfate, silicate and phosphate minerals at distances of 0.1 and 5 meters from the collecting lens. The Raman spectra at both distances are compared and contrasted, and the possibility of using SHRS for future planetary mission is commented on. Finally, the Raman spectra of salt and organic compounds of interest to the planetary science community are measured at a distance of 5 meters with the technique described above.

3.1 Introduction

Modern planetary missions typically require spectroscopic tools capable of unambiguously identifying organics, inorganics and biomarkers. Raman spectroscopy is ideally suited to fulfill these requirements due to its selectivity to chemical environments and ease of analysis due to its narrow spectral features. Recently, Harlander[1] invented a new type of interferometer, the spatial heterodyne spectrometer (SHS), which is capable of measuring Raman spectra with high resolution in a compact, light footprint system. The spatial heterodyne Raman spectrometer (SHRS) is a Michelson interferometer variant in

which the mirrors of a Michelson are replaced by two stationary diffraction gratings. The light entering SHRS is incident upon the diffraction gratings, and the diffracted wavefronts recombine as crossed wavefronts at the beam-splitter, creating an interference pattern in space, which is imaged by and intensified charge-coupled device (ICCD) camera. The resulting interference pattern is Fourier transformed (FT), yielding a Raman spectrum.

SHS was first developed by Harlander[1] in order to bring the advantages of interferometry into the ultraviolet (UV) regime. Traditional interferometers require sub-wavelength optical flatness so that phase errors generated by optical defects do not dominate the output of the interferometer. The surface flatness requirement is relaxed for SHS from sub-wavelength flatness across the whole optics piece, to that area which is imaged by a single pixel element on the ICCD. Harlander utilized these benefits in order to measure C IV emission lines in the Cygnus loop[1], detect hydroxyl radicals in Earth's mesosphere[2,3], and measure O II emission lines from diffuse gas clouds in the Milky Way galaxy[4]. SHS has since been extended to many other applications that generally fall into two categories. First, SHS has been used to measure various forms of emission and scattering spectra from the extreme UV to the near infrared, including Raman spectra of organics, inorganic salts, pharmaceuticals and minerals[5-10], atomic emission spectra of brass alloys[11], and emissions by particles in various strata of the atmosphere[12-13]. The second class of SHS experiments involves measuring the Doppler shift of emission lines in order to estimate velocity distributions, notably wind velocity measurements from ground[14] or satellite based instruments.

One of the principle advantages of spatial heterodyne spectroscopy is its ability to correct optical, phase and intensity defects in post-processing. This concept has arisen frequently in the spatial heterodyne spectroscopy literature. Some notable examples include the correction of irregular pixel-to-pixel quantum efficiencies by flatfielding according to the balanced-arm, unbalanced-arm or phase-shifted flatfielding[15] approaches, the correction of frequency dependent or independent phase errors[16], and the correction of figure errors and index inhomogeneities[17] of the gratings and beam-splitters. Less artful attention however has been focused on the concept of intensity calibration as a function of frequency. The methods utilized thus far for intensity calibration have been rather ad-hoc or tedious, either requiring a separate intensity

calibrated Raman spectrometer to compare and correct raw SHRS spectra[18] or requiring a multitude[7] of measurements of a single spectral feature as a function of Littrow angle. In this work, a heretofore unpublished method of intensity calibrating SHRS spectra is described that relies upon returning the real-world outputs of SHRS to its theoretical idealization.

Once the data reduction procedure has been explained in detail, the technique will be applied to the measurement of minerals, salts and organics relevant to the planetary science community. The purpose of this work is to demonstrate the usefulness of SHRS in identifying these materials and to test whether or not SHRS could replace traditional dispersive based Raman instruments for planetary missions.

3.2 Samples

The rock-forming minerals used in this work were purchased from Ward's Natural Science Establishment, Inc. (Rochester, NY, USA). The carbonate minerals calcite, dolomite, rhodochrosite, siderite and smithsonite were acquired, respectively, from Chihuahua, Mexico, Bamble, Norway, Catamarca Province, Bolivia, Haints County, Nova Scotia Canada, and Cochise County, Arizona USA. The sulfate minerals anhydrite, barite, and gypsum samples were, respectively, taken from Windsor Nova Scotia Canada, Potosi, Missouri USA, and Washington County, Utah USA. The feldspar samples microcline and plagioclase were from Essex County New York and Crystal Peak Colorado, respectively. Electron microprobe analysis showed that the composition of the major phase in the microcline sample was $Ab_{5.48}An_{0.03}Or_{94.3}$, where Ab = albite ($NaAlSi_3O_8$); An = anorthite ($CaAl_2Si_2O_8$); and Or = orthoclase ($KAlSi_3O_8$). The sample originally labeled as orthoclase was largely a plagioclase with composition of $Ab_{70.09}An_{21.18}Or_{2.78}$. The other tectosilicate minerals presented in this work are quartz and sodalite, which were acquired, respectively, from Hot Springs, Arkansas USA and Cochabamba Province, Bolivia. The orthosilicate minerals forsterite, topaz and zircon were acquired from Jackson County, North Carolina USA, Millard County, Utah USA, and Minal Gerais, Brazil. The sample called forsterite was found to be a magnesium-rich olivine (Fo_{91}), (91% forsterite (Mg_2SiO_4) and 9% fayalite (Fe_2SiO_4) by electron microprobe analysis. The minerals spodumene and phosphate were acquired from Minas Gerais, Brazil and Perkins Mills, Ontario Canada, respectively. All mineral samples

were measured without cutting or polishing. The salts and organics presented in this work, including epsomite, $KClO_3$, $KClO_4$, KNO_3, Urea, NH_4NO_3, acetonitrile, naphthalene, anthracene and cyclohexane were analytical grade chemicals purchased from Fisher Scientific or Sigma Aldrich.

3.3 Experimental Method of SHRS at 0.1 and 5 meters

Two experimental designs were used in this experiment. The sole difference between the two set-ups is the collection optic and the distance of the sample. In the first experimental design, the sample is placed 100 mm from a 25.4 mm collimating lens (f = 100 mm). This experimental design is nearly identical to that described in **Fig 2.1** and so will not be elaborated further here.

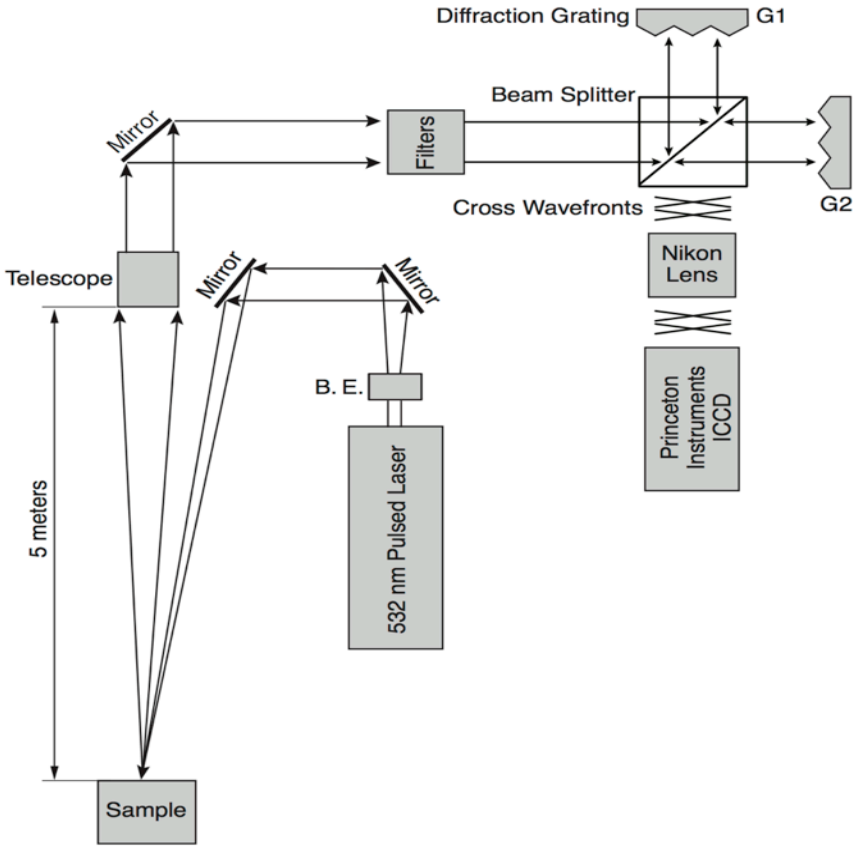

Fig 3.1 – An illustration of the SHRS system used to measure Raman spectra at a distance of 5 meters. B.E. stands for beam expander.

Figure 3.1 illustrates the second experimental design used in the present work. A Quantel Centurion compact, pulsed Nd:YAG laser operating at 532 nm, 100 Hz and 8.6 mJ per pulse is sent through a 2x beam expander, reflected off two mirrors and directed onto the sample. The sample scatters said light and a portion of the scattered light, as defined by the solid angle, is collected by a Questar 96.5 mm diameter telescope located 5 meters away from the sample. The collected light is forced through a 25.4 mm exit aperture, reflected off a mirror, attenuated by two 532 nm edge filters and allowed to pass into the interferometer. Once inside the interferometer, the light is split in two by a 50/50 silica glass cube beam splitter and directed unto two tilted diffraction gratings. The diffraction gratings, which have 150 grooves per mm and are 25 mm square, are oriented to retro-reflect a user-defined wavenumber. The angle at which a given wavenumber is reflected is determined by defining the angle of incidence and calculating the angle of reflectance in the grating equation[1], as shown in Eqn. (3.1).

$$d(\sin\theta_i + \sin\theta_r) = m\sigma \tag{3.1}$$

where σ is a wavenumber, m is the order of light, and d is the distance between adjacent grooves on a grating in units of wavenumbers. A special case arises when the angle of incidence equals the angle of reflectance. This special case is known as the Littrow angle, θ_L, and is defined[1] by Eqn. (3.2).

$$\theta_L = arcsin\left(\frac{m\sigma_0}{2d}\right) \tag{3.2}$$

The gratings retro-reflect σ_0 and produce planar parallel wavefronts from each grating that combine at the beam splitter, producing a fringe of constant intensity across the ICCD. For wavelengths not equal to σ_0, wavefronts are diffracted at angles relative to the optical axis, which recombine at the beam-splitter as crossed wavefronts (**Fig. 3.1**). When these crossed wavefronts are imaged on the ICCD, they produce a spatial fringe pattern, as described[1] by Eqn. (3.3).

$$I(x) = \int_0^\infty B(\sigma)(1 + \cos[2\pi(4(\sigma - \sigma_0)x\tan\theta_L)])d\sigma \tag{3.3}$$

where B(σ) represents the input spectral intensity as a function of wavenumber, and x represents the position on the CCD array x-axis. Equation (3.4) describes the width of a spatial fringe[1].

$$f = 4(\sigma - \sigma_L)tan(\theta_L) \tag{3.4}$$

An interesting property of SHRS is that +σ and –σ wavenumber shifts produce identical spatial fringe patterns due to the symmetry properties of cosine, as can be seen in Eqn. (3.3). Yet by introducing a small tilt along the y-axis of one grating, this symmetry property can be broken and the bandpass can be doubled, as described by Eqn. (3.5).

$$I(x,y) = \int_0^\infty B(\sigma)[1 + \cos\big(2\pi(4(\sigma - \sigma_0)x\tan\theta + \sigma y\alpha)\big)]d\sigma \qquad (3.5)$$

where α represents the grating tilt along the y-axis and σα is a spatial frequency along the y-axis of the ICCD.

The two-dimensional interference pattern is focused by a Nikon f/1.8D lens and imaged by a Princeton Instruments intensified charge-coupled device (ICCD). The principle advantage of using an ICCD is its ability to produce a retarding voltage, which inhibits photons from being recorded by the CCD while the retarding voltage is activated. This permits Raman measurements to be made during daytime ambient light conditions, as the retarding voltage is deactivated exclusively during the interval when the scattered photons are incident on the detector.

3.4 Operating Procedure & Data Reduction

Raman spectra were collected by SHRS in the following manner. First, the Littrow angle was set in the middle of the desired bandpass. The effective bandpass in this work is about 1200 wavenumbers on either side of the Littrow angle. Since SHRS is an amplitude-splitting interferometer with a sinc(σ) instrumental response, the instrument is most sensitive to spectral features near the user-defined Littrow angle and so judicious selection of the Littrow angle is necessary in order to achieve the best Raman spectrum. In the case of mineral and salt spectra, the Littrow angle was generally set between 600 and 800 cm^{-1} Raman shift relative to the laser excitation wavenumber (18794.2 cm^{-1}) in order to capture the crystal lattice modes below 400 cm^{-1} Raman shift, the symmetric and antisymmetric bending modes of the anions between 400 and 700 cm^{-1} Raman shift, and the symmetric stretching modes of the anions between 900 and 1100 cm^{-1} Raman shift. In the case of organic compounds, the Littrow angle was generally set between 1800 and 2000 cm^{-1} Raman shift relative to the laser excitation wavenumber (18794.2 cm^{-1}) in order to capture the carbon-carbon vibrations around 800 cm^{-1} Raman shift at one end of the bandpass, and

the carbon-hydrogen vibrations at the other end of the bandpass around 3000 cm^{-1} Raman shift. Detailed accounts of the Littrow angle selections will be provided in the figure captions of every Raman spectrum in this chapter.

Three images were obtained for every sample. As an aside, the author's in-house idiosyncratic identifiers will label certain pieces of data for the purposes of easing communication. First, an image was taken of the interference pattern produced by the superposition of the Raman spectral features. This image will be labeled the "science image". Next, each grating is blocked one at a time with a piece of black paper, and an image is acquired with setting identical to the "science image". These two images will be labeled the "non-modulated images". The purpose of acquiring the non-modulated images is to remove the non-modulated contributions to the science image and produce Raman spectra with the greatest signal-to-noise.

Next, the three images are loaded into a python integrated development environment called Spyder as numpy arrays and the "non-modulated images" are subtracted from the "science image" to produce the "modulated image". Next, the "modulated image" is apodized by a two-dimensional Gaussian function, so that the edges of this new image, labeled the "apodized image", approach zero in order to eliminate ringing by reducing the magnitude of the sidelobes in the instrumental lineshape. Next, a two-dimensional Fourier transform (2D-FT) is taken of the apodized image, and the phase of the 2D-FT is corrected by the method devised by Mertz[19] and Brault[20]. Let this new image be called the "phase corrected FT".

The "phase corrected FT" is depicted as the top image in **Fig 3.2**. In this image, three major components can be identified. The first component is the direct current (D.C.) bias, located at the center of the image, which represents the first term in the Fourier series and the mean of the "apodized image". The second component is that area highlighted by the red window labeled "A". In this section of **Fig 3.2**, the area that contributes to the Raman spectrum of cyclohexane can be identified. When the area bounded by window "A" is integrated along the x-axis, a one-dimensional Raman spectrum will result, which is illustrated in sub-figure A in the lower left of **Fig 3.2**. The third component of the phase corrected FT is the noise, circumscribed by the red window "B", that corresponds to the shot noise of various frequencies recorded by SHRS. Upon integration along the x-axis, the

frequency response of the shot noise produces a sinc(σ)-like profile, as illustrated in sub-figure B by the noisy blue line. Clearly this does not represent white noise as the power is not equal in all frequencies. In order to convert the noise present to white noise, a pseudovoigt curve is fit to the blue line in sub-figure B and the fitted line is used to intensity calibrate the Raman spectrum presented sub-figure A. The result is a Raman spectrum with white noise, as presented in sub-figure C. The use and efficacy of this technique will be justified in the following section.

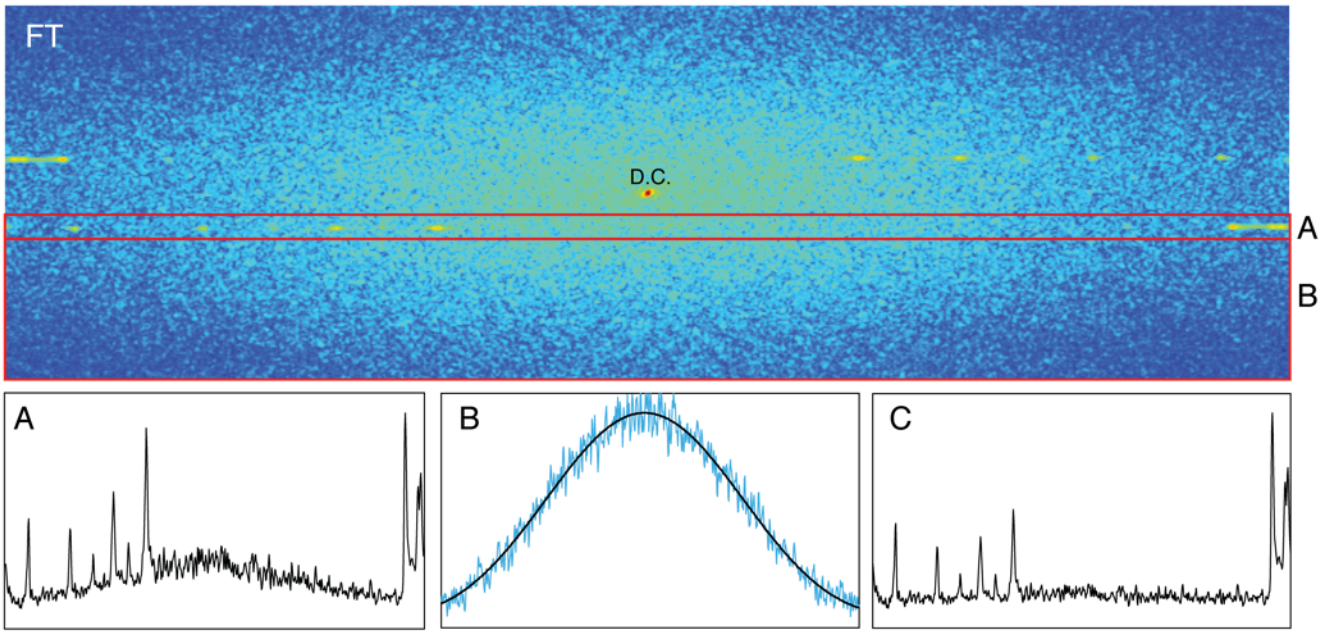

Fig 3.2 – An illustration of how data is reduced from "phase corrected FT" (top image) to the white noise Raman spectrum (labeled C) by dividing the raw one-dimensional Fourier Transform (labeled A) by the lineshape of the shot noise (labeled B).

3.5 Justification & Efficacy of Data Reduction Procedure

When a rectangular pulse is Fourier transformed, the result is a frequency response curve with a sinc(σ) profile[21]. The width of the rectangular pulse for the interference fringes is determined by the Nyquist limit, which states that the highest frequency that SHRS can record is equal to half the number of sampling elements where a sampling element in SHRS is equal to a charge-coupled device pixel along the x-axis. In the images acquired in this work, 880 pixels along the x-axis were utilized to record the interference pattern. Therefore, according to Nyquist, SHRS should measure 440 Fourier frequency bins.

This number was doubled to 880 Fourier frequency bins by introducing a small tilt along the y-axis of one grating so that frequencies greater and lesser than the frequency retro-reflected by the gratings are rotated clockwise and counter-clockwise, respectively. If no y-axis tilt were introduced, then the Raman spectral features shown in **Fig 3.2** would shift to be in-line with the D.C. bias at y = 0 and so only 440 Fourier bins would contain unique information. Therefore, SHRS measures 880 frequencies as a rectangular pulse and that, upon Fourier transformation, the frequency response constitutes a sinc(σ) lineshape.

Noise in SHRS undergoes a similar transformation. Since every pixel on the ICCD in an SHRS experiment contains information about every spectral frequency, the noise produced by shot noise in any pixel contributes noise to all frequencies. Therefore, the noise should have constant power spectral density in all frequencies, otherwise known as white noise. The extent to which the noise is not white is an indication of the frequency response profile of SHRS. Hence by modeling the noise, SHRS' frequency response profile can be quantified and hence can be used to intensity calibrate Raman spectra. This goal is achieved by fitting a pseudovoigt function to the shot noise as circumscribed by window "B" of **Fig 3.2**, followed by dividing the shot noise by the fitted curve. The effect of dividing the shot noise by the fitted curve can be seen in **Fig 3.3**.

Next, the successfulness of this correction technique in producing white noise will be proven by the following two methods. First, the Fourier transform of white noise should be an impulse at the origin. This makes sense since white noise should have no periodicity and the intensity at the origin of a Fourier transform simply quantifies the mean of the item being Fourier transformed. Second, the autocorrelation of white noise should be a triangle that peaks at the origin and that extends from $-\tau$ to τ where τ represents the length of the rectangular pulse. In **Fig 3.3**, the Fourier transform and autocorrelation of three types of noise is calculated, including the shot noise in window "B" before and after correction, and the shot noise in window "A" after correction. It is clear that the correction being applied is effective because the Fourier transform is an impulse at the origin and the autocorrelation is a triangle in both corrected noise spectra.

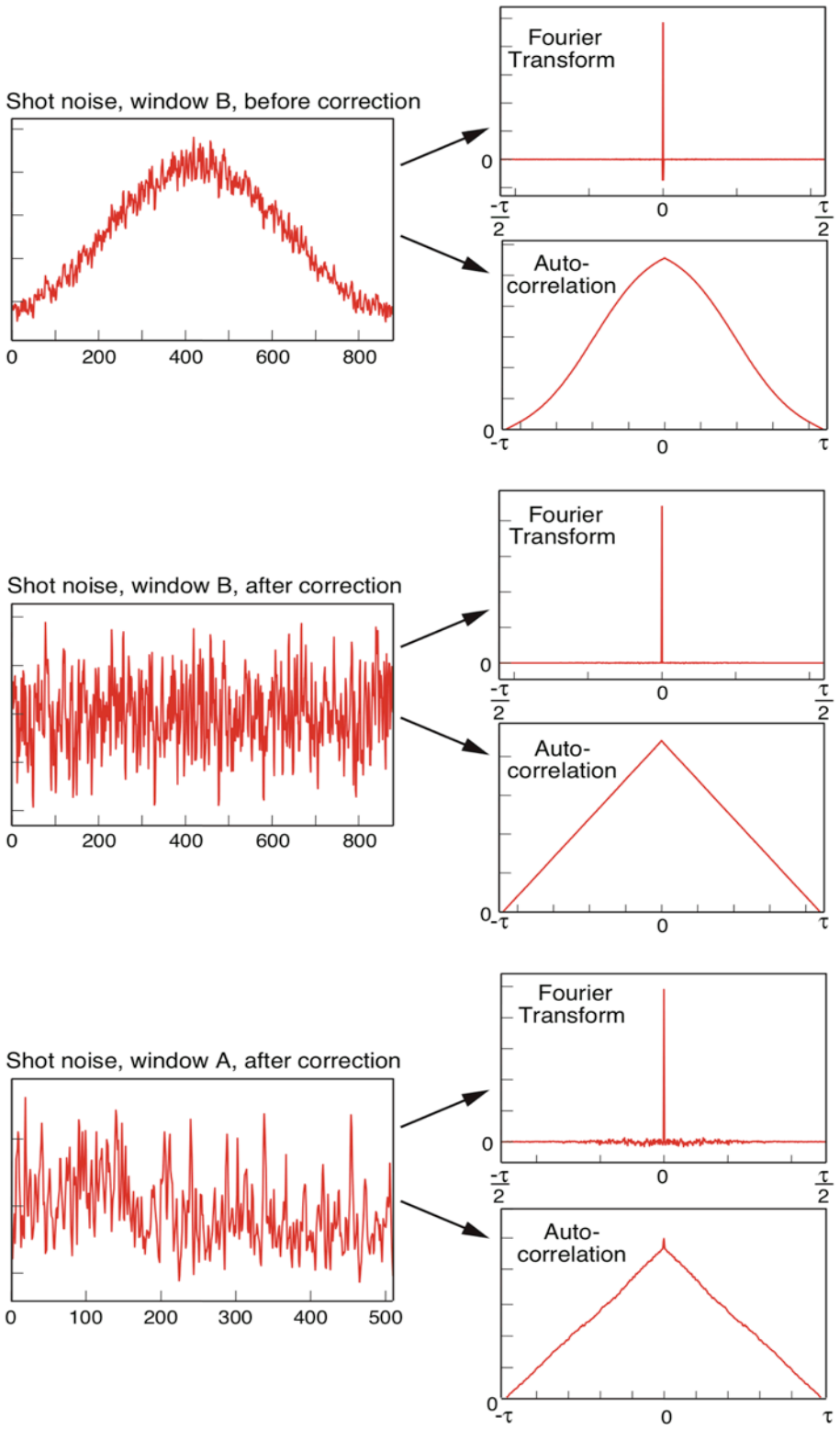

Fig 3.3 – A depiction of the data reduction process in which raw shot noise is converted to white noise via modeling with a pseudovoigt curve. The noise is white noise if the Fourier transform is an impulse at x = 0 and the autocorrelation is a triangle.

3.6 Results and Discussion

The following section will illustrate the Raman spectra acquired by SHRS with the instrument designs and data reduction procedure detailed above. The purpose of this work is to explore the potential of using SHRS for planetary surface exploration and so the majority of the Raman spectra presented in this section will be of minerals. A limited number of salt and organic spectra will be presented as well that either have relevance to the planetary science community or are commonly used as standards in calibrating Raman spectrometers, such as in the case of cyclohexane and acetonitrile. The results and discussion section is further subdivided into the following six parts. In **Section 3.6.1**, the Raman spectra of minerals measured at a distance of 10 cm from a 2.54 cm (f = 10 cm) collection lens will be presented with the intent of showing SHRS' ability to measure the weak bands of low Raman scattering efficiency minerals. In **Section 3.6.2**, the Raman spectra of minerals measured at a distance of 5 meters will be presented. In **Section 3.6.3**, the results of **Sections 3.6.1** and **3.6.2** will be compared and contrasted. In **Sections 3.6.4** and **3.6.5**, the ability of SHRS to measure the Raman spectra of salt and organic compounds, respectively, will be demonstrated. Finally, in **Section 3.6.6**, the signal-to-noise Raman spectrum of cyclohexane will be presented.

3.6.1 The Raman Spectra of Minerals at 0.1 meters

The carbonate minerals are one of the most common minerals found on the Earth, comprising about 4% of the Earth's crust[22] by mass. The carbonate mineral calcite is the most common of the carbonate minerals and is commonly found in metamorphic marble[23], the shells of marine organisms[24], and in caves in the form of stalactites and stalagmites[25]. Furthermore, carbonate minerals are naturally produced in hydrothermal veins[26] on planet Earth and have been identified on Mars by landers[27], rovers[28] and orbital remote-sensing techniques[29-30], although the origin of the carbonates on Mars is not yet well understood.

The characteristic vibrational modes of carbonate minerals[31-33], quantified by their Raman spectra, include the symmetric stretch of the carbonate anion (ν_1) that appears between 1085-1099 cm^{-1}, the antisymmetric bending mode of the carbonate anion (ν_4) that appears between 711-730 cm^{-1}, and the hindered translations and rotations of the crystal

lattice that appear between 155-302 cm^{-1}. The Raman spectra of several carbonate minerals, including smithsonite ($ZnCO_3$), calcite ($CaCO_3$), rhodochrosite ($MnCO_3$), siderite ($FeCO_3$) and dolomite ($CaMg(CO_3)_2$) are presented in **Fig 3.4**.

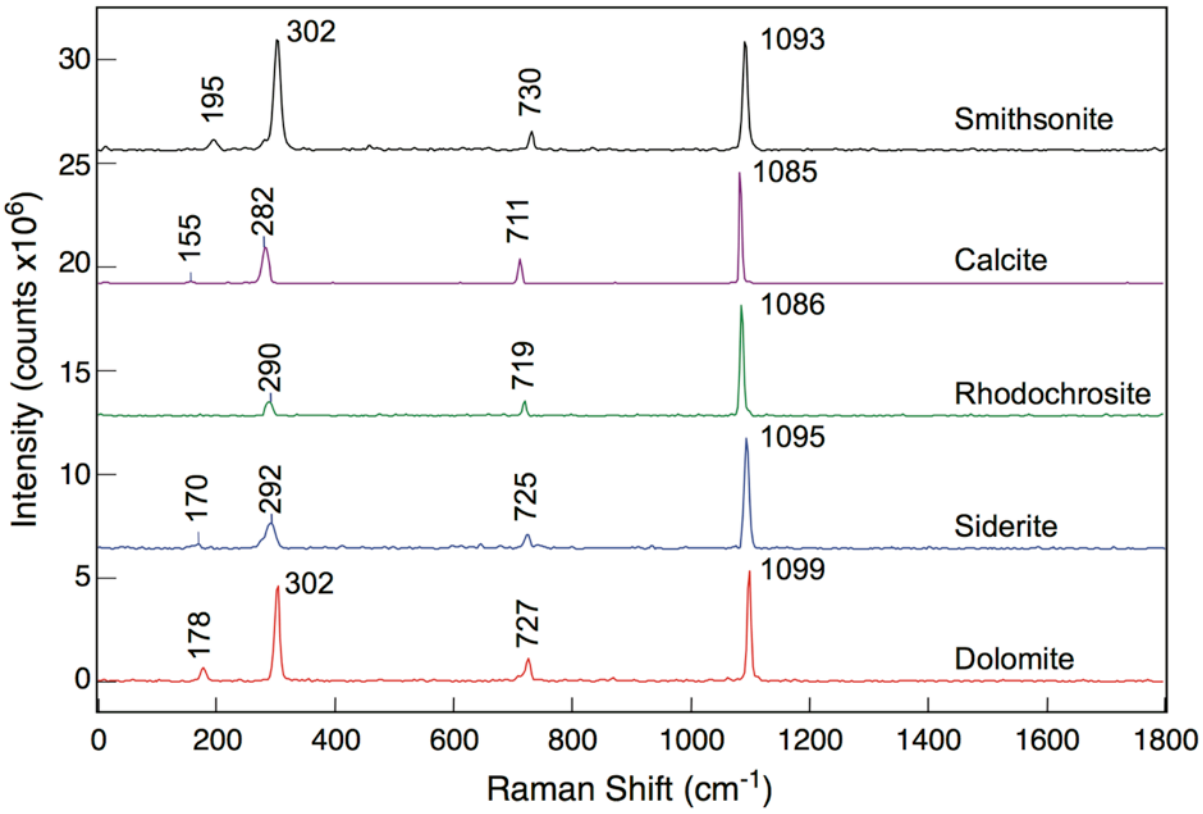

Fig 3.4 – The Raman spectra of carbonate minerals measured at a distance of 0.1 m with a laser power of 8.6 mJ per pulse and a camera gain of 150. The Littrow angle was set to retro-reflect 550 nm light. The accumulation time was 1 seconds.

Sulfate minerals are rarer than carbonate minerals in the composition of the Earth's crust. One of the mechanisms in which sulfate minerals formed on Earth is by phase transition[34] from salty waters to minerals. For example during the Paleozoic Era (600 to 230 MYA), ocean water encroached upon and contaminated the Michigan Basin. When the ocean waters receded and the volume of water in the Michigan Basin declined by evaporation, the waters of the Basin became supersaturated thus requiring the precipitation of minerals like gypsum[35]. The most commonly occurring sulfate minerals are gypsum, anhydrite and barite. Gypsum is a well-regarded building material with a

variety of uses, including as a drywall[36], as a primary ingredient in blackboard chalk[37] and as a sulfate fertilizer[38]. Gypsum is found, in addition to the Michigan Basin, in the White Sands National Monument in New Mexico USA and on Mars by rover[39-42] and orbital remote-sensing[43-44] instruments.

The Raman spectra of sulfate minerals[45-47] can be easily understood by identifying the symmetric stretch of the sulfate anion (ν_1) located between 985-1015 cm^{-1}, the symmetric bending modes (ν_2) of the sulfate anion that appear between 400-500 cm^{-1}, and the antisymmetric bending modes (ν_4) that appear between 600-700 cm^{-1}. The Raman spectra of gypsum, anhydrite and barite are presented in **Fig 3.5**.

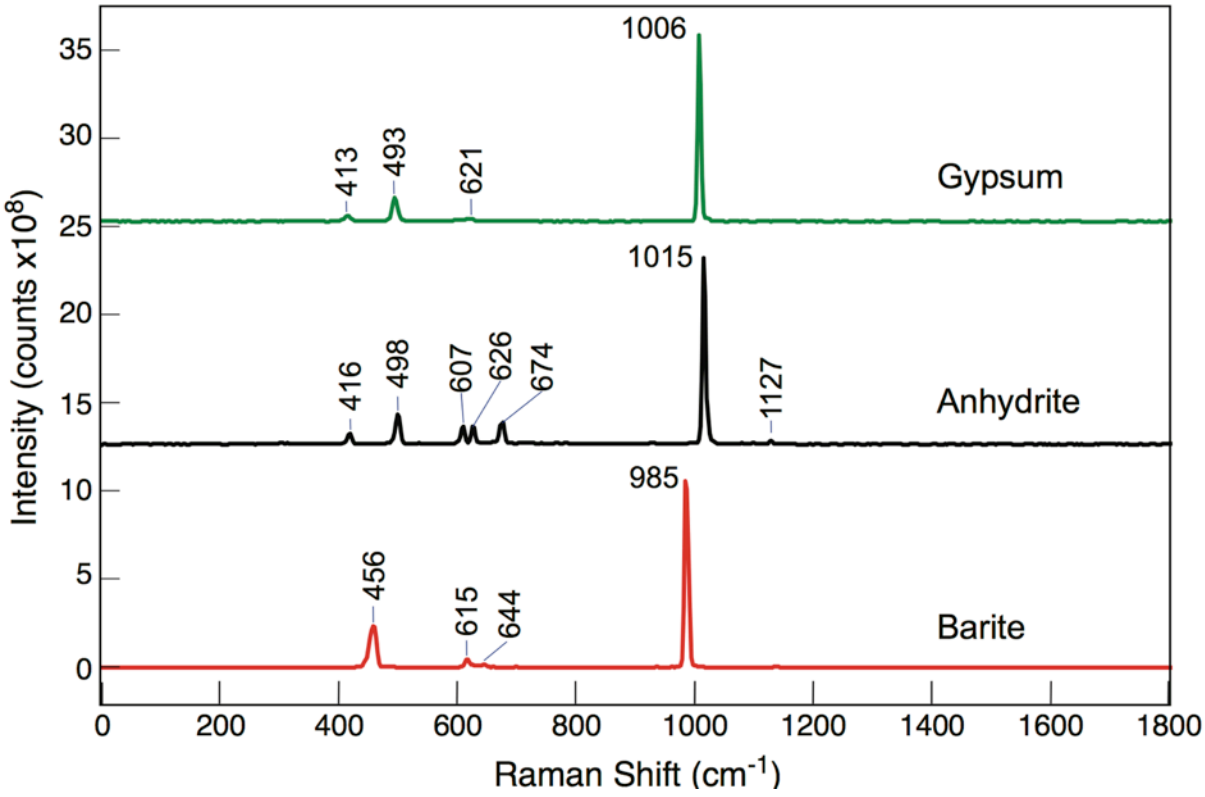

Fig 3.5 – The Raman spectra of sulfate minerals measured at a distance of 0.1 m with a laser power of 8.6 mJ per pulse and a camera gain of 150. The Littrow angle was set to retro-reflect 550 nm light. The accumulation time was 1 seconds.

Silicate minerals make up more than 90% of the Earth's crust and mantle[22]. The silicate minerals fall into a variety of sub-classifications of which three of the most important will be presented in this work. They are the orthosilicates, tectosilicates and

pyroxenes. The orthosilicates are the simplest of the silicates described in this work, made up of SiO_4^{4-} tetrahedral building blocks that are surrounded by interstitial cations that balance out the charge of the silicate anion. The most commonly occurring mineral in the mantle above 400 km are the forsterite-rich olivines[22], an orthosilicate, and is commonly formed as the byproduct of magma processes. Zircons, another orthosilicate, are most famous for their radiometric dating capabilities, determined by quantifying the defects in the crystal structure of zircon as caused by the radioactive decay of Uranium isotopes[48].

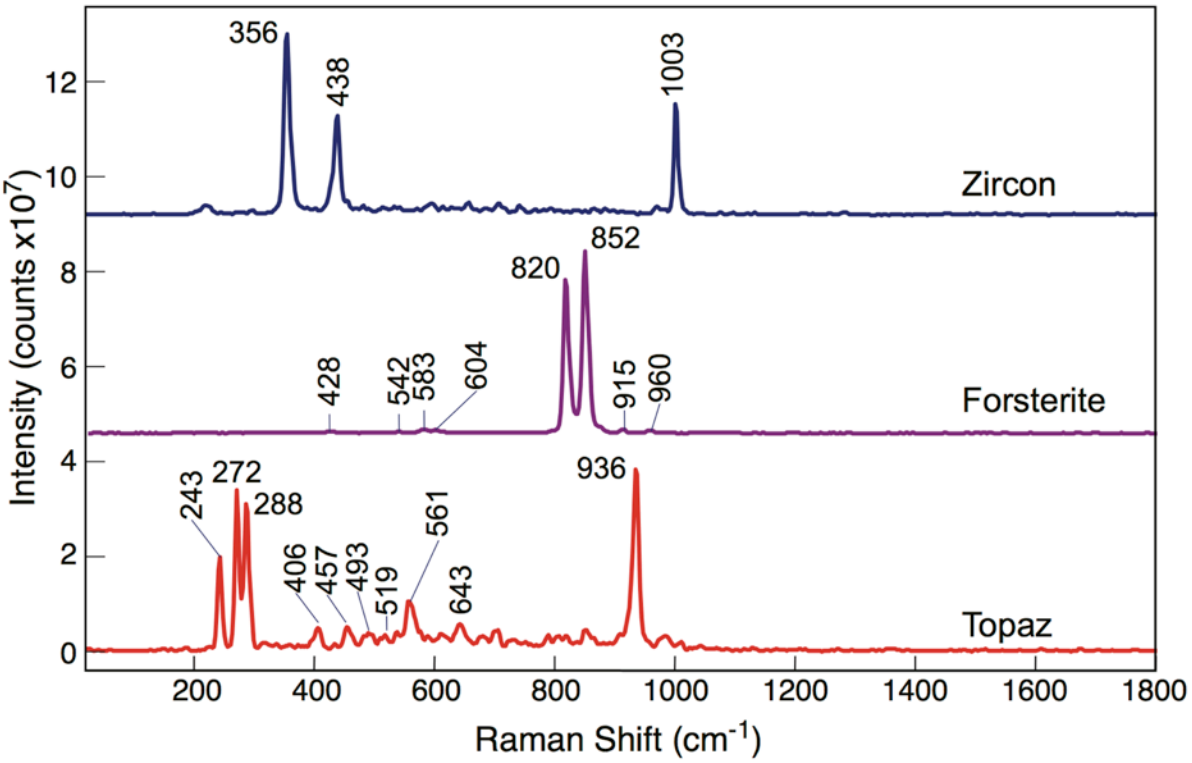

Fig 3.6 - The Raman spectra of orthosilicate minerals measured at a distance of 0.1 m with a laser power of 8.6 mJ per pulse and a camera gain of 150. The Littrow angle was set to retro-reflect 550 nm light. The accumulation time was 10 seconds.

The Raman spectra of three orthosilicate minerals, zircon ($ZrSiO_4$), topaz ($Al_2SiO_4(F,OH)_2$) and forsterite (Mg_2SiO_4), are presented in **Fig 3.6**. The principle vibrational modes of the zircon spectrum[49] labeled in **Fig 3.6** are the stretching modes of the silicate tetrahedra as shown at 356, 439 and 1002 cm^{-1} corresponding to E_g (ν_4), A_{1g} (ν_2) and B_{1g} (ν_3), respectively. The characteristic mode of forsterite[50-52] is the well-

resolved doublet that appears at 820 and 852 cm^{-1} that originates from Si-$O_{non\text{-}bridging}$ bond stretches in the SiO_4^{4-} tetrahedra and is considered to a have a mixed ν_1 and ν_3 character. Finally, the key vibrational modes of topaz[53-54] are the modes that occur at 243, 272, 288 and 936 cm^{-1}, all of which have A_g symmetry.

The tectosilicate mineral class is built upon interlinking silicon (SiO_4^{4-}) and aluminium (AlO_4^{5-}) tetrahedra. In the tectosilicate group, every oxygen of the tetrahedra is bonded to a neighboring tetrahedra and so the ratio of silicon to oxygen is one to two. The tectosilicates differ from the orthosilicates due to the fact that an isolated aluminium tetrahedra has a minus five charge and so different cations in different arrangements are required to balance out the charges. The tectosilicate minerals are the most abundant constituents of the Earth, making up as much as 60% of the Earth's crust[22] with the feldspar group being the most abundant of the tectosilicates followed by the quartz group.

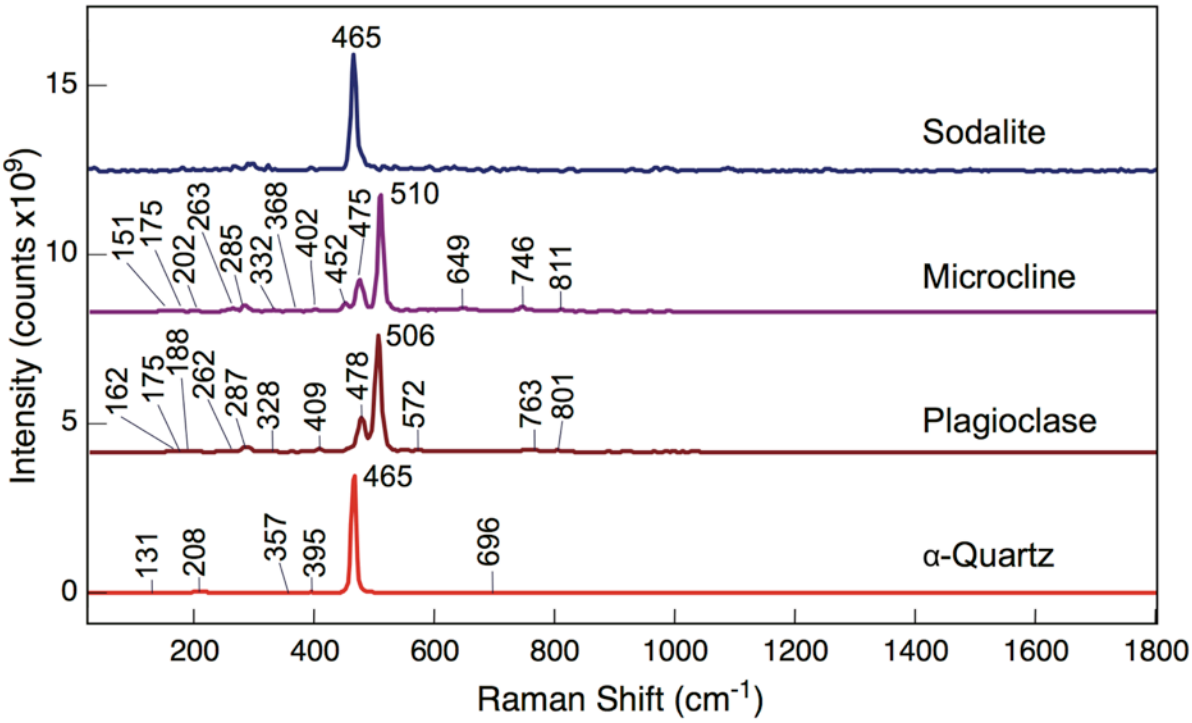

Fig 3.7 – The Raman spectra of tectosilicate minerals measured at a distance of 0.1 m with a laser power of 8.6 mJ per pulse and a camera gain of 150. The Littrow angle was set to retro-reflect 550 nm light. The accumulation time was 10 seconds.

In **Fig 3.7**, the Raman spectra of four tectosilicate minerals, sodalite, microcline, plagioclase and α-quartz are presented. The principle modes of these minerals occur

between 450-510 cm^{-1} and they correspond to the six or four-membered tetrahedral ring breathing modes. In the case of sodalite[55] and α-quartz[56], a six-membered ring breathing mode occurs as a singlet at 465 cm^{-1}, and in the case of the feldspar minerals[57-58] microcline and plagioclase, a four-membered ring breathing mode appear as a triplet at 452, 475 and 510 cm^{-1} and as a doublet at 478 and 506 cm^{-1}, respectively.

In **Fig 3.8**, the Raman spectra of α-spodumene (α-$LiAlSi_2O_6$), a pyroxene, and fluorapatite ($Ca_5(PO_4)_3F$), a phosphate mineral, are illustrated together for the purpose of economizing page space. Spodumene is a single chain pyroxene with a silicon to oxygen ratio of one to three. Both Li and Al act as network modifier cations in the crystal lattice. Spodumene is of tremendous economic importance as it is one of the few sources of lithium for the production of batteries in the world. The main vibrational modes of α-spodumene[59-60] that occur at 299, 356, 393, and 443 cm^{-1} originate from interactions between the cation-oxygen interactions. The bending vibrations of O-Si-O produce the Raman spectral features at 522 and 585 cm^{-1} and the stretching motions of $Si\text{-}O_{bridging}$ produces the strongest mode that appears at 707 cm^{-1} corresponding to the symmetric stretching mode of bridging oxygen in the pyroxene chain. Fluorapatite is the most common form of apatite. It can be found in tooth enamel and is an important precursor to the industrial production of hydrofluoric and phosphoric acid. The vibrational modes of fluorapatite can be classified[61] in the following manner. The vibrational mode at 966 cm^{-1} corresponds to the symmetric stretching (ν_1) of the phosphate anion, the vibrational modes at 591 and 610 cm^{-1} correspond to the antisymmetric bending modes (ν_4) of the phosphate anion, and the vibrational mode at 437 cm^{-1} corresponds to the symmetric bending mode (ν_2) of the phosphate anion.

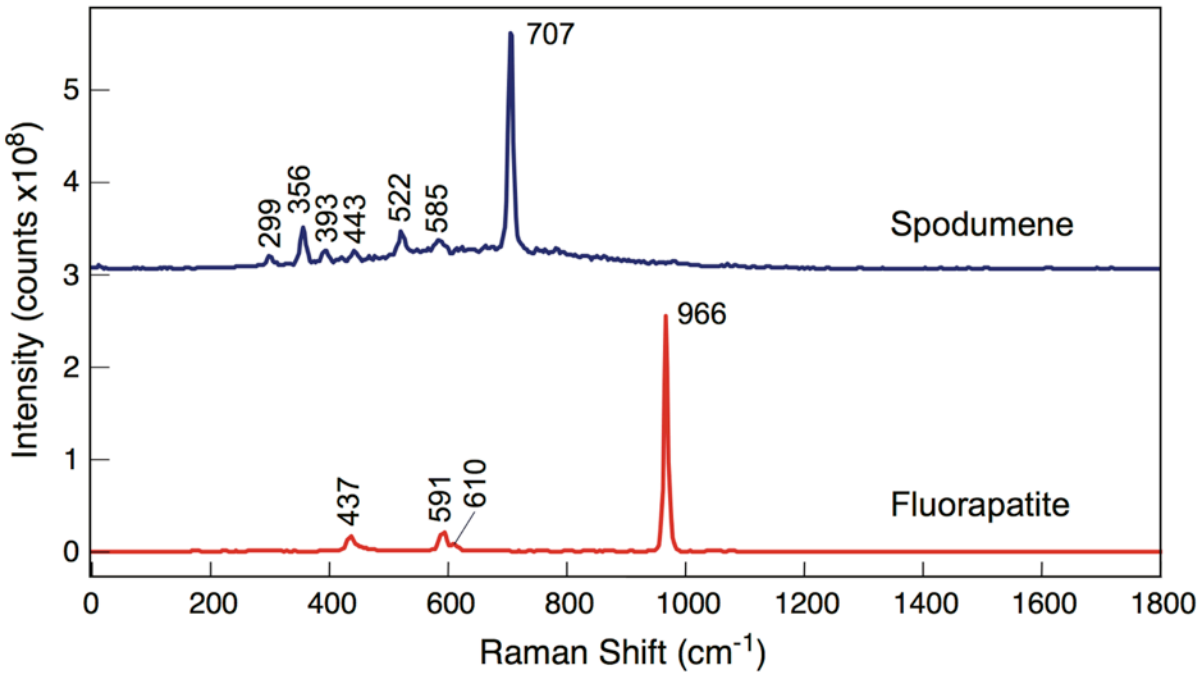

Fig 3.8 - The Raman spectra of α-spodumene and fluorapatite minerals measured at a distance of 0.1 m with a laser power of 8.6 mJ per pulse and a camera gain of 150. The Littrow angle was set to retro-reflect 550 nm light. The accumulation time was 10 seconds.

3.6.2 The Raman Spectra of Minerals at 5 meters

The Raman spectra of several minerals were measured at a distance of 5 meters from the collecting lens in order to demonstrate the efficacy of SHRS as a planetary science tool. Most of the minerals presented in this section have already been discussed in **Section 3.6.1** of the results and discussion section and so the spectra will be presented with minimal commentary.

The Raman spectra of three carbonate minerals were measured at 5 meters, including calcite, dolomite and smithsonite. The results are presented in **Fig 3.9**. The acquisition of the Raman spectrum of siderite was attempted, but no peak save the symmetric stretch of the sulfate anion (ν_1) could be attained in a reasonable period of time and hence is not included. The acquisition of the Raman spectrum of rhodochrosite was not attempted.

The Raman spectra of sulfate minerals gypsum, anhydrite, barite and epsomite were measured at a distance of 5 meters and are presented in **Fig 3.10**.

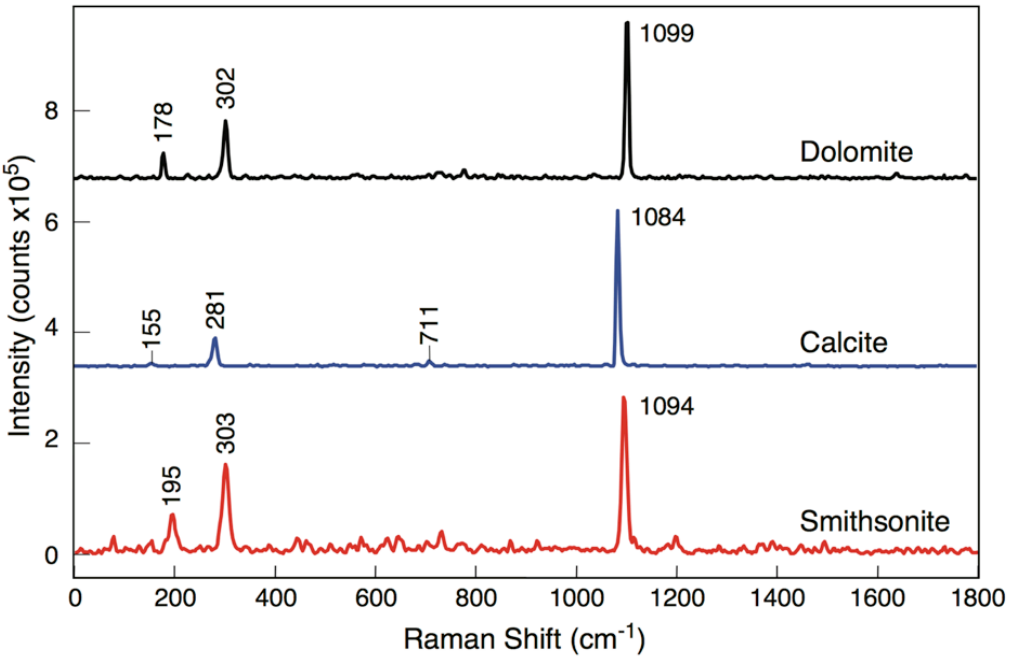

Fig 3.9 – The Raman spectra of carbonate minerals measured at a distance of 5 m with a laser power of 8.6 mJ per pulse and a camera gain of 150. The Littrow angle was set to retro-reflect 554 nm light. The accumulation time was 10 seconds.

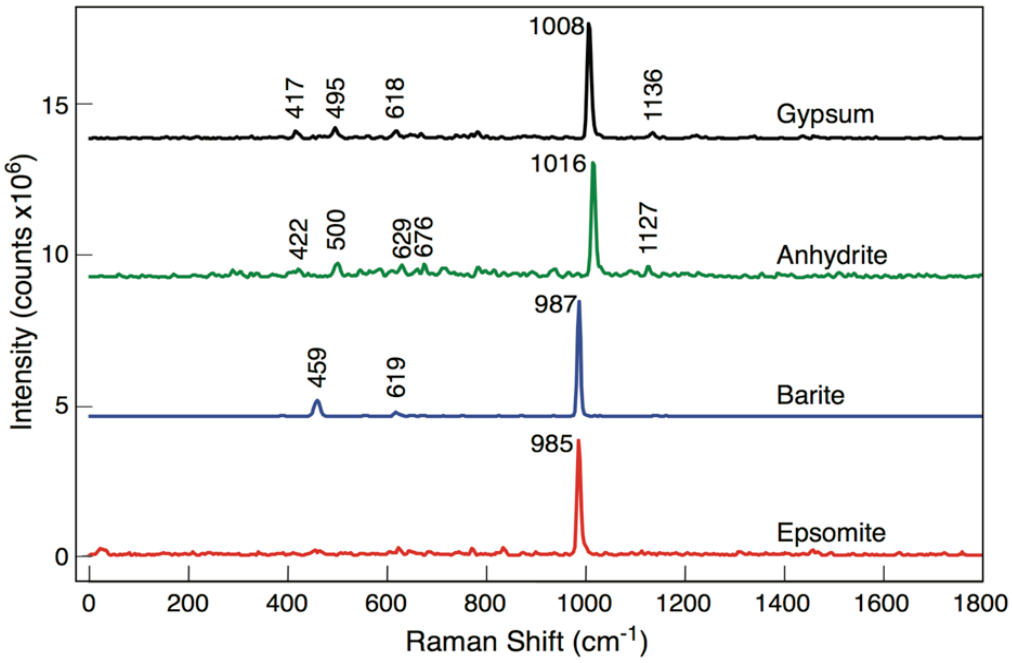

Fig 3.10 – The Raman spectra of sulfate minerals measured at a distance of 5 m with a laser power of 8.6 mJ per pulse and a camera gain of 150. The Littrow angle was set to retro-reflect 554 nm light. The accumulation time was 10 seconds.

The Raman spectra of silicate minerals plagioclase, forsterite and α-quartz were measured at a distance of 5 meters with an accumulation time of 30 seconds, as presented in **Fig 3.11**, and with an accumulation time of 60 seconds (with the exception of α-quartz), as presented in **Fig 3.12**. The silicate minerals zircon, topaz, sodalite and microcline could not be measured at 5 meters.

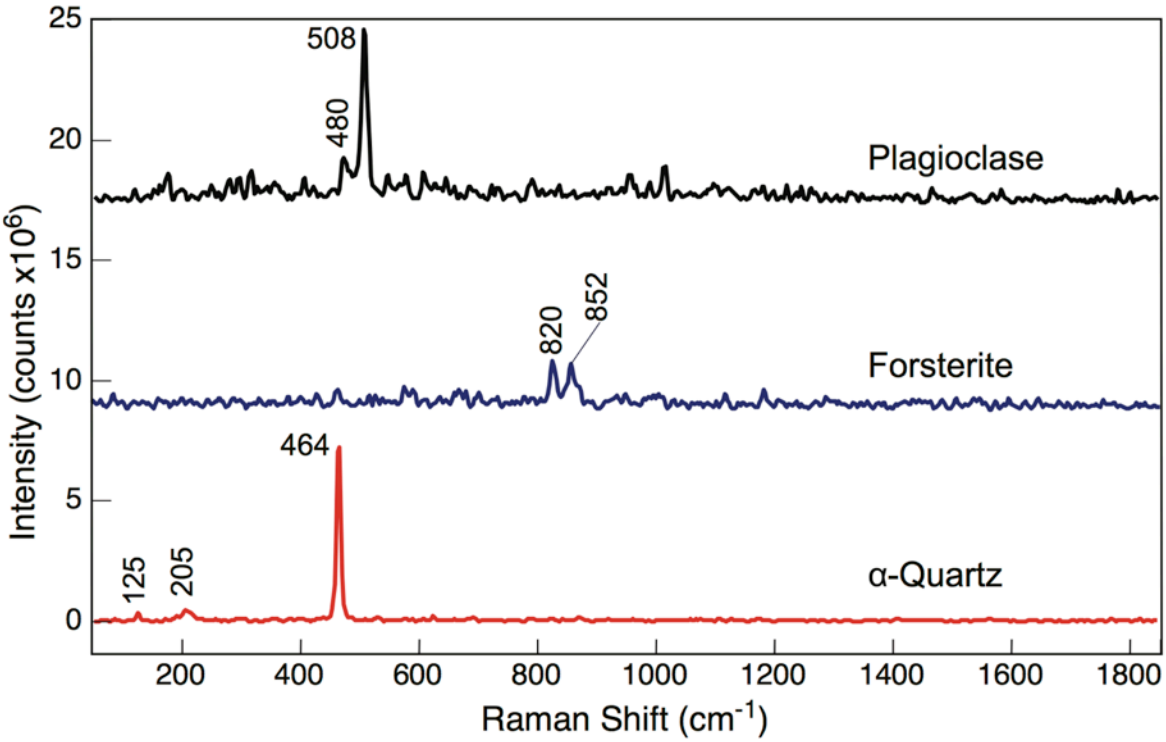

Fig 3.11 - The Raman spectra of silicate minerals measured at a distance of 5 m with a laser power of 8.6 mJ per pulse and a camera gain of 150 (250 for forsterite). The Littrow angle was set to retro-reflect 554 nm light. The accumulation time was 30 seconds.

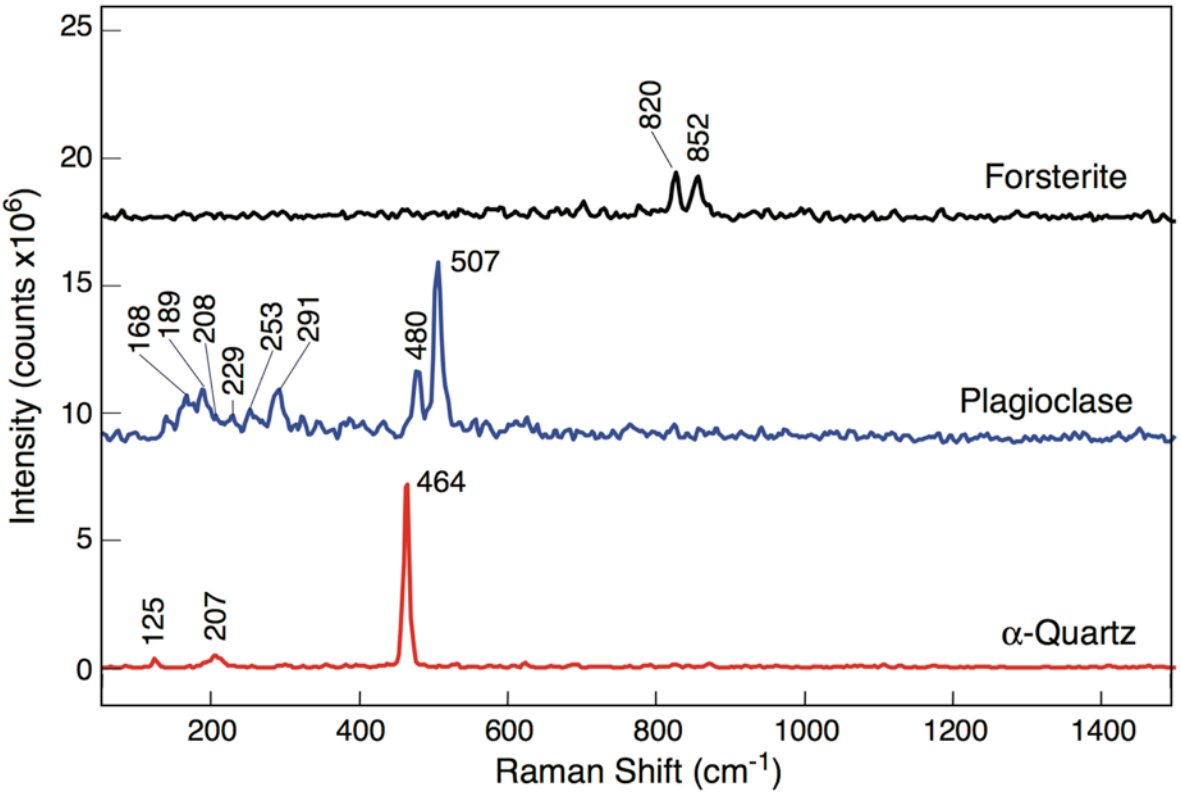

Fig 3.12 – The Raman spectra of silicate minerals measured at a distance of 5 m with a laser power of 8.6 mJ per pulse and a camera gain of 250 (150 for α-quartz). The Littrow angle was set to retro-reflect 554 nm light. The accumulation time was 60 seconds (30 seconds for α-quartz).

3.6.3 Comparison of Raman Spectra of Minerals at 0.1 and 5 meters

The intensity of a given Raman spectral feature as recorded by SHRS depends upon the amount of scattered light SHRS collects or otherwise known as SHRS' solid angle. The solid angle can be calculated according to Eqn. (3.6).

$$\Omega = \frac{A}{r^2} \tag{3.6}$$

where Ω equals the solid angle, A is the usable area of the collecting lens, and r is the radial distance from the sample to the collecting lens. In the case of the system used in section 3.7.1, the collecting lens was 0.0254 m in diameter and was located 0.1 meters from the sample. Therefore, the solid angle of the 0.1 m system has a solid angle of 5.067 x 10^{-2} sr. In the case of the system used in **Section 3.6.2**, the collecting telescopic mirror was 96.5 mm in diameter with a 25.4 mm central obstruction and was located 5 m from the sample. The

effective area of the collecting mirror was 6.807 x 10^{-3} m^2 and the solid angle is therefore 2.723 x 10^{-4} sr.

By taking the ratio of these two solid angles, the relative intensities can be predicted between two identical Raman bands measured at different distances. Based on the calculations presented above, the intensity of Raman bands measured at 0.1 meters should be 186 times more intense than those measured at 5 meters. For the sake of comparison, the same sample of dolomite was measured with identical laser power and camera gain at a distance of 0.1 and 5 meters. The ratio of 0.1 m to 5 m for the dolomite Raman bands at 178, 302 and 1099 cm^{-1} were 13:1, 29:1 and 23:1. This is not what one would expect based solely on theory of solid angles. The most likely explanation for the discrepancy is that the 5 m system has superior collimation as compared to the 0.1 m system. The angle at which a given photon reflects of the grating depends on the angle of incidence. When off-axis light is present for a given Raman band, the light reflecting off the diffraction gratings contains a range of reflection angles. This in turn causes the fringe contrast to be diminished as the phase of each reflection angle becomes out-of-sync across the ICCD. The problem of off-axis light is less prevalent in the 5 m system because the light that reaches the telescope is already nearly collimated by the time the light reaches the telescope by virtue of the small angles photons must travel from the sample to reach the telescope.

3.6.4 The Raman Spectra of Salts at 5 meters

Salts such as chlorides and perchlorates have been measured on the surface of Mars by the Curiosity Rover[62-63] and by two instruments on-board the Viking Lander[64-65] – the Wet Chemistry Lab, and the Thermal and Evolved Gas Analyzer. In addition, perchlorates and nitrates have been identified in considerable quantities within Martian Meteorites[66] recovered in Antarctica. Several authors have inferred the presence of chlorate anions, but unambiguous detection of chlorates on Mars has eluded researchers due to a lack of either sensitivity[65] or selectivity[62-63] of the on-board instrumentation. Raman spectrometers suffer no such limitations and can easily identify and differentiate between chlorate and perchlorate, as demonstrated in **Fig 3.13**.

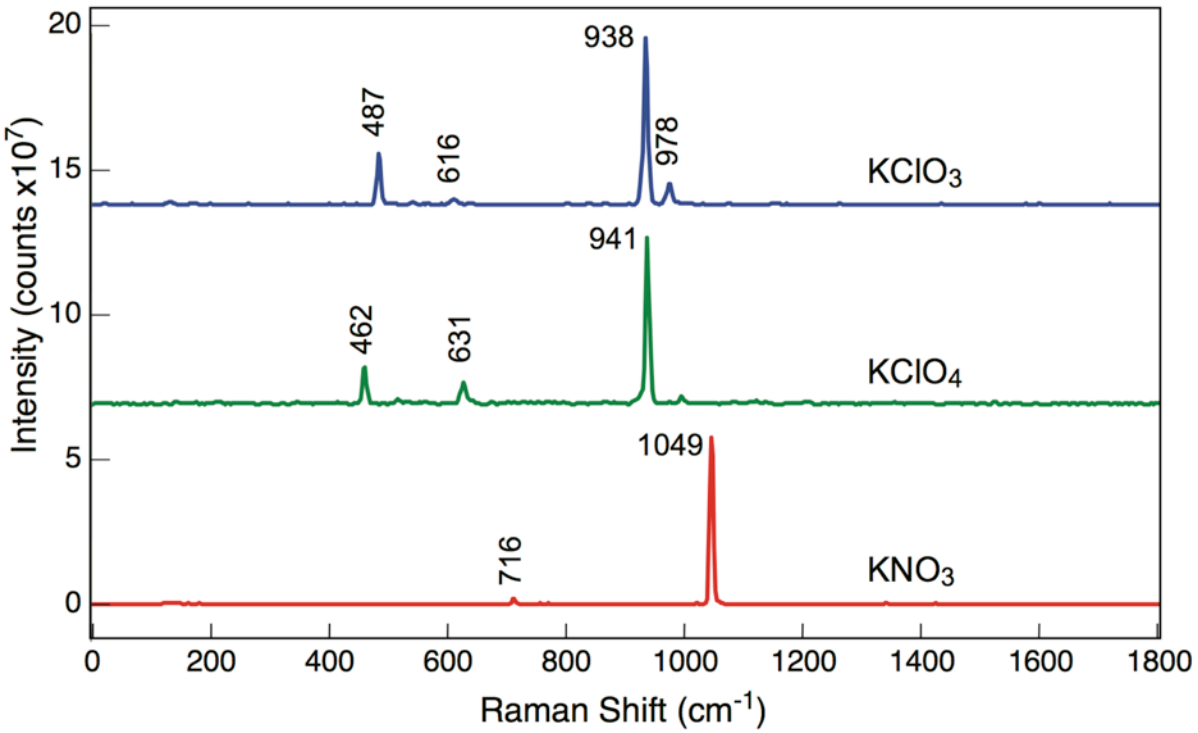

Fig 3.13 – The Raman spectra of salts measured at a distance of 5 m with a laser power of 8.6 mJ per pulse and a camera gain of 150. The Littrow angle was set to retro-reflect 554 nm light. The accumulation time was 10 seconds.

The Raman spectra of potassium chlorate[67] ($KClO_3$), potassium perchlorate[68-69] ($KClO_4$), and potassium nitrate[70] (KNO_3) are presented in **Fig 3.13**. The key features of the Raman spectra presented in this figure are the symmetric stretches (ν_1) of the anion that appear at 938, 941 and 1049 cm^{-1} for chlorate, perchlorate and nitrate, respectively. Other key features include the symmetric bending (ν_2) of the anion that appear at 487 and 462 cm^{-1} for chlorate and perchlorate, respectively, and the antisymmetric bend (ν_4) that appears at 616, 631, and 716 cm^{-1} for chlorate, perchlorate and nitrate, respectively.

Fig 3.14 contains the Raman spectra of urea ($CO(NH_2)_2$) and ammonium nitrate (NH_4NO_3). Urea has two identifiable low frequency modes[71] present at 133 and 178 cm^{-1} that are assigned E_3 and E_4 symmetry, respectively. The mode at 1010 cm^{-1} can be attributed to a symmetric carbon-nitrogen stretch. The Raman spectrum of phase IV ammonium nitrate[72-74] presented in **Fig 3.14** contains four normal modes of vibration, including a strong mode at 1043 cm^{-1} that corresponds to the symmetric stretch (ν_1) of the nitrate anion, an antisymmetric bending mode (ν_4) of nitrate at 714 cm^{-1}, and two lattice

vibrations at 141 and 170 cm^{-1} that correspond to hindered translations and rotations of the two ions in the crystal lattice.

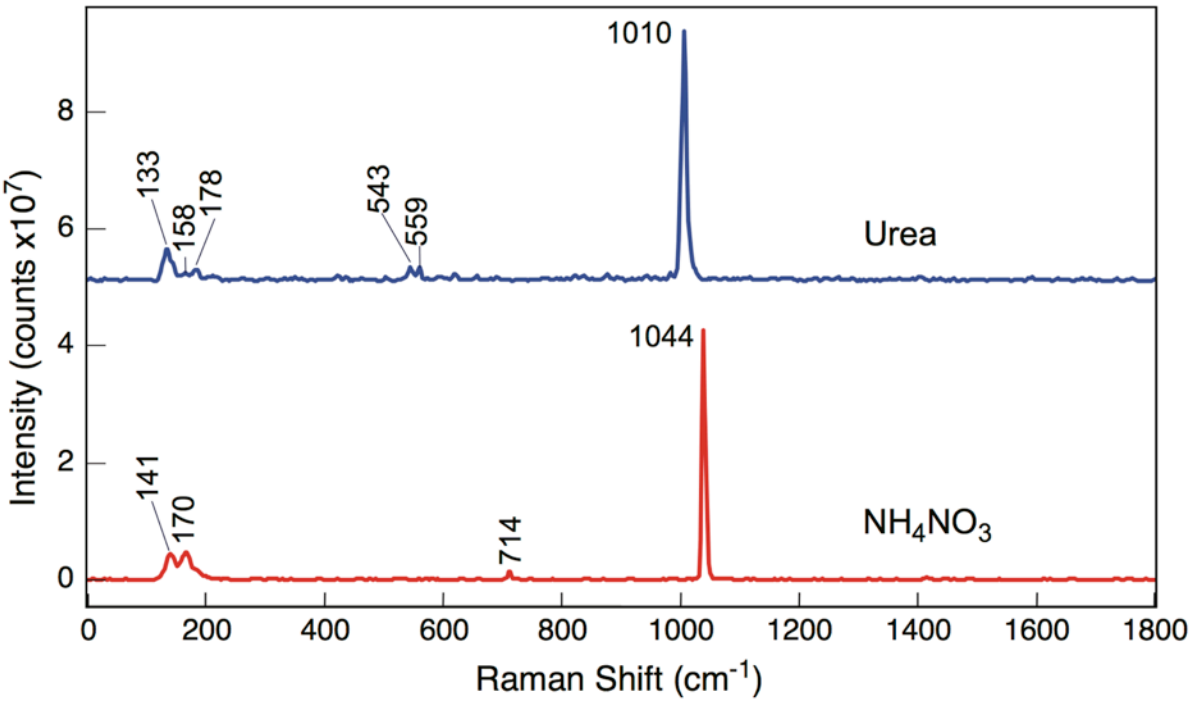

Fig 3.14 – The Raman spectra of salts measured at a distance of 5 m with a laser power of 8.6 mJ per pulse and a camera gain of 150. The Littrow angle was set to retro-reflect 554 nm light. The accumulation time was 10 seconds.

3.6.5 The Raman Spectra of Organic Compounds at 5 meters

Fig 3.15 depicts the Raman spectra of several organic compounds as measured with SHRS, including acetonitrile, naphthalene, anthracene and cyclohexane. The Littrow angle was selected to try to incorporate as many of the major bands of the four organic materials while maintaining relatively similar bandpass for all spectra. The Raman spectrum of acetonitrile[75] contains vibrational modes at 918 cm^{-1} attributable to a symmetric carbon-carbon stretch, a vibrational mode at 1376 cm^{-1} originating from a symmetric methyl combination band, a carbon-nitrogen symmetric stretching mode at 2251 cm^{-1}, and a symmetric stretch of the methyl group at 2941 cm^{-1}. The Raman spectrum of naphthalene[76] includes the symmetric ring-breathing (ν_5) apparent at 1383 cm^{-1}, two separate symmetric carbon-carbon stretches at 1465 and 1577 cm^{-1}, and a symmetric

carbon-hydrogen stretch (ν_1) at 3056 cm^{-1}. The Raman spectrum of anthracene[77-78] illustrated in **Fig 3.15** shows seven bands. There are two in plane carbon-hydrogen bending vibrations at 1165 and 1186 cm^{-1} with A_{1g} and B_{1g} symmetry, respectively. In addition, there are three totally symmetric carbon-carbon stretches at 1261, 1402 and 1559 cm^{-1}, and two in-plane carbon-carbon stretches at 1480 and 1632 cm^{-1} with B_{1g} symmetry. The Raman spectrum of cyclohexane[75] presented in **Fig 3.15** contains seven principle vibrational modes. The vibrational modes that account for the spectral features shown include a carbon-carbon stretch (A_{1g}) at 802 cm^{-1}, a carbon-carbon stretch (E_g) at 1027 cm^{-1}, a CH_2 twist (E_g) at 1266 cm^{-1}, a CH_2 scissor (E_g) at 1443 cm^{-1}, and three CH_2 symmetric stretches (A_{1g}) at 2853, 2922, and 2938 cm^{-1}.

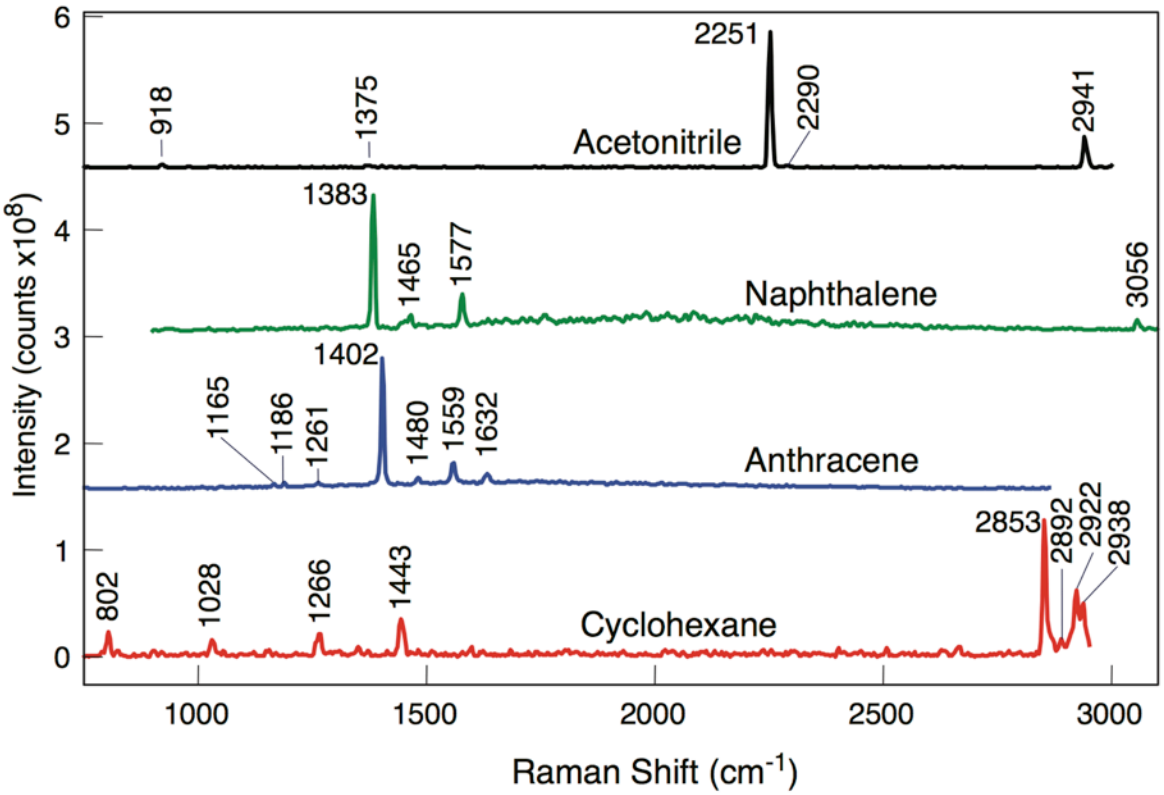

Fig 3.15 - The Raman spectra of organic compounds measured at a distance of 5 m with a laser power of 8.6 mJ per pulse and a camera gain of 250 (150 for naphthalene). The accumulation time was 10 seconds. The Littrow angle for acetonitrile, naphthalene, anthracene and cyclohexane was set to retro-reflect 586, 599, 589 and 592 nm light, respectively.

3.6.6 The Signal to Noise Ratio Plot

The data reduction section of this chapter described how the noise could be manipulated in order to produce a Raman spectrum with white noise. Upon dividing this white noise Raman spectrum by the mean of the noise, a new spectrum is created where the mean of the noise of all frequencies is equal to one and so in effect, the y-axis represents signal-to-noise ratio. Any of the Raman spectra in this chapter could have been presented as signal-to-noise spectra by simply divided said spectra by the mean of the noise; however, the traditional Raman spectra were preferred in order to demonstrate the high-throughput so often touted by SHRS experimentalist and to maintain a level of consistency with other SHRS publications for ease of direct comparison. In **Fig 3.16**, the signal-to-noise Raman spectrum of cyclohexane is illustrated.

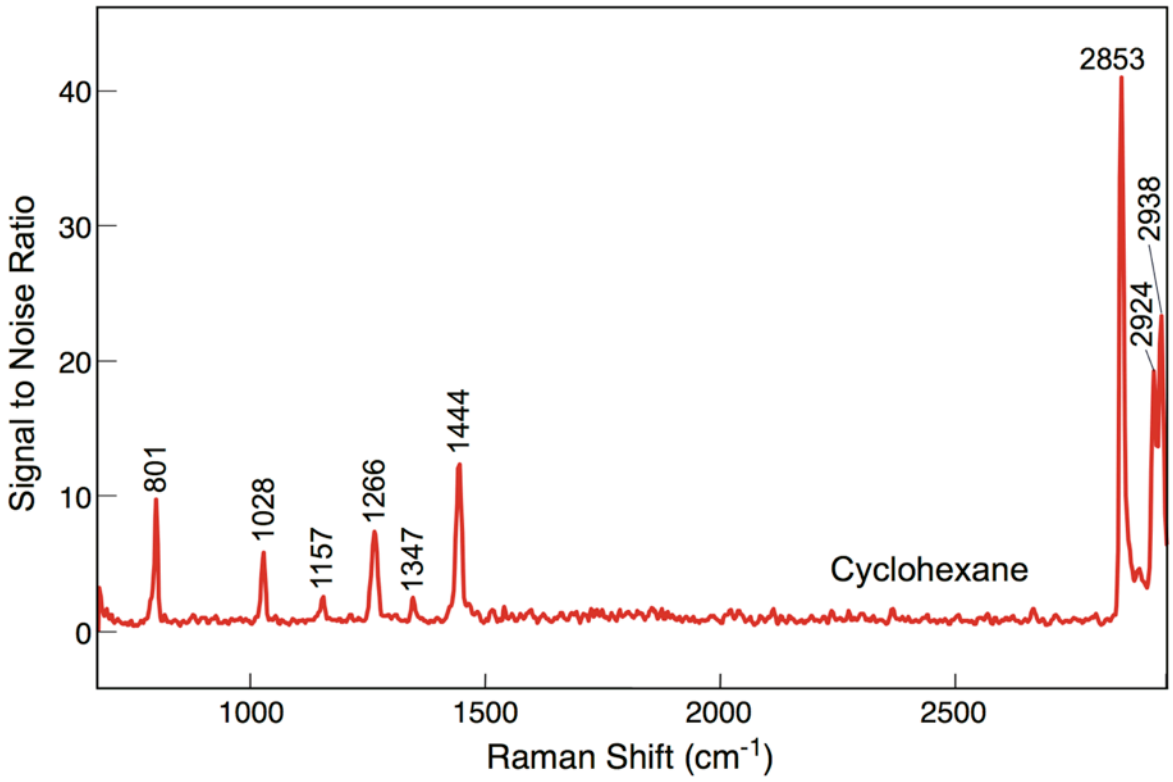

Fig 3.16 – The signal-to-noise Raman spectrum of cyclohexane, measured at 5 meters with a laser power of 8.6 mJ per pulse, 250 camera gain and 60 second accumulation time. The Littrow angle was set to retro-reflect 592 nm light. The peak at 2892 cm^{-1} is present but not labeled.

3.7 Conclusions

Spatial heterodyne Raman spectrometers record Raman spectra by imaging crossed wavefronts caused by frequency dependent reflection angles off of diffraction gratings. The crossed wavefronts produce a superposition of spatial fringes that may be converted to a Raman spectrum by Fourier transform. Since every pixel recording the crossed wavefronts contains information on every frequency, the noise produced by SHRS should maintain a constant power spectral density in all frequencies. Upon conversion from the spatial frequency domain to the spectral domain, the expected constant power spectral density is converted to a sinc(σ) profile due to the fact that the Fourier transform of a rectangular pulse has a sinc(σ) frequency response. This frequency dependent intensity response may be corrected by fitting a pseudovoigt function to the sinc(σ) profile of the shot noise, and thereafter by using the fitted curve as an intensity calibration for Raman spectra. This technique has two principle benefits. First, it produces Raman spectra with white noise. Second, it can produce Raman spectra where the intensity axis is equal to signal-to-noise ratio.

The instrument design and data reduction procedure described above was utilized to measure the Raman spectra of carbonate, sulfate and silicate minerals along with a selection of inorganic salts and organic compounds. Several mineral spectra, including zircon, topaz, sodalite, spodumene and fluorapatite, had never been measured before by SHRS, which is indicative of the advancing nature of this work. SHRS is capable of measuring the Raman spectra of a larger area of minerals and provides much better spectral resolution of spectral lines than corresponding dispersive instrument. SHRS is not as effective in measuring the Raman spectra of minerals at the current state-of-the-art as compared to dispersive instruments, especially when the laser spot size is smaller than 10 mm and thus the spot size does not overfill the entrance slit of the dispersive spectrometer. It is not uncommon for SHRS to require ten or twenty times longer accumulation times than modern dispersive based instruments when measuring the same sample. One of the major contributing factors to this reality is the multiplex disadvantage that stems from the fact that all frequencies are measured simultaneously in every pixel of the ICCD. Since the noise is proportional to the square of the signal and the noise is constant in all frequencies, a strong Raman line will create a rising floor of noise that can wash out low intensity

spectral features. Another contributing factor is the fact that spectral features must produce interference fringes over a large area of the ICCD and thus requires a great deal of photons. This fact is in stark contrast to dispersive instruments, which localizes photons of a given frequency into a small area of the recording device. Finally, SHRS records intensity of a spectral feature by quantifying the fringe contrast. As the number of spectral features superimposed on another increases, the fringe contrast necessarily decreases, especially as the phase difference between the bands increases away from the zero path difference.

Chapter 4: Future Work

In the preceding chapters, it was demonstrated that with a pulsed 532-nm laser excitation a spatial heterodyne spectrometer (SHS) could be used to measure the Raman spectra of carbonate, sulfate and silicate minerals at distances of 0.1, 0.5 and 5 meters. Furthermore, it was shown that SHS spectra could be intensity calibrated by modeling the experimental noise with a pseudovoigt curve, thereafter creating Raman spectra with white noise. Future work related to SHS will primarily concern itself with improving the sensitivity of SHS, increasing the bandpass, and applying SHS to a greater number of situations. Some untested ideas on how to achieve these aims will be outlined below.

4.1 Improving the Sensitivity of SHS

The principle limitation to the sensitivity of SHS is the multiplex disadvantage. In a SHS experiment, every pixel contributes signal to every frequency and so noise in any pixel contributes noise to all frequencies. This is what is known as the multiplex disadvantage. In effect, the multiplex disadvantage creates a rising floor of noise and allows strong spectral features to mask weak spectral features.

One idea to overcome the multiplex disadvantage is to disperse the light before entering the interferometer via a prism. The goal of this instrument design is to create a frequency gradient along the y-axis of the diffraction gratings and ICCD. This instrument design has a few predicted effects. First, counts contributing to a given spectral feature are now localized in a few rows of the ICCD as opposed to the whole ICCD. This will allow weak spectral features that contribute relatively few photons to produce a stronger interference fringe by concentrating the limited photons in a smaller space. Second, the fringe contrast will be improved because spectral features with different wavelengths and thus different phase slopes that when superimposed diminishes fringes contrast are now located on different areas of the ICCD.

A second idea on how to overcoming the multiplex disadvantage is to calculate the frequency spectrum via a maximum likelihood estimator. Bialkowski[1] has published a detailed exposition on how to calculate an emission spectrum via a maximum likelihood estimator from a Michelson interferogram. This method estimates the most likely input

that caused a given interferogram as recorded by the CCD while taking into account the shot noise as modeled by a Poisson distribution. Bialkowski found that he was able to measure emission spectra without white noise and found that the resolution or line-width was improved.

The third method to improve the sensitivity SHS for Raman spectroscopy is to collect more light. In the current Michelson variant design, fifty percent of light is lost out the entrance aperture after the light is reflected off the diffraction gratings. This may be improved to 67% by changing the instrumental design to a common-path, circular interferometer as described by Harlander[2] and Hosseini[3].

4.2 Improving the Bandpass of SHS

The ideal bandpass for a Raman spectrometer should cover the low frequency lattice modes of solids above 100 cm^{-1}, and the high frequency stretches such as carbon-hydrogen, nitrogen-hydrogen or oxygen-hydrogen stretches from 2800 to 3600 cm^{-1}. Therefore, the ideal bandpass should cover a frequency range from 0 to 3600 cm^{-1} in a single measurement. With 532-nm laser excitation, this bandpass corresponds to a 534.8-658.0 nm spectral range. It was shown in Chapter III that SHRS could achieve a bandpass of 2500 cm^{-1} (79.2 nm) by introducing a small tilt along the y-axis of a single grating followed by two-dimensional Fourier transform. Using 532 nm excitation, the simplest way to improve the bandpass is to either decrease the groove density on the diffraction gratings or increase the pixel density on the ICCD. Increasing the pixel density on the ICCD is the better method because it does not simultaneously degrade the resolution of the interferometer but instead increases the bandpass by increasing the sampling frequency of the instrument. Princeton Instruments, the manufacturer of the ICCD used in this work, has recently developed a new ICCD with 12.8 μm by 12.8 μm pixel size as opposed to the 26 μm by 26 μm pixel size used in the present work. By utilizing this new ICCD with reduced pixel size, the bandpass could be doubled without changing any other aspect of the experimental design.

Another method of improving the bandpass with visible laser excitation is to construct an SHS where the diffraction gratings are reflected in an echelle[4] orientation. In this experimental design, a low groove density diffraction grating reflects multiple, high

diffraction order light onto the camera. The separate diffraction orders represent different parts of a given spectrum, which can be intelligently combined in post-processing. It should be mentioned that the Raman shifts of materials are independent of laser excitation. With 266 nm UV excitation, the Raman shift of 100-3600 cm^{-1} corresponds to spectral range of 266.7 - 294.2 nm, i.e., a band pass of 27.5 nm. By changing the excitation wavelength to UV region one could get the Raman spectra of organic, inorganic and minerals in the full spectral range using 300 groove/mm gratings in SHRS as has been demonstrated by Lamsal and Angel[5].

4.3 Applications of SHS

Raman spectroscopy may be used as a temperature probe by calculating the ratio of Stokes to anti-Stokes Raman lines. The intensity of a Raman transition depends upon the population of the initial state. The population of initial states depends upon the temperature and the energy difference ($\Delta\nu$) between states. The greater the energy difference between states, the more likely a molecule is in the ground vibrational energy state. Conversely, the lower the temperature, the more likely the molecule is in the ground vibrational energy state. At room temperature, the vast majority of molecules occupy the ground vibrational state and so transitions from the ground vibrational state to an excited state by means of inelastic scattering are typically the most prevalent. As the temperature of a sample increases, the number of molecules in an excited vibrational state increases. When this occurs, transitions by means of inelastic scattering from an excited vibrational state to a less energetic vibrational state become more prevalent. The population of a certain molecule in a certain vibrational state may be calculated by means of Boltzmann's distribution. The ratio of Stokes to anti-Stokes Raman lines quantifies the population of each vibrational state, according to Eq. (4.1).

$$\frac{I_{Stokes}}{I_{anti-Stokes}} = \frac{(\nu_0-\Delta\nu)^4}{(\nu_0+\Delta\nu)^4} e^{(-hc\Delta\nu/kT)} \quad (4.1)$$

where h is Planck's constant, k is Boltzmann's constant, T is temperature in Kelvin, ν_0 is the wavenumber of the excitation laser and $\Delta\nu$ is the Raman shift due to a normal mode of vibration of the molecule (ν_{vib}) in cm^{-1}. Since SHS can measure both Stokes and anti-Stokes Raman bands simultaneously, it can be used as a type of time series temperature probe.

References

Chapter 1: Raman Spectroscopy – Theory and Laboratory Spectra of Geologic Materials

1. Raman C.V. (1928) A change of wave-length in light scattering. *Nature*, **121**, 619-619.
2. Raman C.V. & Krishnan K.S. (1928) A new type of secondary radiation. *Nature*, **121**, 501-502.
3. White W.B., & De Angelis B.A. (1967) Interpretation of the vibrational spectra of spinels. *Spectrochimica Acta*, **A23**, 985-995.
4. White W.B. (1975) Structural interpretation of lunar and terrestrial minerals by Raman spectroscopy. pg 325-358 in *Infrared and Raman spectroscopy of Lunar and Terrestrial Minerals* (C. Karr, Jr., editor). Academic Press, New York.
5. McMillan P. (1985) Vibrational spectroscopy in the mineral sciences. pg 9-63 in: *Microscopic to Macroscopic—Atomic Environments to Thermodynamic Properties* (S.W. Kieffer and A. Navrotsky, editors). *Reviews in Mineralogy*, **14**, Chapter 2. Mineralogical Society of America, Washington, D.C.
6. McMillan P.F. and Hofmeister A.M. (1988) Infrared and Raman spectroscopy. pg 99-159 in *Spectroscopic Methods in Mineralogy and Geochemistry* (F.C. Hawthorne, editor). *Reviews in Mineralogy*, **18**, Chapter 4. Mineralogical Society of America, Washington, D.C.
7. Nasdala L., Smith D.C., Kaindl R. & Ziemann M.A. (2004) Raman spectroscopy: Analytical perspectives in mineralogical research. Pp. 281-343 in: *Spectroscopic Methods in Mineralogy, EMU Notes in Mineralogy*, **6** (A. Beran and E. Libowitzky, editors). European Mineralogical Union and Mineralogical Society of Great Britain and Ireland.
8. Dubessy J., Caumon M.C., Rull F. & Sharma S. (2012) Instrumentation in Raman spectroscopy: elementary theory and practice, pg. 83-172 in: *Applications of Raman Spectroscopy to Earth Sciences and Cultural Heritage* (J. Dubessy, F. Rull & M.C.

Caumon, editors). *EMU Notes in Mineralogy*, **12**, European Mineralogical Union and the Mineralogical Society of Great Britain & Ireland.

9. Colthup N.B., Daly L.H., & Wiberley S.E. (1975) Introduction to Infrared and Raman Spectroscopy. *Academic Press, New York*, **2**.
10. Nadungadi T.M.K. (1939) Effect of crystal orientation on the Raman spectrum of sodium nitrate. *Proceedings of Indian Academy of Sciences*, **A10**, 197-212.
11. Bhagvantam S. (1940) Effect of crystal orientation on the Raman spectrum of calcite. *Proceedings of Indian Academy of Sciences*, **A11**, 62-71.
12. Damen T.C., Porto S.P.S. & Tell B. (1966) Raman Effect in zinc oxide. *Physical Review*, **142,** 570-574.
13. Jaffé H.H. & Miller A.L. (1966) The Fates of Electronic Excitation Energy. *Journal of Chemical Education*, **43**, 469-473.
14. Panczer G., De Ligny D., Mendoza C., Gaft M., Seydoux-Guillaume A.M. & Wang X. (2012) Raman and fluorescence. pg. 1-22 in: *Applications of Raman Spectroscopy to Earth Sciences and Cultural Heritage* (J. Dubessy, F. Rull & M.C. Caumon, editors). *EMU Notes in Mineralogy*, **12.** European Mineralogical Union and the Mineralogical Society of Great Britain & Ireland.
15. Gaft M. & Nagli L. (2009) Time-resolved laser based spectroscopies for mineralogical research and applications. In: *Micro-Raman Spectroscopy and Luminescence Studies in the Earth and Planetary Sciences* (A. Gucsik, editor). Mainz, Germany, 2-4 April 2009, *American Institute of Physics (AIP) Conference Proceedings*, **1163**, 3-14.
16. Gaft M., Reinsfeld R. & Panczer G. (2005) Modern Luminescence Spectroscopy of Minerals and Materials. *Springer-Verlag, Berlin Heidelberg, Germany*.
17. Kittel C. (1976) Introduction to Solid State Physics. *John Wiley & Sons, New York*, **5**.
18. de Faria D.L.A., Venâncio Silva S. & de Oliveira M.T. (1997) Raman microspectroscopy of some iron oxides and oxyhydroxides. *Journal of Raman Spectroscopy*, **28**, 873-878.
19. Nieuwoudt M.K., Comins J. D. & Cukrowski I. (2011) The growth of the passive film on iron in 0.05 MNaOH studied *in situ* by Raman micro-spectroscopy and electrochemical polarisation. Part I: near-resonance enhancement of the Raman

spectra of iron oxide and oxyhydroxide compounds. *Journal of Raman Spectroscopy*, **42**, 1335-1339.

20. Cornell R.M. & Schwertmann U. (2003) The Iron Oxides. Structure, Reactions, Ocurrences and Uses. *Wiley-VCH Verlag GmbH & Co. KGaA, Weinheim, FRG*, **2**.
21. Urmos J.P., Sharma S.K. & Mackenzie F.T. (1991) Characterization of some biogenic carbonates with Raman spectroscopy. *American Mineralogist,* **76**, 641-646.
22. Cotton F.A. (1963) Chemical Applications of Group Theory. *Wiley Publisher, New York*.
23. Bhagavantam S. & Venkatarayudu T. (1969) Theory of Groups and its Applications to Physical Problems. *Academic Press, New York*.
24. Ferraro J.R. & Ziomek J.S. (1969) Introductory Group Theory and Its Application to Molecular Structure. *Plenum Press, New York*.
25. Rull F. (2012) The Raman effect and the vibrational dynamics of molecules and crystalline solids. pg. 1-60 in: *Applications of Raman Spectroscopy to Earth Sciences and Cultural Heritage* (J. Dubessy, F. Rull & M.C. Caumon, editors). *EMU Notes in Mineralogy,* **12**, European Mineralogical Union and the Mineralogical Society of Great Britain & Ireland.
26. Harris D.C. & Bertolucci M.D. (1989) Symmetry and Spectroscopy: An Introduction to Vibrational and Electronic Spectroscopy. *Dover Publications*, 1-543.
27. Herzberg G. (1945) Molecular Spectra and Molecular Structure. II. Infrared and Raman Spectra of Polyatomic Molecules. *Van Nostrand Reinhold, New York*.
28. Ferigle S.M. & Meister A.G. (1952) Selection rules for vibrational spectra of linear molecules. *American Journal of Physics*, **20**, 421-428.
29. Buback M. & Schulz K.R. (1976) Raman Scattering of Pure Ammonia to High Pressures and Temperatures. *The Journal of Physical Chemistry*, **80**, 2478-2482.
30. Bertie J.E. & Bell, J.W. (1971) Unit cell group and factor group in the theory of the electronic and vibrational spectra of crystals. *Journal of Chemical Physics*, **54**, 160-162.
31. Bhagavantam S. & Venkatarayudu T. (1939) Raman effect in relation to crystal structure. *Proceedings of Indian Academy Science*, **A9**, 224-258.

32. Fateley W.G., Dollish F.R., McDevitt N.T. & Bentley F. F. (1972) Infrared and Raman selection rules for molecular and lattice modes. *Wiley, New York*.
33. Salthouse J.A. & Ware M. J. (1972) Point Group Character Tables and Related Data. *Cambridge University Press, Cambridge, England*.
34. Adams D.M. & Newton D.M. (1970a) Tables for factor group analysis of the vibrational spectra of solids. *Journal of Chemical Society*, (A) **1970**, 2822-2827.
35. Adams D.M. & Newton D.M. (1970b) Tables for Factor Group Analysis. pg. 58, *Beckman-RICC Ltd. England*.
36. Halford R.S. (1946) Motions of molecules in condensed systems: I. Selection rules, relative intensities, and orientation effects for Raman and infrared spectra. *Journal of Chemical Physics*, **74**, 8-15.
37. Hornig D.F. (1948) The vibrational spectra of molecules and complex ions in crystals. I. General theory. *Journal of Chemical Physics*, **16**, 1063-1076.
38. Winston H. & Halford R.S. (1949) Motions of molecules in condensed systems: V. Classification of motions and selection rules for spectra according to space symmetry. *Journal of Chemical Physics*, **17**, 607-616.
39. Maraduddin A.A. & Vosko S.H. (1968) Symmetry properties of the normal vibrations of a crystal. *Reviews of Modern Physics*, **40**, 1-37.
40. Warren J. L. (1968) Further considerations on the symmetry properties of the normal vibrations of a crystal. *Reviews of Modern Physics*, **40**, 38-76.
41. Ferraro J.R. (1975) Factor group analysis for some common minerals. *Applied Spectroscopy*, **29**, 418-420.
42. DeAngeles B. A., Newnham R.E. & White W.B. (1972) Factor group analysis of the vibrational spectra of crystals: A review and consolidation. *American Mineralogist*, **57**, 255-268.
43. Aroyo M.I., Perez-Mato J.M., Orobengoa D., Tasci E., de la Flor G. & Kirov A. (2011) Crystallography online: Bilbao crystallographic server. *Bulgarian Chemistry Communications*, **43**, 183-197.
44. Aroyo M.I., Perez-Mato J.M., Capillas C., Kroumova E., Ivantchev S., Madariaga G., Kirov A., & Wondratschek H. (2006a) Bilbao crystallographic server I: Databases

and crystallographic computing programs. *Zeitschrift für Kristallographie*, **221**, 15-27.

45. Aroyo M.I., Kirov A., Capillas C., Perez-Mato J.M. & Wondratschek H. (2006b) Bilbao crystallographic server II: Representations of crystallographic point groups and space groups. *Acta Crystallographica*, **A62**, 115-128.
46. Porto S.P.S., Giordmaine J.A. & Damen T.C. (1966) Depolarization of Raman scattering in calcite. *Physical Review*, **147**, 608-611.
47. De La Pierre M., Carteret C., Maschio L., André E., Orlando R. & Dovesi R. (2014) The Raman spectrum of $CaCO_3$ polymorphs calcite and aragonite: A combined experimental and computational study. *Journal of Chemical Physics*, **140**, 164509/1-12.
48. Pandya N., Sharma S.K. & Muenow D.W. (1988) Calibration of a multichannel micro-Raman spectrograph with plasma lines of argon and krypton ion lasers. Pp. 171-174 in: *Microbeam Analysis*—1988 (D. E. Newbury, editor). San Francisco Press Inc.
49. Storrie-Lombardi M.C., Hug W.F., McDonald G.D., Tsapin AI. & Nealson, K.H. (2011) Hollow cathode ion lasers for deep ultraviolet Raman spectroscopy and fluorescence imaging. *Review of Scientific Instruments*, **72**, 4452-4459.
50. Beegle L.W., Bhartia R., DeFlores L., Darrach M., Kidd R.D., Abbey W., Asher S., Burton A., Clegg S., Conrad P.G., Edgett K., Ehlmann B., Langenhorst F., Fries M., Hug W., Nealson K., Popp J., Sorbon P., Steele A., Wiens R. & Williford K. (2014) SHERLOC: Scanning habitable environments with Raman and luminescence for organics and chemicals, an investigation for 2020. *Lunar and Planetary Science Conference*, **45**, 2835 (abstract). www.hou.usra.edu/meetings/lpsc2014/pdf/2835.pdf
51. Angel S.M., Carrabba M. & Cooney T.F. (1995) The utilization of diode lasers for Raman spectroscopy. *Spectrochimica Acta,* **A51**, 1779-1799.
52. Cooney T.F., Skinner H.T. & Angel S.M. (1995) Evaluation of external-cavity diode lasers for Raman spectroscopy. *Applied Spectroscopy*, **49**, 1846-1851.
53. Cooper J.B., Flecher P.E., Albin S., Vess T.M. & Welch W.T. (1995) Elimination of mode hopping and frequency hysteresis in diode laser Raman spectroscopy: The advantages of a distributed Bragg reflector diode laser for Raman excitation. *Applied Spectroscopy*, **49**, 1692-1698.

54. McCreery R.L. (2000) Raman Spectroscopy for Chemical Analysis. *John Wiley & Sons: New York*.

55. Wang Z., Cooney T.F. & Sharma S.K. (1995) *In situ* structural investigation of iron-containing silicate melts and glasses. *Geochimica Cosmochimica Acta*, **59**, 1571-1577.

56. Wang W., Major A. & Paliwal J. (2012) Grating-stabilized external cavity diode lasers for Raman spectroscopy—A review. *Applied Spectroscopy Reviews*, **47**, 116-143.

57. Aminzadeh, A. (1997) Fluorescence bands in the FT-Raman spectra of some calcium minerals. *Spectrochimica Acta*, **A53**, 693-797.

58. Kaszowska Z., Malek K., Staniszewska-Slezak E. & Niedzielska K. (2016) Raman scattering or fluorescence emission? Raman spectroscopy study on lime-based building and conservation materials. *Spectrochimica Acta*, **A169**, 7-15.

59. Sharma S.K. (1989) Applications of advanced Raman techniques in earth sciences. *Vibrational Spectra and Structure*, **17B**, 513 568.

60. Blacksberg J., Rossman G. R. & Gleckler A. (2010) Time-resolved Raman spectroscopy for in situ planetary mineralogy. *Applied Optics*, **49**, 4951-4962.

61. Delhaye M. & Dhamelincourt P. (1975), Raman microprobe and microscope with laser excitation. *Journal of Raman Spectroscopy,* **3**, 33-43.

62. Dhamelincourt P., Wallart F., Leclercq M., N'Guyen A.T. & Landon D.O. (1979) Laser Raman molecular microprobe (MOLE). *Analytical Chemistry*, **51**, 414A-421A.

63. Li Z. & Deen M.J. (2014) Towards a portable Raman spectrometer using a concave grating and a time-gated CMOS SPAD. *Optics Express*, **22**, 18736-18747.

64. Arns J.A. (1995) Holographic transmission gratings improve spectroscopy and ultrafast laser performances, *Proc. SPIE*, **2404**, 174–181.

65. Arns J.A., Colburn W.S. & Barden S.C. (1999) Volume phase gratings for spectroscopy, ultrafast laser compressors, and wavelength division multiplexing, *Proc. SPIE*, **3779**, 313- 323.

66. Battey D.E., Slater J.B., Wludyka R., Owen H., Pallister D.M. & Morris M.D. (1993) Axial transmissive f/1.8 imaging Raman spectrograph with volume-phase holographic filter and grating. *Applied Spectroscopy*, **47**, 1913-1919.

67. Wang A., Haskin L.A., Lane A.L., Wdowiak T.J., Squyres S.W., Wilson R.J., Hovland L.E., Manatt K.S., Raouf N. & Smith C. D. (2003) Development of the Mars Microbeam Raman Spectrometer (MMRS). *Journal of Geophysical Research,* **108 E1,** 5005/1-18.

68. Sharma S. K., Misra A.K. & Sharma B. (2005) Portable remote Raman system for monitoring hydrocarbon, gas hydrates and explosives in the environment. *Spectrochimica Acta*, **A61**, 2404-2412.

69. Gasda P.J., Acosta-Maeda T.E., Lucey P.G., Misra A.K., Sharma S.K. & Taylor G.J. (2015) Next generation laser-based standoff spectroscopy techniques for Mars exploration. *Applied. Spectroscopy,* **69**, 173-192.

70. Lebedkin S., Blum C., Stürzl, N., Hennrich, F. & Kappes, M.M. (2011) A low wavenumber extended confocal Raman microscope with very high laser excitation line discrimination. *Review of Scientific Instruments*, **82**, 013705/1-6.

71. Jennings D.E., Weber A. & Brault J. W. (1986) Raman spectroscopy of gases with a Fourier transform spectrometer: the spectrum of D_2. *Applied Optics*, **25**, 284-290.

72. Hirschfeld T. & Chase B. (1986) FT-Raman spectroscopy: Development and justification. *Applied Spectroscopy*, **40**, 133-137.

73. Chase D.B (1986) Fourier transform Raman spectroscopy. *Journal of American Chemical Society*, **108**, 7485-7488.

74. Zhao J. & McCreery R.L. (1996) Multichannel Fourier transform Raman spectroscopy: Combining the advantages of CCDs with interferometry. *Applied Spectroscopy*, **50**, 1209-1214.

75. Zhao J. & McCreery R.L. (1997) Multichannel FT-Raman spectroscopy: Noise analysis and performance assessment. *Applied Spectroscopy*, **51**, 1687-1697.

76. Gomer N., Gordon C., Lucey P., Sharma S., Carter J. & Angel S. (2011) Raman spectroscopy using a spatial heterodyne spectrometer: Proof of concept. *Applied Spectroscopy*, **65**, 849-857.

77. Hu G., Xiong W., Shi H., Li Z., Shen J., & Fang X. (2015) Raman spectroscopic detection for liquid and solid targets using a spatial heterodyne spectrometer. *Journal of Raman Spectroscopy*, **47**, 289-298.

78. Lamsal N., Sharma S.K., Acosta T.E., & Angel S.M. (2016) UV standoff Raman measurements using a gated spatial heterodyne Raman spectrometer. *Applied Spectroscopy,* **70**, 666-675.
79. Rosasco G.J., Etz E.S., & Cassatt W.A. (1975) The analysis of discrete fine particles by Raman spectroscopy. *Applied Spectroscopy,* **29**, 396-404.
80. Adams D.M., Sharma S.K. & Appleby R. (1977) Spectroscopy at very high pressures: Part 14. Laser Raman scattering in ultra-small samples in the diamond anvil cell. *Applied Optics,* **16***,* 2572-2575.
81. Sharma S.K. (1979) Raman spectroscopy at very high pressure. *Carnegie Institution of Washington Year Book*, **78**, 660-665.
82. Denson S.C., Pommier C.J.S. & Denton M.V. (2007) The impact of array detectors on Raman spectroscopy. Journal of Chemical Education, 84, 67-74.
83. Matousek P., Towrie M., Stanley A. & Parker A.W. (1999) Efficient rejection of fluorescence from Raman spectra using picosecond Kerr gating. *Applied Spectroscopy*, **53**, 1485-1489.
84. Misra A.K., Sharma S.K., Chio C. H., Lucey P. G. & Lienert B. (2005) Pulsed remote Raman system for daytime measurements of mineral spectra. *Spectrochimica Acta*, **A61**, 2281-2287.
85. Carter J.C., Scaffidi J., Burnett S., Vasser B., Sharma S.K. & Angel S.M. (2005), Stand-off Raman detection using dispersive and tunable filter based systems. *Spectrochimica Acta,* **A61**, 2288-2298.
86. Blacksberg J., Rossman G. R. & Gleckler A. (2010) Time-resolved Raman spectroscopy for in situ planetary mineralogy. *Applied Optics*, **49**, 4951-4962.
87. Sharma S.K. (2007) New trends in telescopic remote Raman spectroscopic instrumentation. *Spectrochimica Acta*, **A68**, 1008-1022.
88. Wang A., Haskin L.A. & Cortez, E. (1998) Prototype Raman spectroscopic sensor for in situ mineral characterization on planetary surfaces. *Applied Spectroscopy*, **52**, 477-487.
89. Lucey P.G., Cooney T.F. & Sharma S.K. (1998) A remote Raman analysis system for planetary landers. *Lunar and Planetary Science Conference*, **29***,* Abstract 1354.

90. Wiens R.C., Maurice S., McCabe K., Cais P., Anderson R.B., Beyssac O., Bonal L., Clegg S., Deflores L., Dromart G., Fischer W.W., Forni O., Gasnault O., Grotzinger J.P., Johnson J.R., Martinez-Frias J., Man-gold N., McLennan S., Montmessin F., Rull F., Sharma S.K., Sautter V., Lewin E., Cloutis E., Poulet F., Bernard S., McConnochie T., Lanza N., Newsom H., Ollila A., Leveille R., Le Mouelic S., Lasue J., Melikechi N., Meslin P.-Y., Misra A., Grasset O., Angel S.M., Fouchet T., Beck P., Bridges N., Bousquet B., Fabre C., Pinet P., Benzerara K., & Montagnac G. (2016) The SUPERCAM remote sensing instrument suite for Mars 2020. *Lunar and Planetary Science Conference*, **47**, 1332 (abstract).

91. Angel S.M., Gomer N.R., Sharma S.K. & McKay C. (2012) Remote Raman spectroscopy for planetary exploration: A review. *Applied Spectroscopy,* **66**, 137-150.

92. Egan M.J., Angel S.M. & Sharma S.K. (2016) Standoff spatial heterodyne Raman spectrometer for mineralogical analysis, *XII International Conference-GeoRaman-2016 Abstract Volume*, Novosibirsk, Russia, June 9-15, p. 39.

93. McKeown D.A. (2005) Raman spectroscopy and vibrational analyses of albite: from 25°C through the melting temperature. *American Mineraogist.* **90**, 1506-1517.

94. Freeman J.R., Wang A., Kuebler K.E., Jolliff B.L. & Haskin L.A. (2008) *Canadian Mineralogist*, **46**, 1477-1500.

95. Spinella F., Barrata G.A. & Strazzulla G. (1991) An apparatus for in situ Raman spectroscopy of ion-irradiated frozen target. *Review of Scientific Instruments*, **62**, 1743-1745.

96. Ferini G., Baratta G.A. & Palumbo M.E. (2004) A Raman study of ion irradiated icy mixtures. *Astronomy* & *Astrophysics,* **414**, 757-766.

97. Sonwalker N., Sunder S.S. & Sharma S.K. (1991) Raman microprobe spectroscopy of icing on metal surfaces. *Journal of Raman Spectroscopy*, **22**, 551-557.

98. Elman B.S., Dresselhaus M.S., Dresselhaus G., Maby E.W. & Mazurek H. (1981) Raman scattering from ion-implanted graphite. *Physical Review* B, **24,** 1027-1034.

99. Strazzulla G. & Baratta, G.A. (1992) Carbonaceous material by ion irradiation in space. *Astronomy and Astrophysics*, **266**, 434-438.

100. Strazzulla G., Baratta G.A., & Palumbo M.E. (2001) Vibrational spectroscopy of ion-irradiated ices. *Spectrochimica Acta*, **A57**, 825-842.

101. Bennett C.J., Brotton S.J., Jones B.M., Misra A.K., Sharma S.K. & Kaiser R.I. (2013) A novel high sensitivity Raman spectrometer to study pristine and irradiated interstellar ice analogs. *Analytical Chemistry*, **85**, 5659-5665.

102. Pasteris J.D., Kuehn C.A. & Bodnar R.J. (1986): Applications of the laser Raman microprobe Ramanor U-1000 to hydrothermal ore deposits: Carlin as an example. *Economic Geology*, **81,** 915-930.

103. Fries M. & Steele A. (2011) Raman spectroscopy and confocal Raman imaging in mineralogy and petrography. Pp. 111-133 in: *Confocal Raman Microscopy* (T. Dieing, O. Hollricher and J. Toporski, editors), *Springer Series in Optical Sciences*, **158**, Springer-Verlag Berlin and Heidelberg, Germany.

104. Frezzotti M.L., Tecce F. & Casagli A. (2012) Raman spectroscopy for fluid inclusion analysis. *Journal of Geochemical Exploration*, **112**, 1-20.

105. Roedder E. (1984) Nondestructive methods of determination of inclusion composition. Pp. 79-108 in: *Fluid Inclusions* (E. Roedder, editor), *Reviews in Mineralogy*, **12**, Mineralogical Society of America, Washington, D.C.

106. Sharma S.K., Hoering T.C. & Yoder H.S., Jr. (1979a) Quenched melts of akermanite compositions with and without CO_2-characterization by Raman spectroscopy and gas chromatography. *Carnegie Institution Washington Year Book,* **78***,* 537-542.

107. Sharma, S. K., D. Virgo, D. & Mysen, B.O. (1979b) Raman study of the coordination of aluminum in jadeite melts as function of pressure. *American Mineralogist,* **64***,* 779-787.

108. Sharma S. K. & Simons B. (1981) Raman study of crystalline polymorphs and glasses of spodumene ($LiAlSi_2O_6$) composition quenched from various pressure. *American Mineralogist*, **66**, 118-126.

109. Sharma S.K., Mammone J.F. & Nicol M.F. (1981) Ring configurations in vitreous silica - a Raman spectroscopic investigation. *Nature,* **292***,* 140-141.

110. Sharma S.K., Philpotts J.A. & Matson D.W. (1985) Ring distributions in alkali- and alkaline-earth alumino-silicate framework glasses—a Raman spectroscopic study. *Journal of Non-Crystalline Solids,* **71***,* 403-410.

111. Sharma S.K., Yoder H.S., Jr. & Matson D.W. (1988) Raman study of some melilites in crystalline and glassy states. *Geochimica et Cosmochimica Acta,* **52**, 1961-1967.

112. Sharma S.K. (1989) Applications of advanced Raman techniques in earth sciences. *Vibrational Spectra and Structure*, **17B**, 513 568.

113. Sharma S. K., Wang Z. & van der Laan S. (1996) Raman spectroscopy of oxide glasses at high pressure and high temperature. *Journal of Raman Spectroscopy,* **27**, 739-746.

114. Sharma S. K., Cooney T.F., Wang Z. & van der Laan, S.(1997) Raman band assignments of silicate and germanate glasses in light of high pressure and high temperature spectral data. *Journal of Raman Spectroscopy,* **28**, 679-709.

115. Matson D.W., Sharma S.K. & Philpotts J.A. (1983) The structure of high-silica alkali-silicate glasses—a Raman spectroscopic investigation. *Journal of Non-Crystalline Solids,* **58**, 323-352.

116. Matson D.W., Sharma S.K. & Philpotts J.A. (1986) Raman spectra of some tectosilicates and of glasses along the orthoclase-anorthite and nepheline-anorthite joins. *American Mineralogist,* **71**, 694-704.

117. Rai C.S., Sharma S.K., Muenow D.W., Matson D. W. & Byers C.D. (1983) Temperature dependence of CO_2 solubility in high-pressure quenched glasses of diopside composition. *Geochimica et Cosmochimica Acta,* **47**, 953-958.

118. Cooney T.F. & Sharma S.K. (1990) Structure of glasses in the system Mg_2SiO_4-Fe_2SiO_4, Mn_2SiO_4-Fe_2SiO_4, Mg_2SiO_4-$CaMgSiO_4$ and Mn_2SiO_4-$CaMnSiO_4$. *Journal of Non-Crystalline Solids*, **122**, 10-32.

119. Wang Z., Cooney T.F. & Sharma S.K. (1993) High-temperature structural investigation of iron-bearing glasses and melts. *Contributions to Mineralogy* & *Petrology*, **115**, 112-122.

120. Galeener F.L. (1982a) Planner rings in glasses. *Solid State Communication*, **44**, 1037-1040.

121. Galeener F.L. (1982b) Planner rings in vitreous silica. *Journal of Non-Crystalline Solids*, **49**, 53-62.

122. McMillan P.F. & Wolf G.H. (1995) Vibrational spectroscopy of silicate liquids. Pp. 247-314 in *Structure, Dynamics and Properties of Silicate Melts* (J.F Stebbins, P.F.

McMillan & D.B. Dingwell, editors), *Reviews in Mineralogy*, **32**. Mineralogical Society of America, Washington, D.C.

123. Kingma K.J. & Hemley R.J. (1994): Raman spectroscopic study of microcrystalline silica. *American Mineralogist*, **79**, 269-273.

124. Götze J., Nasdala L. Kleeberg R. & Wenzel M. (1998) Occurrence and distribution of "moganite" in agate/chalcedony: a micro-Raman, Rietfeld, and cathodoluminescence study. *Contribution to Mineralogy and Petrology,* **133,** 96-105.

125. McMillan P. F., Dubessy J. & Hemley R. (1996) Applications in Earth, planetary and environmental sciences. Pp. 289-365 in: *Raman Microscopy- Developments and Applications* (G. Turrell & J. Corset, editors). Academic Press, New York.

126. Mysen B.O & Richet P. (2005) *Silicate Glasses & Melts—Properties and Structure*. Elsevier, New York.

127. Rossano S. & Mysen B.O. (2012) Raman spectroscopy of silicate glasses and melts in geological systems. Pp. 321-366 in: *Applications of Raman Spectroscopy to Earth Sciences and Cultural Heritage* (J. Dubessy, F. Rull & M.-C. Caumon, editors). *EMU Notes in Mineralogy*, **12**, European Mineralogical Union and the Mineralogical Society of Great Britain & Ireland.

128. Haskin L.A., Wang A., Rockow K.M., Jolliff B.L., Korotev R.L. & Viskupic K.M. (1997) Raman spectroscopy for mineral identification and quantification for in situ planetary surface analysis: a point count method. *Journal of Geophysical Research*, **102**, 19293-19306.

129. Wang A., Jolliff B.L., Haskin L.A., Kuebler K.E. & Viskupic K.M. (2001) Characterization and comparison of structural and compositional features of planetary quadrilateral pyroxenes by Raman spectroscopy. *American Mineralogist*, **86**, 790-806.

130. Kuebler K.E., Jolliff B.L., Wang A. & Haskin L.A. (2006) Extracting olivine (Fo-Fa) compositions from Raman spectral peak positions. *Geochimica et Cosmochimica Acta*, **70**, 6201-6222.

131. Acosta T.E, Scott E.R.D., Sharma S.K. & Misra A.K. (2013) The pressures and temperatures of meteorite impact: Evidence from micro-Raman mapping of mineral

phases in the strongly shocked Taiban ordinary chondrite. *American Mineralogist*, **98**, 859-869.

132. Taran M., Koch-Müller M., Wirth R., Abs-Wurmbach I., Rhede D. & Greshake A. (2009) Spectroscopic studies of synthetic and natural ringwoodite, γ-$(Mg, Fe)_2SiO_4$. *Physics and Chemistry of Minerals*, **36**, 217–232.

133. Hemley R.J., Bell P.M. & Mao H.K. (1987) Laser techniques in high-pressure geophysics. *Science*, 237, 605-612.

134. Gillet P., Daniel I., Guyot F. Matas J. & Chervin J.C. (2000) A thermodynamic model for $MgSiO_3$-perovskite derived from pressure and temperature and volume dependence of the Raman mode frequencies. *Physics of the Earth and Planetary Interiors*, **117**, 361-384.

135. Goncharov A.F. (2012) Raman spectroscopy at high pressures. *International Journal of Spectroscopy*, **2012**, 617528/1-16.

136. Reynard B., Montagnac G., & Cardon H. (2012) Raman spectroscopy at high pressure and temperature for study of the Earth's mantle and planetary minerals. Pp. 367-390 in: *Applications of Raman Spectroscopy to Earth Sciences and Cultural Heritage* (J. Dubessy, F. Rull & M.-C. Caumon, editors). *EMU Notes in Mineralogy*, **12**, European Mineralogical Union and the Mineralogical Society of Great Britain & Ireland.

Chapter 2: Standoff Spatial Heterodyne Raman Spectrometer for Mineralogical Analysis

1. Harlander J.M., Roesler F.L., Reynolds R.J., Jaehnig K. & Sanders W. (1993) A Differential, Field-Widened Spatial Heterodyne Spectrometer for Investigations at High Spectral Resolution of the Diffuse Far Ultraviolet 1548 Å Emission Line from the Interstellar Medium. *Proc. SPIE*, **2006**, 139-148.
2. Harlander J.M., Roesler F.L., Cardon J.G., Englert C.R. & Conway R.R. (2002) SHIMMER: A Spatial Heterodyne Spectrometer for Remote Sensing of Earth's Middle Atmosphere. *Appl. Opt.*, **41**, 1343-1352.
3. Englert C.R., Stevens M.H., Siskind D.E., Harlander J.M. & Roesler F.L. (2010) Spatial Heterodyne Imager for Mesospheric Radicals on STPSat-1. J. Geophys. Res., **115**, D20306.
4. Mierkiewicz E.J., Reynolds R.J., Roesler F.L., Harlander J.M. & Jaehnig K.P. (2006) Detection of Diffuse Intersterllar [O II] Emission from the Milky Way Using Spatial Heterodyne Spectroscopy. *Astrophys. J.*, **650**, L63-L66.
5. N. R. Gomer (2012) *The Development of a Spatial Heterodyne Spectrometer for Raman Spectroscopy*. (Doctoral dissertation, University of South Carolina), pp. 142 http://scholarcommons.sc.edu/etd/684
6. Gomer N.R., Gordon C.M., Lucey P., Sharma S.K., Carter J.C. & Angel S.M. (2011) Raman Spectroscopy Using a Spatial Heterodyne Spectrometer: Proof of Concept. *Appl. Spectrosc.*, **65**, 849-857.
7. Lamsal N., Sharma S.K., Acosta T.E. & Angel S.M. (2016) Ultraviolet Stand-off Raman Measurements Using a Gated Spatial Heterodyne Raman Spectrometer. *Appl. Spectrosc.*, **70**, 666-675.
8. Lamsal N. & Angel S.M. (2015) Deep-Ultraviolet Raman Measurements Using a Spatial Heterodyne Raman Spectrometer (SHRS). *Appl. Spectrosc.*, **69**, 525-534.
9. Strange K.A., Paul K.C. & Angel S.M. (2016) Transmission Raman Measurements Using a Spatial Heterodyne Raman Spectrometer. *Appl. Spectrosc.*, **71**, 250-257.
10. Hu G., Xiong W., Shi H., Li Z., Shen J. & Fang X. (2016) Raman Spectroscopic Detection for Liquid and Solid Targets Using a Spatial Heterodyne Spectrometer. *J. Raman Spectrosc.*,

47, 289-298.

11. Hu G., Xiong W., Shi H., Li Z., Shen J. & Fang X. (2015) Raman Spectroscopic Detection Using a Two-Dimensional Spatial Heterodyne Spectrometer. *Optical Engineering*, **54**, 1-9.
12. Gornushkin I.B., Smith B.W., Panne U. & Omenetto N. (2014) Laser-Induced Breakdown Spectroscopy Combined with Spatial Heterodyne Spectroscopy. *Appl. Spectrosc.*, **68**, 1076-1084.
13. Scott A., Zheng S., Brown S. & Bell A. (2007) Spatial Heterodyne Spectrometer for FLEX. *Proc. SPIE*, **6744**, 1-11.
14. Watchorn S., Noto J. & Waldrop L.S. (2009) 8446-Angstrom Observations of Neutral Oxygen with the Spatial Heterodyne Spectrometer at Millstone Hill. *Proc. SPIE*, **7438**, 1-10.
15. Englert C.R., Harlander J.M., Emmert J.T., Babcock D.D. & Roesler F.L. (2010) Initial Ground-Based Thermospheric Wind Measurements Using Doppler Asymmetric Spatial Heterodyne Spectroscopy (DASH). *Opt. Express*, **18**, 27416-27430.
16. Stopar J.D., Lucey P.G., Sharma S.K., Misra A.K., Taylor G.J. & Hubble H.W. (2005) Raman Efficiencies of Natural Rocks and Minerals: Performance of a Remote Raman System for Planetary Exploration at a Distance of 10 Meters. *Spectrochim. Acta Part A*, **61**, 2315.
17. Mertz L. (1967) Auxiliary Computation for Fourier Spectrometry. *Infrared Physics*, **7**, 17-23.
18. Brault J.W. (1987) High Precision Fourier Transform Spectrometry: The Critical Role of Phase Correction. *Microsc. Acta*, **93**, 215-227.
19. Welch P. D. (1967) The Use of Fast Fourier Transform for the Estimation of Power Spectra: A Method Based on Time Averaging Over Short, Modified Periodograms. *IEEE Trans. Audio Electroacoust,* **15**, 70-73.
20. Bischoff W.D., Sharma S.K. & Mackenzie F.T. (1985) Carbonate Ion Disorder in Synthetic and Biogenic Magnesian Calcites: a Raman Spectral Study. *Am. Mineral.,* **70**, 581-589.
21. Urmos J.P., Sharma S.K. & Mackenzie F.T. (1991) Characterization of some Biogenic Carbonates with Raman Spectroscopy. *Am. Mineral.*, **76**, 641-646.
22. Misra A.K., Sharma S.K., Chio C.H., Lucey P.G. & Lienert B. (2005) Pulsed Remote Raman System for Daytime Measurements of Mineral Spectra. *Spectrochim. Acta*, *Part A*, **61**,

2281-2287.

23. Chio C.H., Sharma S.K. & Muenow D.W. (2004) Micro-Raman Studies of Gypsum in the Temperature Range between 9 K and 373 K. *Am. Mineral.*, **89**, 390-395.
24. Sharma S.K., Misra A.K., Clegg S.M., Barefield J.E., Wiens R.C., Acosta T.E. & Bates D.E. (2011) Remote-Raman Spectroscopic Study of Minerals Under Supercritical CO_2 Relevant to Venus Exploration. *Spectrochim. Acta Part A*, **80**, 75-81.
25. Wang A. & Zhou Y. (2014) Experimental Comparison of the Pathways and Rates of the Dehydration of Al, Fe, Mg and Ca Sulfates under Mars Relevant Conditions. *Icarus*, **234**, 162.
26. McKeown D.A. (2005) Raman Spectroscopy and Vibrational Analyses of Albite: from 25°C through the Melting Temperature. *Am. Mineral.*, **90**, 1506-1517.
27. Freeman J.J., Wang A., Kuebler K.E., Jolliff B.L. & Haskin L.A. (2008) Characterization of Natural Feldspars by Raman Spectroscopy for Future Planetary Exploration. *Can. Mineral.*, **46**, 1477-1500.
28. Lam P.K., Yu R., Lee M.W. & Sharma S.K. (1990) Structure Distortion and Vibrational Modes in Mg_2SiO_4. *Am. Mineral.,* **75**, 109-119.
29. Kuebler K.E., Jolliff B.L., Wang A. & Haskin L.A. (2006) Extracting Olivine (Fo-Fa) Compositions from Raman Spectra Peak Positions. *Geochim. Cosmochim. Acta*, **70**, 6201-6222.
30. Acosta T.E., Scott E.R.D., Sharma S.K. & Misra A.K. (2013) The Pressures and Temperatures of Meteorite Impact: Evidence from Micro-Raman Mapping of Mineral Phases in the Strongly Shocked Taliban Ordinary Chondrite. *Am. Mineral.*, **98**, 859-869.

Chapter 3: Data Reduction Optimization for Spatial Heterodyne Raman Spectroscopy with Application to Minerals, Salts and Organic Compounds

1. Harlander J.M., Roesler F.L., Reynolds R.J., Jaehnig K. & Sanders W. (1993) A Differential, Field-Widened Spatial Heterodyne Spectrometer for Investigations at High Spectral Resolution of the Diffuse Far Ultraviolet 1548 Å Emission Line from the Interstellar Medium. *Proc. SPIE*, **2006**, 139-148.
2. Harlander J.M., Roesler F.L., Cardon J.G., Englert C.R. & Conway R.R. (2002) SHIMMER: A Spatial Heterodyne Spectrometer for Remote Sensing of Earth's Middle Atmosphere. *Appl. Opt.*, **41**, 1343-1352.
3. Englert C.R., Stevens M.H., Siskind D.E., Harlander J.M. & Roesler F.L. (2010) Spatial Heterodyne Imager for Mesospheric Radicals on STPSat-1. J. Geophys. Res., **115**, D20306.
4. Mierkiewicz E.J., Reynolds R.J., Roesler F.L., Harlander J.M. & Jaehnig K.P. (2006) Detection of Diffuse Intersterllar [O II] Emission from the Milky Way Using Spatial Heterodyne Spectroscopy. *Astrophys. J.*, **650**, L63-L66.
5. Gomer N.R., Gordon C.M., Lucey P., Sharma S.K., Carter J.C. & Angel S.M. (2011) Raman Spectroscopy Using a Spatial Heterodyne Spectrometer: Proof of Concept. *Appl. Spectrosc.*, **65**, 849-857.
6. Lamsal N., Sharma S.K., Acosta T.E. & Angel S.M. (2016) Ultraviolet Stand-off Raman Measurements Using a Gated Spatial Heterodyne Raman Spectrometer. *Appl. Spectrosc.*, **70**, 666-675.
7. Lamsal N. & Angel S.M. (2015) Deep-Ultraviolet Raman Measurements Using a Spatial Heterodyne Raman Spectrometer (SHRS). *Appl. Spectrosc.*, **69**, 525-534.
8. Strange K.A., Paul K.C. & Angel S.M. (2016) Transmission Raman Measurements Using a Spatial Heterodyne Raman Spectrometer. *Appl. Spectrosc.*, **71**, 250-257.
9. Hu G., Xiong W., Shi H., Li Z., Shen J. & Fang X. (2016) Raman Spectroscopic Detection for Liquid and Solid Targets Using a Spatial Heterodyne Spectrometer. *J. Raman Spectrosc.*, **47**, 289-298.
10. Hu G., Xiong W., Shi H., Li Z., Shen J. & Fang X. (2015) Raman Spectroscopic Detection Using a Two-Dimensional Spatial Heterodyne Spectrometer. *Optical Engineering*, **54**,

1-9.

11. Gornushkin I.B., Smith B.W., Panne U. & Omenetto N. (2014) Laser-Induced Breakdown Spectroscopy Combined with Spatial Heterodyne Spectroscopy. *Appl. Spectrosc.*, **68**, 1076-1084.
12. Scott A., Zheng S., Brown S. & Bell A. (2007) Spatial Heterodyne Spectrometer for FLEX. *Proc. SPIE*, **6744**, 1-11.
13. Watchorn S., Noto J. & Waldrop L.S. (2009) 8446-Angstrom Observations of Neutral Oxygen with the Spatial Heterodyne Spectrometer at Millstone Hill. *Proc. SPIE*, **7438**, 1-10.
14. Englert C.R., Harlander J.M., Emmert J.T., Babcock D.D. & Roesler F.L. (2010) Initial Ground-Based Thermospheric Wind Measurements Using Doppler Asymmetric Spatial Heterodyne Spectroscopy (DASH). *Opt. Express*, **18**, 27416-27430.
15. Englert C.R. & Harlander J.M. (2006) Flatfielding in Spatial Heterodyne Spectroscopy. *Applied Optics*, **45**, 4583-4590.
16. Englert C.R., Harlander J.M., Cardon J.G. & Roesler F.L. (2004) Correction of Phase Distortion in Spatial Heterodyne Spectroscopy. *Applied Optics*, **43**, 6680-6687.
17. Harlander J.M., Tran H.T., Roesler F.L., Jaehnig K., Seo S.M., Sanders W. & Reynolds R.J. (1994) Field-Widened Spatial Heterodyne Spectroscopy: Correcting for Optical Defects and New Vacuum Ultraviolet Performance Tests, *Proceedings of SPIE*, **2280**, 310-319.
18. Egan M.J., Angel S.M. & Sharma S.K. (2017) Standoff Spatial Heterodyne Raman Spectrometer for Mineralogical Analysis. *Journal of Raman Spectroscopy* (in press).
19. Mertz L. (1967) Auxiliary Computation for Fourier Spectrometry. *Infrared Physics*, **7**, 17-23.
20. Brault J.W. (1987) High Precision Fourier Transform Spectrometry: The Critical Role of Phase Correction. *Microsc. Acta*, **93**, 215-227.
21. Bracewell R. (1999) The Fourier Transform and its Applications. *McGraw-Hill*, 3, 1-640.
22. Earle, S. (2015) Physical Geology, *BC Campus Open Textbook Project*, 1-632.
23. Fahad M., Iqbal Y., Riaz M., Ubic R. & Redfern S.A.T. (2016) Metamorphic Temperature Investigations of Coexisting Calcite and Dolomite Marble – Examples

from Nikani Ghar Marble and Nowshera Formation, Peshawar Basin, Pakistan. *Journal of Earth Science*, **27**, 989-997.

24. Lecuyer C., Hutzler A., Amiot R., Daux V., Grosheny D., Otero O., Martineau F., Fourel F., Balter V. & Reynard B. (2012) Carbon and Oxygen Isotope Fractionations Between Aragonite and Calcite of Shells from Modern Molluscs. *Chemical Geology*, **332-333**, 92-101.
25. Immenhauser A., Buhl D., Richter D., Niedermayr A., Riechelmann D., Dietzel M. & Schulte U. (2010) Magnesium-isotope Fractionation During Low-Mg Calcite Precipitation in a Limestone Cave – Field Study and Experiments. Geochimica et Cosmochimica *Acta*, **74**, 4346-4364.
26. Coggon R.M. & Teagle D.A.H. (2011) Hydrothermal Calcium-Carbonate Veins Reveal Past Ocean Chemistry. *Trends in Analytical Chemistry*, **30**, 1252-1268.
27. Boynton W.V. et al. (2009) Evidence for Calcium Carbonate at the Mars Phoenix Landing Site. *Science*, **325**, 61-64.
28. Morris R.V. et al. (2010) Identification of Carbonate-rich Outcrops on Mars by the Spirit Rover. *Science*, **329**, 421-424.
29. Ehlman B.L. et al. (2008) Orbital Identification of Carbonate-Bearing Rocks on Mars. *Science*, **322**, 1828-1832.
30. Wray J.J. et al. (2016) Orbital Evidence for More Widespread Carbonate-Bearing Rocks on Mars. *Journal of Geophysical Research: Planets*, **121**, 652-677.
31. Bischoff W.D., Sharma S.K. & Mackenzie F.T. (1985) Carbonate Ion Disorder in Synthetic and Biogenic Magnesian Calcites: a Raman Spectral Study. *Am. Mineral.,* **70**, 581-589.
32. Urmos J.P., Sharma S.K. & Mackenzie F.T. (1991) Characterization of some Biogenic Carbonates with Raman Spectroscopy. *Am. Mineral.*, **76**, 641-646.
33. Misra A.K., Sharma S.K., Chio C.H., Lucey P.G. & Lienert B. (2005) Pulsed Remote Raman System for Daytime Measurements of Mineral Spectra. *Spectrochim. Acta*, *Part A*, **61**, 2281-2287.
34. Sarg J.F. (2001) The Sequence Stratigraphy, Sedimentology, and Economic Importance of Evaporite – Carbonate Transitions: a Review. *Sedimentary Geology*, **140**, 9-42.

35. Schaetzl, R. (2017) http://geo.msu.edu/extra/geogmich/gypsummining.html. *Michigan State University Department of Geography, Environment, and Spatial Sciences*.
36. USG Corporation (2000) The Gypsum Construction Handbook. *John Wiley & Sons*, **7**, 1-536.
37. Hancock P.L. & Skinner B.J. (2003) The Oxford Companion to the Earth. *Oxford University Press*.
38. Phillips J. (1791) On the Effects of Gypsum or Plaster of Paris as a Manure, *Agricultural Society in Canada*, 1-18.
39. Squyres S.W. et al. (2012) Ancient Impact and Aqueous Processes at Endeavor Crater, Mars. *Science*, **336**, 570-576.
40. Gellert R. et al. (2004) Chemistry of Rocks and Soils in Gusev Crater from the Alpha Particle X-ray Spectrometer. *Science*, **305**, 829-832.
41. Kounaves S.P. et al. (2010) Soluble sulfate in the Martian soil at the Phoenix landing site. *Geophysical Research Letters*, **37**, 1-5.
42. Nachon M. et al. (2014) Calcium Sulfate Veins Characterized by ChemCam/Curiosity at Gale Crater, Mars. *Journal of Geophysical Research: Planets*, **119**, 1991-2016.
43. Bishop J.L. (2009) Mineralogy of Juventae Chasma: Sulfates in the Light-Toned Mounds, Mafic Minerals in the Bedrock, and Hydrated Silica and Hydroxylated Ferric Sulfate on the Plateau. *Journal of Geophysical Research*, **114**, 1-23.
44. Murchie S.L. (2009) A Synthesis of Martian Aqueous Mineralogy After 1 Mars Year of Observations from the Mars Reconnaissance Orbiter. *Journal of Geophysical Research*, **114**, 1-30.
45. Chio C.H., Sharma S.K. & Muenow D.W. (2004) Micro-Raman Studies of Gypsum in the Temperature Range between 9 K and 373 K. *Am. Mineral*., **89**, 390-395.
46. Sharma S.K., Misra A.K., Clegg S.M., Barefield J.E., Wiens R.C., Acosta T.E. & Bates D.E. (2011) Remote-Raman Spectroscopic Study of Minerals Under Supercritical CO_2 Relevant to Venus Exploration. *Spectrochim. Acta Part A*, **80**, 75-81.
47. Wang A. & Zhou Y. (2014) Experimental Comparison of the Pathways and Rates of the Dehydration of Al, Fe, Mg and Ca Sulfates under Mars Relevant Conditions. *Icarus*, **234**, 162.

48. Rink W.J. & Thompson J.W. (2015) Encyclopedia of Scientific Dating Methods, 848-857.
49. Dawson P., Hargreave M.M. & Wilkinson G.R. (1971) The Vibrational Spectrum of Zircon ($ZrSiO_4$). *J. Phys. C Solid St. Phys.*, **4**, 240-256.
50. Lam P.K., Yu R., Lee M.W. & Sharma S.K. (1990) Structure Distortion and Vibrational Modes in Mg_2SiO_4. *Am. Mineral.,* **75**, 109-119.
51. Kuebler K.E., Jolliff B.L., Wang A. & Haskin L.A. (2006) Extracting Olivine (Fo-Fa) Compositions from Raman Spectra Peak Positions. *Geochim. Cosmochim. Acta*, **70**, 6201-6222.
52. Acosta T.E., Scott E.R.D., Sharma S.K. & Misra A.K. (2013) The Pressures and Temperatures of Meteorite Impact: Evidence from Micro-Raman Mapping of Mineral Phases in the Strongly Shocked Taliban Ordinary Chondrite. *Am. Mineral.*, **98**, 859-869.
53. Griffith W.P. (1969) Raman Studies on Rock-forming Minerals. Part I. Orthosilicates and Cyclosilicates. *Journal of Chemical Society A: Inorganic, Physical, Theoretical*, 1372-1377.
54. Beny J.M. & Piriou B. (1987) Vibrational Spectra of Single-Crystal Topaz. *Physics and Chemistry of Minerals*, **15**, 148-154.
55. Barsan M.M., Butler I.S. & Gilson D.F.R. (2012) High-Pressure Resonance Raman Spectroscopic Study of Ultramarine Blue Pigment. *Spectrochimica Acta A Molecular and Biomolecular Spectroscopy*, **98**, 457-459.
56. Krishnamurti D. (1958) The Raman Spectrum of Quartz and its Interpretation. *Proceedings of the Indian Academy of Sciences*, **47**, 276-291.
57. McKeown D.A. (2005) Raman Spectroscopy and Vibrational Analyses of Albite: from 25°C through the Melting Temperature. *Am. Mineral.*, **90**, 1506-1517.
58. Freeman J.J., Wang A., Kuebler K.E., Jolliff B.L. & Haskin L.A. (2008) Characterization of Natural Feldspars by Raman Spectroscopy for Future Planetary Exploration. *Can. Mineral.*, **46**, 1477-1500.
59. Buzatu A. & Buzgar N. (2010) The Raman Study of Single-Chain Silicates. 107-125.
60. Pagliai M. et al. (2011) Raman and Infrared Spectra of Minerals from ab initio Molecular Dynamics Simulations: the Spodumene Crystal. *Journal of Molecular*

Structure, **993**, 151-154.

61. Leroy G., Leroy N., Penel G., Rey C., Lafforgue P. & Bres E. (2000) Polarized Micro-Raman Study of Fluorapatite Single Crystals. *Applied Spectroscopy*, **54**, 1521-1527.
62. Ming D.W. et al. (2014) Volatile and Organic Compositions of Sedimentary Rocks in Yellowknife Bay, Gale Crater, Mars. *Science*, **343**, 1-9.
63. Leshin L.A. et al. (2013) Volatile, Isotope and Organic Analysis of Martian Fines with the Mars Curiosity Rover. *Science*, **341**, 1-9.
64. Hecht M.H. et al. (2009) Detection of Perchlorates and the Soluble Chemistry of Martian Soil at the Phoenix Lander Site. *Science*, **325**, 64-67.
65. Hanley J., Chevrier V.F., Berget D.J. & Adams R.D. (2012) Chlorate Salts and Solutions on Mars. *Geophysical Research Letters*, **39**, 1-5.
66. Kounaves S., Carrier B.L., O'Neil G.D., Stroble S.T. & Claire M.W. (2014) Evidence of Martian Perchlorates, Chlorate and Nitrate in Mars Meteroite EETA 79001: Implications for Oxidants and Organics. *Icarus*, **229**, 206-213.
67. Kumari C.S. (1948) Raman Spectrum of Sodium Chlorate. *Proceedings of the Indian Academy of Sciences A*, **28**, 500-505.
68. Misra A.K., Sharma S.K., Acosta T.E., Porter J.N. & Bates D.E. (2012) Single-Pulse Standoff Raman Detection of Chemicals from 120m Distance During Daytime. *Applied Spectroscopy*, **66**, 1279-1285.
69. Misra A.K., Sharma S.K., Bates D.E. & Acosta T.E. (2010) Compact Standoff Raman System for Detection of Homemade Explosives. *Proceedings of SPIE*, **7665**, 76650U-1-76650U-11.
70. Rousseau D.L., Miller R.E. & Leroi G.E. (1968) Raman Spectrum of Crystalline Sodium Nitrate. *The Journal of Chemical Physics*, **48**, 3409-3413.
71. Khilji M.Y., Sherman W.F. & Wilkinson G.R. (1986) Variable Temperature Raman Study of Urea. *Journal of Molecular Structure*, 143, 109-112.
72. Harju M.E.E. (1993) Solid-State Transition Mechanism of Ammonium Nitrate Phases IV, III, and II Investigated by Simultaneous Raman Spectrometry and Differential Scanning Colorimetry. *Applied Spectroscopy*, **47**, 1926-1930.
73. Akiyama K., Morioka Y. & Nakagawa I. (1981) Raman Scattering and Phase Transition of Ammonium Nitrates. *Bulletin of the Chemical Society of Japan*, **54**,

1662-1666.

74. Misra A.K., Sharma S.K., Bates D.E. & Acosta T.E. (2010) Compact Standoff Raman system for Detection of Homemade Explosives. *Proceedings of SPIE*, **7665**, 76650U-1-76650U-11.
75. Shimanouchi T. (1972) Tables of Molecular Vibrational Frequencies Consolidated, *United States Defense Technical Information Center*, **1972**, 1, 1-160.
76. S.K. Sharma, Misra A.K., Lucey P.G, Angel, S.M. & McKay C.P. (2006) Remote Pulsed Raman Spectroscopy of Inorganic and Organic Materials to a Radical Distance of 100 meters. *Applied Spectroscopy*, **60**, 871-876.
77. Abasbegovic N., Vukotic N. & Colombo L. (1964) Raman Spectrum of Anthracene. *The Journal of Chemical Physics*, **41**, 2575-2577.
78. Shinohara H., Yamakita Y. & Ohno K. (1998) Raman Spectra of Polycyclic Aromatic Hydrocarbons. Comparison of Calculated Raman Intensity Distributions with Observed Spectra for Naphthalene, Anthracene, Pyrene and Perylene. *Journal of Molecular Structure*, **442**, 221-234.

Chapter 4: Future Work

1. Bialkowski S.E. (1998) Overcoming the Multiplex Disadvantage by Using Multiplex-Likelihood Inversion. *Applied Spectroscopy*, **52**, 591-598.
2. Harlander J.M. (2010) First results from an all-reflection spatial heterodyne spectrometer with broad spectral coverage. *Optics Express*, **18**, 6205-6210.
3. Hosseini S.S. (2015) Tunable Reflective Spatial Heterodyne Spectrometer: A Technique for High Resolving Power, Wide Field of View Observation of Diffuse Emission Line Sources. *ProQuest*, PhD Thesis, 1-115.
4. Harlander J.M., Reynolds R.J., Roesler F.L., Li G. (1992) Spatial Heterodyne Spectroscopy: Laboratory Tests of Field Widened, Multiple Order, and Vacuum Ultraviolet Systems. *Proceedings of SPIE*, **1743**, 48-59.
5. Lamsal N. & Angel S.M. (2015) Deep-Ultraviolet Raman Measurements Using a Spatial Heterodyne Raman Spectrometer (SHRS). *Appl. Spectrosc.*, **69**, 525-534.